Large-Scale Characterization of Quantum Emitters in High-Purity Diamond

by

Madison M. Sutula

S. B. Materials Science and Engineering & Physics
Massachusetts Institute of Technology, 2019

Submitted to the Department of Electrical Engineering and Computer Science
in Partial Fulfillment of the Requirements for the Degree of

Masters of Science in Electrical Engineering and Computer Science

at the

MASSACHUSETTS INSTITUTE OF TECHNOLOGY

February 2022

©2022 Massachusetts Institute of Technology. All rights reserved.

Signature of author: ____

Department of Electrical Engineering and Computer Science
January 20, 2022

Certified by: ____

Dirk R. Englund
Associate Professor of Electrical Engineering and Computer Science
Thesis supervisor

Accepted by: ____

Leslie A. Kolodziejski
Professor of Electrical Engineering and Computer Science
Chair, Department Committee on Graduate Students

Large-Scale Characterization of Quantum Emitters in High-Purity Diamond

by

Madison M. Sutula

Submitted to the Department of Electrical Engineering and Computer Science
on January 20, 2022 in Partial Fulfillment of the Requirements for the Degree of
Master of Science in Electrical Engineering and Computer Science

ABSTRACT

Solid state quantum memories, such as color centers in diamond, are a leading platform for the distribution of quantum information. Quantum repeaters will require many qubit registers at every quantum network node, each with long-lived spin states and high-quality single photon emissions. Here, we present techniques for large-scale characterization of color centers in diamond. We first demonstrate automated confocal microscopy and apply it to characterize silicon vacancies in diamond overgrown via chemical vapor deposition and tin vacancies in overgrown and high pressure high temperature treated diamond, yielding narrow inhomogeneous distributions of both emitters. We then demonstrate widefield photoluminescence excitation microscopy as a tool to multiplex the characterization of color center optical properties, and apply it to measure the optical properties of silicon vacancies in a sample implanted with a focused ion beam. These techniques pave the way for future large-scale characterization efforts necessary to construct quantum memory nodes.

Thesis supervisor: Dirk R. Englund

Title: Associate Professor of Electrical Engineering and Computer Science

Acknowledgements

First, I would like to thank my advisor, Professor Dirk Englund. Dirk has been a constant source of ideas and his support of this work made the efforts presented in this thesis possible. I would like to extend a special thanks to my colleagues Eric Bersin, Ian Christen, and Dr. Michael Walsh: they have served as officemates, mentors, and friends to me from the beginning. Their knowledge, willingness to offer help and advice, and ability to pinpoint a misaligned optic with fewer than three questions is inspirational. They all contributed to the work that is presented here, particularly in the design and development of software infrastructure and optical setups, and I am grateful for their friendship. I would like to thank Kevin Chen, who provided fabrication support in the cleanroom and many helpful conversations. I would also like to thank Dr. Matt Trusheim for illuminating discussions and for sharing many insights on tin vacancy centers. Alongside these wonderful core colleagues, I would like to thank the members of the Quantum Photonics group for their encouragement and for many exciting discussions over coffee. I would like to acknowledge the administrative support provided to the group by Janice Balzer and the administrative team in MIT's Research Laboratory for Electronics. Furthermore, I would like to thank David Barnett, whose financial expertise surely keeps the group running, and whose kindness and attention to detail is unparalleled.

Next, I would like to thank my collaborators. This work would not have been possible without a strong collaborative effort with MIT Lincoln Laboratory. In particular, I would like to thank Dr. P. Ben Dixon for all of the support, insight, and technical mentorship he has provided to me. I would also like to thank Dr. Scott Hamilton and Dr. Danielle Braje for their support, Dr. Justin Mallek, who made the diamond overgrowth efforts possible, and Ryan Murphy and Dr. Alex Zhang. Finally, I would like to thank our collaborators at the National Institute for Materials Science of Japan, Element 6, and Sandia National Laboratory.

The focused ion beam implantation work was performed at the Center for Integrated Nanotechnologies, an Office of Science User Facility operated for the U.S. Department of Energy (DOE) Office of Science. Sandia National Laboratories is a multimission laboratory managed and operated by National Technology Engineering Solutions of Sandia, LLC, a wholly owned subsidiary of Honeywell International, Inc., for the U.S. DOE's National Nuclear Security Administration under contract DE-NA-0003525. The views expressed in this thesis do not necessarily represent the views of the U.S. DOE or the United States Government. This work made use of the Shared Experimental Facilities supported in part by the MRSEC Program of the National Science Foundation (NSF) under award number DMR - 1419807. We thank Anthony Flores and Michael Titze for providing the focused ion beam implantation at Sandia National Laboratories.

The work presented here was supported by a NASA Space Technologies Graduate Research Opportunities Fellowship. I am indebted to the folks at NASA for their support of my work and my professional development, and I would like to thank my NASA collaborator, Dr. John Lekki, for his support, availability, and excitement about all things quantum. I would also like to extend thanks to the Center for Integrated Quantum Materials for providing both funding support and access to a strong community of quantum materials scientists.

Most of all, I would like to thank my family, and especially my sibling, Ozark, and my parents, Kathy and Jon. Their never-ending love, patience, and encouragement has shaped who I am today, and who I would like to become.

Contents

1 Introduction **12**

1.1 Solid state quantum memories 13

1.2 Color centers in diamond 14

1.2.1 Physical properties of diamond 14

1.2.2 Nitrogen-vacancy centers 15

1.2.3 Group IV-vacancy centers 16

1.3 Thesis outline 17

2 Theory **18**

2.1 Hamiltonian 19

2.2 Interaction terms 19

2.2.1 Spin-orbit coupling 19

2.2.2 Jahn-Teller interaction 19

2.2.3 Strain 20

2.2.4 Zeeman interaction 23

2.2.5 Summary 24

2.3 Atomic interactions with electromagnetic fields 25

2.3.1 Dipole transitions 25

2.3.2 Two-level atom 26

2.3.3 Optical Bloch equations 28

2.3.4 Optical linewidths 29

2.3.5 Broadening 30

3 Optical setups **33**

3.1 Confocal microscopy 33

3.1.1 Principles 33

3.1.2 Experimental cryogenic confocal microscope setup 34

3.2 Widefield microscopy 37

3.2.1 Principles 37

3.2.2 Experimental widefield microscope setup 38

3.3 Automated microscopy 39

4 Characterization of SiVs in CVD diamond **45**

4.1 Chemical vapor deposition of diamond 45

4.1.1 Principles 45

4.1.2 Sample 46

4.2 Experimental results 47

4.2.1 Sample preparation 47

4.2.2 Photoluminescence measurements 48

4.2.3 Photoluminescence excitation measurements 52

5 Characterization of SnVs in HPHT-treated diamond **59**

5.1 High pressure high temperature treatment 59

5.1.1 Principles 59

5.1.2 Samples 60

5.2 Experimental results 61

5.2.1 Sample preparation 61

5.2.2 Photoluminescence measurements 61

5.2.3 Photoluminescence excitation measurements 68

6 Widefield microscopy for efficient optical characterization **70**

6.1 Focused-ion beam implantation 70

6.1.1 Principles 70

6.1.2 Sample 70

6.2 Experimental results 72
6.2.1 Sample preparation 72
6.2.2 Photoluminescence measurements 72
6.2.3 Widefield photoluminescence excitation measurements 75

7 Conclusion **85**
7.1 Outlook 85
7.2 Future directions 87

List of Figures

1.1 Nitrogen vacancy center in diamond 15

1.2 Silicon vacancy center in diamond 16

2.1 Crystallographic orientation of the silicon vacancy center 23

2.2 Energy spectrum of a single silicon vacancy center 25

2.3 Monte Carlo simulation of inhomogeneous broadening 32

3.1 Working principle of our confocal microscope 34

3.2 Cryogenic confocal microscope schematic 36

3.3 Working principle of our widefield microscope 37

3.4 Cryogenic widefield microscope schematic 38

3.5 Automated microscope control scheme 40

3.6 Typical confocal scan image 41

3.7 Region of interest on spectrometer charge coupled device 41

3.8 Typical photoluminescence spectrum 42

3.9 Pulse sequence and collection window for photoluminescence excitation experiments 43

3.10 Typical photoluminescence excitation measurement 44

4.1 Optical micrograph of overgrown diamond film 46

4.2 Confocal image of diamond overgrowth layer 48

4.3 Image filtering and candidate emitter site selection 49

4.4 Example photoluminescence spectrum of silicon vacancy in overgrown sample 50

4.5 Candidate silicon vacancy sites and resulting photoluminescence inhomogeneous distribution 51
4.6 Inhomogeneous distribution of silicon vacancy photoluminescence in three regions of overgrown sample 52
4.7 Summary of silicon vacancy photoluminescence inhomogeneous distribution in overgrown sample 53
4.8 Experimental stack and peak fitting for a silicon vacancy in the overgrown sample 54
4.9 Comparison of photoluminescence excitation taken in two regions of the overgrown sample over two cooldowns 55
4.10 Summary of silicon vacancy photoluminescence excitation in the overgrown sample 56
4.11 Inhomogeneous distribution of silicon vacancy B and C transitions in the overgrown sample 57
4.12 Spatial map of silicon vacancy linewidths in the overgrown sample 57
4.13 Spatial map of silicon vacancy optical properties in the overgrown sample . . 58

5.1 Example photoluminescence spectra of tin vacancy centers in high pressure high temperature-treated diamond samples 62
5.2 Candidate tin vacancy sites and resulting photoluminescence inhomogeneous distribution for Sample A 63
5.3 Candidate tin vacancy sites and resulting photoluminescence inhomogeneous distribution for Sample B 64
5.4 Inhomogeneous distribution of tin vacancy photoluminescence for two high pressure high temperature-treated samples 65
5.5 Silicon vacancy and 720 nm photoluminescence peaks observed in high pressure high temperature-treated Sample A. 65
5.6 Candidate sites and resulting photoluminescence for silicon vacancy centers in Sample A 66

5.7 Silicon vacancy photoluminescence peaks observed in high pressure high temperature-treated Sample B . . . 67
5.8 Candidate sites and resulting photoluminescence for silicon vacancy centers in Sample B . . . 67
5.9 Summary of tin vacancy photoluminescence excitation in high pressure high temperature-treated Sample A . . . 68
5.10 Summary of tin vacancy photoluminescence excitation in high pressure high temperature-treated Sample B . . . 69

6.1 Room temperature widefield microscopy of focused ion beam-implanted sample 71
6.2 Candidate silicon vacancy sites and resulting photoluminescence inhomogeneous distribution in focused ion beam-implanted sample . . . 73
6.3 Candidate tin vacancy sites and resulting photoluminescence inhomogeneous distribution in focused ion beam-implanted sample . . . 73
6.4 Summary of silicon vacancy and tin vacancy photoluminescence inhomogeneous distribution in focused ion beam-implanted sample . . . 74
6.5 Widefield field of view under incoherent illumination. . . . 75
6.6 Raw widefield image under resonant excitation . . . 76
6.7 Cropped and filtered widefield image under resonant excitation . . . 77
6.8 Example aggregate widefield image and candidate sites. . . . 78
6.9 Image processing for one widefield photoluminescence excitation site . . . 81
6.10 Summary of widefield photoluminescence excitation results over one laser scan range . . . 82
6.11 Summary of widefield photoluminescence excitation results for 47,314 silicon vacancy peaks . . . 83
6.12 Clustered reconstruction of focused ion beam sites measured with widefield microscopy . . . 84

7.1 Summary: silicon vacancy photoluminescence excitation measurements . . . 86
7.2 Summary: tin vacancy photoluminescence measurements . . . 87

Chapter 1

Introduction

Quantum mechanics enables a wealth of theoretical and experimental possibilities that cannot be realized in a classical information framework, including quantum key distribution [1], provably secure [2] communication, long baseline interferometry [3], and distributed quantum computing. Of particular interest is the realization of a quantum internet comprised of quantum networks that enable the distribution of entanglement over long distances and between many users [4, 5]. Unfortunately, demonstrations of entanglement over long links have been hampered by exponential loss in optical fibers [6]. In classical communications over fiber networks, loss can be overcome by periodically passing through a repeater that amplifies and re-transmits the encoded information. However, quantum information cannot be amplified or copied without destroying the quantum state of interest, as described by the no-cloning theorem [7]. Fortunately, quantum information can be stored and distributed with the help of quantum memories that take the place of classical photonic amplifiers. Ultimately, the construction of a scalable quantum network requires quantum repeater nodes with many long-lived, optically accessible quantum memories.

Diamond color centers are well-suited quantum memories for use in quantum networks. They feature spin-selective transitions between optical ground and excited state manifolds, enabling the generation of spin-photon entanglement. In the framework of photon-emission based protocols, remote spin-spin entanglement can be generated via entangling operations between spin-entangled photons from two memories [8]. In this thesis, we develop processes

that yield high quality Group-IV emitters in diamond. We report the distribution of optical linewidths and emission frequency of these emitters –two critical metrics for quantum information applications –with robust, high-throughput characterization tools.

1.1 Solid state quantum memories

Atom-like systems in solids have been widely investigated for use in quantum information applications since the turn of the millennium. These solid state quantum memories can be classified by their charge, spin, and optical properties, and quantum applications generally require access to and control over all of these degrees of freedom. Notably, quantum memories in solids have been used to demonstrate applications in quantum sensing, quantum computing, and quantum communication [9]. However, scaling solid state systems remains a critical challenge, as large numbers of co-located physical qubits will be required to encode fault-tolerant logical qubits for computing applications [10] and practical quantum repeaters.

Quantum memories for computing and networking applications require long-lived spin lifetimes and optical access. Solid state defects typically offer an electron or nuclear spin that serves as the quantum memory, while the host crystal is typically a wide-semiconductor transparent to infrared or even visible light. Spin-photon entanglement can be generated via a number of emission, absorption, or reflection-based schemes, depending on the details of the spin-photon interface and the protocol of interest [8, 11, 12]. Unlike trapped ion or neutral atom memories that rely on purely atomic optical transitions, the energetic transitions of solid state quantum memories couple to the environment and are less frequency-stable. Additionally, vibrational modes in the lattice couple to defects, reducing the spectral quality of emitted photons. Some photons are emitted a narrow band at the energy of the optical transition called the zero photon line (ZPL), while some lose energy to the lattice as phonons and are emitted into a broad phonon sideband (PSB) with lower energy [13].

The fraction of light that is emitted into the ZPL versus the PSB is characterized by the Debye-Waller factor. The spontaneous emission rate into the frequency band of interest can

be engineered via quantum electrodynamics (QED), wherein defects are coupled to nanofabricated waveguides or cavities [14]. Such devices can be heterogeneously integrated with photonic integrated circuits [15], coupled to tapered fibers [16] or solid-immersion lenses [17], or vertically coupled into an objective [18] to efficiently extract the spin-coupled photons. All of these strategies rely on emitters with high-quality optical transitions. For the remainder of this thesis, we will turn our attention to defects in diamond, and focus on scalable characterization of optical properties.

1.2 Color centers in diamond

1.2.1 Physical properties of diamond

Diamond is a natural host for optically active defect centers. It is a wide-bandgap semiconductor with an indirect bandgap of 5.5 eV, so it is transparent to visible light [19]. Diamond crystals consist of sp^3 hybridized carbon atoms: the unit cell is described by a two-atom basis with carbon atoms at (0,0,0) and $(\frac{a}{4},\frac{a}{4},\frac{a}{4})$ arranged in a face-centered cubic (FCC) lattice, yielding the typical inter-penetrating diamond cubic lattice. The lattice constant a of diamond is $a = 3.567\AA$. Mineral diamond is naturally occurring: the high pressures and temperatures deep in the Earth's mantle create an environment in which diamond is the most stable phase of carbon. However, the presence of other elements during this uncontrolled natural synthesis typically yields crystals with large impurity concentrations.

A number of advances have been made in recent years to grow high quality single crystal synthetic diamonds, typically by high pressure high temperature (HPHT) synthesis or chemical vapor deposition (CVD). As a result, single crystal synthetic diamonds with ultralow impurity concentrations are commercially available. Electronic grade diamonds with low nitrogen concentrations are particularly attractive for quantum optics applications [20].

1.2.2 Nitrogen-vacancy centers

The negatively charged nitrogen vacancy center (NV) in diamond is a leading solid state quantum memory [21]. It consists of a single substitutional nitrogen atom neighboring a vacancy in the diamond lattice (Fig. 1.1). The NV possesses a spin-1 triplet ground state that is optically addressable, enabling optical readout of the spin state. A narrow optical transition ZPL near 637 nm is accompanied by a broad PSB at lower energies.

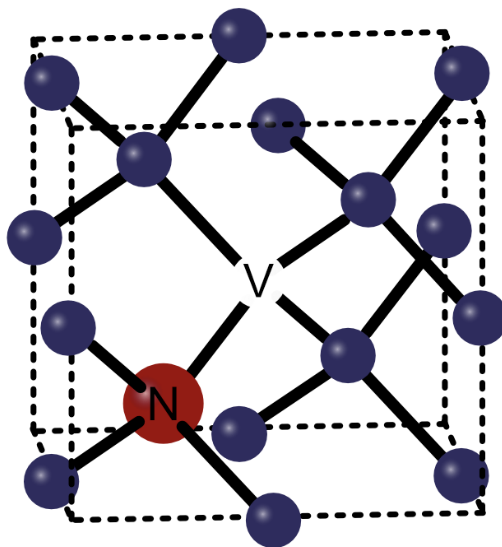

Figure 1.1: Nitrogen vacancy center in diamond. The negatively-charged nitrogen vacancy center (NV) is formed by a single substitutional nitrogen atom adjacent to a vacancy in the diamond lattice.

Because the NV has a permanent electric dipole, it is sensitive to electric fields. Local charge noise in the diamond and from nearby surfaces can cause inhomogeneous broadening of the NV transition linewidths by several orders of magnitude. This process is dominated by spectral diffusion, so the resultant photons cannot be reliably used to produce high-fidelity entanglement. In particular, it is difficult to integrate NV centers into nanophotonic waveguides and cavities without destroying the spectral properties [22, 23]. Additionally, only 3% of light is emitted into the narrow ZPL, so the majority of NV fluorescence is not useful for quantum information applications [24]. In spite of these challenges, NVs have been used in a number of quantum information demonstrations, primarily via integration into solid immersion lenses that direct the NV emission out of the crystal [4, 25].

1.2.3 Group IV-vacancy centers

In recent years, the negatively-charged Group IV-vacancy centers in diamond have emerged as a promising alternative to the NV. Group IV-vacancy centers consist of a single interstitial Group IV atom (Si, Ge, Sn, or Pb) surrounded by two lattice vacancies (Fig. 1.2). The centers are oriented along the ⟨111⟩ family of directions, so like the NV, there are four distinct orientations from the perspective of the surface of single-crystal diamond. Group IV vacancies also possess a narrow ZPL with distinct optical transitions that enable spin initialization and readout, and a PSB in which some of the transition energy is dissipated into vibrational modes in the diamond lattice.

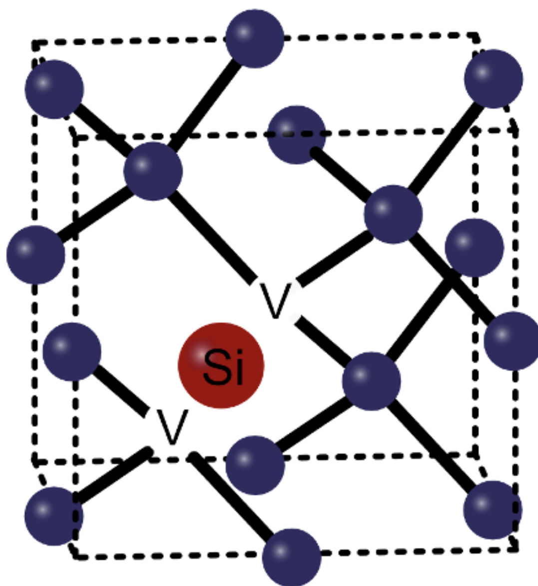

Figure 1.2: Silicon vacancy center in diamond. The negatively-charged silicon vacancy (SiV) in diamond is formed by a single interstitial silicon and a symmetric pair of vacancies. Other Group IV-vacancy centers involve a Ge, Sn, or Pb atom in place of the Si.

Notably, Group IV-vacancy centers are first-order insensitive to electric field noise due to their inversion symmetry. These properties are explored further in Chapter 2. Throughout this thesis, the negatively-charged Group IV-vacancy centers will be referred to as the Group IV-vacancy centers (or SiVs, GeVs, SnVs, and PbVs), and any references to the neutral

centers SiV^0, GeV^0, SnV^0, PbV^0 will be noted as such.

1.3 Thesis outline

Chapter 2 details the relevant theory describing the electronic structure of Group IV color centers in diamond. We provide details on the Hamiltonian and observed optical transitions, and present a simple model for inhomogeneous broadening processes.

Chapter 3 describes the optical microscopes used to perform experiments. We discuss the working principles and specific implementations of confocal and widefield microscopes, and the process by which experiments are automated to enable large-scale optical characterization.

Chapter 4 details the experimental observation of silicon vacancy centers in high-purity diamond deposited by chemical vapor deposition. We observe a narrow inhomogeneous distribution of silicon vacancies across the sample.

Chapter 5 compares the tin vacancies observed in two samples that have been overgrown by chemical vapor deposition and then high pressure high temperature treated. We observe spectrometer-limited photoluminescence spectra, and find a narrow inhomogeneous distribution of tin vacancy centers in both samples.

Chapter 6 describes a technique to measure photoluminescence excitation using widefield microscopy. We walk through the experimental process and develop a noise model to describe frequency-correlated background modulation, and present the optical properties that result from our analysis.

Finally, in Chapter 7, we conclude by examining future prospects for the automated techniques and sample innovations described in the previous Chapters. We discuss the implications of this work and potential for further work in these directions.

Chapter 2

Theory

Group IV-vacancy color centers in diamond possess D_{3d} symmetry with their axis along the $\langle 111 \rangle$ family of directions in the diamond lattice [26]. The symmetry group contains a wealth of information about the properties of group IV emitters. They contain a C_3 rotational symmetry about their axis and three C_2 rotational axes that lie in the perpendicular plane. They contain three mirror planes perpendicular to their axis, and an inversion center located at the interstitial Group IV atom. Altogether, the irreducible representations that make up D_{3d} symmetry include A_{1g}, A_{2u}, E_{xg}, E_{yg}, E_{xu}, and E_{yu}. The total electronic makeup of the Group IV-vacancy complex contains 11 electrons [27]: 6 contributed from C– dangling bonds, 4 from the interstitial Group IV valance electrons, and one electron donated from the lattice that yields the overall negative charge and ground state paramagnetism. In the simplest picture, the SiV consists of a two-level system with an optically-split ground and excited state. Spin-orbit coupling and the dynamic Jahn-Teller interaction split both the ground and excited states, and the presence of lattice strain distorts the electronic orbitals. The application of an external magnetic field yields a Zeeman interaction. In this Chapter, we explore these contributions in detail, discussing the critical role symmetry plays in the electronic structure of Group IV-vacancy centers and the resulting observables.

2.1 Hamiltonian

The 11-electron SiV can be treated as a single-hole system [28, 29]: applying molecular orbital theory, the ground state configuration of the SiV will be $a_{1g}^2 a_{2u}^2 e_g^4 e_u^3$ and the excited state configuration $a_{1g}^2 a_{2u}^2 e_g^3 e_u^4$. In this picture, the hole is promoted to the e_g state upon excitation [28]. A reasonable choice of basis is therefore given by:

$$\text{Ground state: } {}^2E_g \quad \{|e_{g,x}\rangle\}, \{|e_{g,y}\rangle\} \tag{2.1}$$

$$\text{Excited state: } {}^2E_u \quad \{|e_{e,x}\rangle\}, \{|e_{e,y}\rangle\} \tag{2.2}$$

2.2 Interaction terms

2.2.1 Spin-orbit coupling

The single unpaired electron in the Group IV-vacancy system yields a defect with spin $S = \frac{1}{2}$. The electron spin interacts with the neighboring orbitals via the spin-orbit interaction, which is described by the Hamiltonian

$$\hat{H}_{SO} = \lambda_{g,e} \hat{L} \cdot \hat{S} \tag{2.3}$$

where $\lambda_{g,e}$ is the coupling constant for the ground (excited) state, $\hat{S}$ is the electron spin operator $\hat{S} = S_x\hat{x} + S_y\hat{y} + S_z\hat{z}$, and $\hat{L}$ is the orbital operator $\hat{L} = L_x\hat{x} + L_y\hat{y} + L_z\hat{z}$. The spin-orbit interaction breaks the degeneracy of the ground and excited state basis vectors given in Eqs. 2.1-2.2. The spin-orbit interaction in the Group IV-vacancy centers is purely orbital and does not mix spin terms, enabling the observation of spin-tagged fluorescence [30].

2.2.2 Jahn-Teller interaction

The Jahn-Teller interaction couples orbital states via vibrational modes supported by the diamond lattice. The Jahn-Teller Hamiltonian for the gorund (excited) state can be written

in the basis defined by Eqs. 2.1-2.2:

$$\hat{H}_{JT} = \begin{pmatrix} \Upsilon_{x,(g,e)} & \Upsilon_{y,(g,e)} \\ \Upsilon_{y,(g,e)} & -\Upsilon_{x,(g,e)} \end{pmatrix} \tag{2.4}$$

The eigenvalues of Eq. 2.4 give the level splitting of the ground (g) and excited (e) state caused by the Jahn-Teller interaction. The mechanisms are distinct, but the Jahn-Teller and spin-orbit interactions can be grouped together as perturbations that lift the orbital degeneracy, yielding four optical transitions that can be collectively described by a ground state splitting, an excited state splitting, and the optical transition between the ground and excited states. Experimental reports of the ground and excited state splittings of Group IV-vacancy centers in diamond are summarized in Table 2.1.

Emitter	Δg	Δe	**Ref.**
SiV	46 GHz	255 GHz	[31]
GeV	152 GHz	981 GHz	[32]
SnV	850 GHz	3 THz	[33]
PbV	2 THz	70.6 THz*	[34]

Table 2.1: Group IV-vacancy center ground (Δg) and excited (Δe) state splittings. All values are experimentally measured except for *, which was predicted with density functional theory. The magnitude of the splitting increases with the mass of the Group IV element of the color center.

2.2.3 Strain

When force is applied to a material, the deformation response of the material is described by the stress-strain relationship. Stress is the applied force per unit area, and the stress tensor can be represented by

$$\sigma = \begin{pmatrix} \sigma_{11} & \sigma_{12} & \sigma_{13} \\ \sigma_{21} & \sigma_{22} & \sigma_{23} \\ \sigma_{31} & \sigma_{32} & \sigma_{33} \end{pmatrix} \tag{2.5}$$

Each σ_{ij} is the component of stress along a plane normal to the ith primitive lattice vector with stress is applied in the direction parallel to the jth primitive lattice vector. In cubic lattices, diamond included, the diagonal elements represent principal stress along the cubic

directions, and the off-diagonal elements represent shear stress. Strain is the elongation per unit length along each coordinate:

$$\epsilon = \begin{pmatrix} \epsilon_{11} & \epsilon_{12} & \epsilon_{13} \\ \epsilon_{21} & \epsilon_{22} & \epsilon_{23} \\ \epsilon_{31} & \epsilon_{32} & \epsilon_{33} \end{pmatrix} \tag{2.6}$$

The diagonal elements represent principal strain along the primitive lattice vectors, in which the elongation occurs in the same direction as the applied stress. The off-diagonal terms represent shear strain, in which the deformation response is non-zero in the plane perpendicular to the applied stress. In the linear-elastic regime, typically valid for small displacements in crystals such as diamond, the stress-strain relationship is governed by a modified Hooke's law:

$$\sigma_{ij} = \sum_{k=1}^{3}\sum_{l=1}^{3} c_{ijkl}\epsilon_{ij} \tag{2.7}$$

The stiffness tensor c_{ijkl} is a rank-4 tensor which relates stress to strain element-wise. However, given the cubic crystal structure of diamond and associated symmetry, only three independent elastic modulii are necessary to fully describe the elastic response to applied stress when the principle axes are aligned with the $\langle 100 \rangle$ family of crystallographic directions:

$$\begin{pmatrix} \sigma_{11} \\ \sigma_{22} \\ \sigma_{33} \\ \sigma_{12} \\ \sigma_{13} \\ \sigma_{23} \end{pmatrix} = \begin{pmatrix} c_{11} & c_{12} & c_{12} & 0 & 0 & 0 \\ c_{12} & c_{11} & c_{12} & 0 & 0 & 0 \\ c_{12} & c_{12} & c_{11} & 0 & 0 & 0 \\ 0 & 0 & 0 & c_{44} & 0 & 0 \\ 0 & 0 & 0 & 0 & c_{44} & 0 \\ 0 & 0 & 0 & 0 & 0 & c_{44} \end{pmatrix} \begin{pmatrix} \epsilon_{11} \\ \epsilon_{22} \\ \epsilon_{33} \\ 2\epsilon_{12} \\ 2\epsilon_{13} \\ 2\epsilon_{23} \end{pmatrix} \tag{2.8}$$

In the context of the local crystallographic environment around a Group IV-vacancy center in diamond, lattice strain leads to deformation of the electronic orbitals that make up the defect, correspondingly modulating the energy spectrum. There are a number of sources of anisotropic lattice strain in diamonds, including the presence of point and line defects. Strain can be seeded during the growth process, but even low-strain substrates that are im-

planted with ions to generate defect centers can have high strain regions. The implantation process damages the lattice, knocking some carbon atoms out of place and generating localized regions of high strain and lattice anisotropy. There are also a few ways in which some lattice strain can be alleviated, as will be discussed further in subsequent Chapters. All of these mechanisms yield permanent (or at least temporally stable) deformation in the lattice, so it follows that they result in plastic deformation rather than a linear-elastic response. It is therefore appropriate to describe the relationship of the static response of the Group IV-vacancy energy spectrum relative to the strain environment rather than the applied stress.

It is convenient to move into a coordinate system defined by the axes of high symmetry for the Group IV-vacancy centers to describe the effect of strain, as shown in Fig. 2.1. The axial direction $\hat{z}$ is defined to be parallel to the Group IV-vacancy axis, which lies along one of the four equivalent crystallographic directions [111], $[1\bar{1}1]$, $[11\bar{1}]$, and $[\bar{1}11]$. Transverse strain is applied in the plane perpendicular to the axial direction; without loss of generality, a reasonable choice to construct an orthogonal basis is to define $\hat{x}$ along the $[\bar{1}\bar{1}2]$ and $\hat{y}$ along $[1\bar{1}0]$ (for $\hat{z}\|[111]$).

The strain Hamiltonian can be written in terms of the D_{3d} irreducible representations [35]:

$$\hat{H}_{strain} = \epsilon_{A_{1g},(g,e)} A_{1g,(g,e)} + \epsilon_{E_{x,g},(g,e)} E_{x,g,(g,e)} + \epsilon_{E_{y,g}(g,e)} E_{y,(g,e)} \tag{2.9}$$

In the basis defined by Eq. 2.1 (2.2) , the strain Hamiltonian for the ground (excited) state is

$$\hat{H}_{strain} = \begin{pmatrix} \epsilon_{A_{1g},(g,e)} - \epsilon_{E_{g,x},(g,e)} & \epsilon_{E_{g,y},(g,e)} \\ \epsilon_{E_{g,y},(g,e)} & \epsilon_{A_{1g},(g,e)} + \epsilon_{E_{g,x},(g,e)} \end{pmatrix} \tag{2.10}$$

where the matrix elements can be written in terms of strain applied in the coordinate reference frame of the Group IV-defect and using empirically determined strain susceptibilities for the ground (excited) state, following the convention of Meesala et al. [31]:

$$\epsilon_{A_{1g}} = t_{\perp,(g,e)}(\epsilon_{xx} + \epsilon_{yy}) + t_{\|,(g,e)}\epsilon_{zz} \tag{2.11}$$

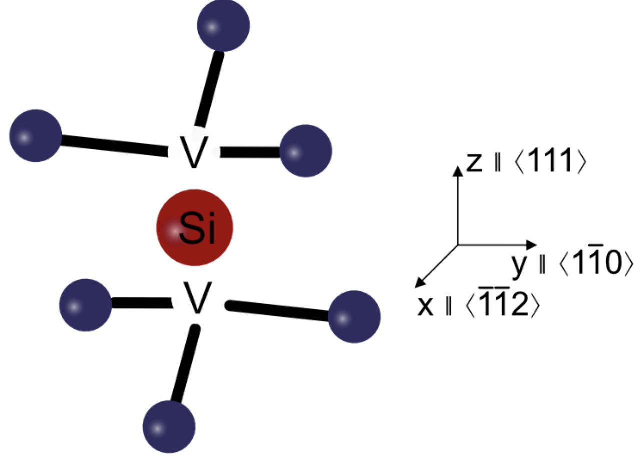

Figure 2.1: Crystallographic orientation of the silicon vacancy center. The SiV center is oriented along the ⟨111⟩ family of axes in the diamond lattice, so there are four equivalent crystallographic orientations the defect could lie upon. Axial strain is defined to be applied along the z axis, parallel to one of the ⟨111⟩ directions, while transverse strain is applied in the $x - y$ plane, perpendicular to the z axis. An orthogonal basis can be constructed in terms of crystallographic directions by letting $\hat{x}$ lie along the $\langle\bar{1}\bar{1}2\rangle$ family of directions and $\hat{y}$ lie along the $\langle 1\bar{1}0\rangle$ family of directions. For other Group IV-vacancy centers, the Si atom is replaced with a Ge, Sn, or Pb atom.

$$\epsilon_{E_{g,x}} = d_{(g,e)}(\epsilon_{xx} - \epsilon_{yy}) + f_{(g,e)}\epsilon_{xz} \tag{2.12}$$

$$\epsilon_{E_{g,y}} = -2d_{(g,e)}\epsilon_{xy} + f_{(g,e)}\epsilon_{yz} \tag{2.13}$$

Here, $t_{\perp,(g,e)}$, $t_{\parallel,(g,e)}$, $d_{(g,e)}$, and $f_{(g,e)}$ are the empirically determined prefactors. From Eq. 2.10, it is clear that $\epsilon_{A_{1g},(g,e)}$ strain leads to an overall shift in the energy levels in the ground (excited) states, while $\epsilon_{E_g,(g,e)}$ strain leads to modification of the splittings Δe and Δg.

2.2.4 Zeeman interaction

Both the orbital angular momentum and spin magnetic moment of the Group IV-vacancy center couple to external magnetic fields via the Zeeman interaction:

$$\hat{H}_{Zeeman} = g_L \frac{\mu_B}{\hbar}\left(\hat{L} \cdot \overrightarrow{B} + g_s \hat{S} \cdot \overrightarrow{B}\right) \tag{2.14}$$

Where the Lande g-factor for orbital angular momentum $g_L = 1$ and for spin $g_s \approx 2$, $\overrightarrow{B} = B_x\hat{x} + B_y\hat{y} + B_z\hat{z}$ is the vector applied magnetic field, $\hat{L} = \hat{L}_x\hat{x} + \hat{L}_y\hat{y} + \hat{L}_z\hat{z}$ is the

orbital angular momentum operator, and $\hat{S} = \frac{\hbar}{2}(\hat{\sigma}_x \hat{x} + \hat{\sigma}_y \hat{y} + \hat{\sigma}_z \hat{z})$ is the spin operator. Under application of sufficient magnetic field to fully split out the Zeeman sublevels, the basis defined in Eq. 2.1-2.2 can be modified as follows:

$$\text{Ground state:} \qquad \{|E_{g,x} \uparrow\rangle\}, \{|E_{g,x} \downarrow\rangle\}, \{|E_{g,y} \uparrow\rangle\}, \{|E_{g,y} \downarrow\rangle\} \tag{2.15}$$

$$\text{Excited state:} \qquad \{|E_{u,x} \uparrow\rangle\}, \{|E_{u,x} \downarrow\rangle\}, \{|E_{u,y} \uparrow\rangle\}, \{|E_{u,y} \downarrow\rangle\} \tag{2.16}$$

2.2.5 Summary

The perturbative interactions described in sections 2.2.1-2.2.4 are summarized in Fig. 2.2, and the total Hamiltonian for the Group IV-vacancy center can be written as

$$\hat{H} = \hat{H}_{\circ} + \hat{H}_{SO} + \hat{H}_{JT} + \hat{H}_{strain} + \hat{H}_{Zeeman} \tag{2.17}$$

The combined effects of spin-orbit coupling, the Jahn-Teller interaction, and crystal strain yield four optical transitions A, B, C, and D, where A is the highest energy transition between the upper excited state and the lower ground state, and D is the lowest energy transition between the lower excited state and upper ground state (Fig. 2.2). The application of a magnetic field lifts the double degeneracy of each of these optical transitions via the Zeeman interaction: the qubit state can then be encoded in the spin states of the ground state manifold and read out optically.

In low-strain diamond, spin-orbit coupling is the dominant contribution to the energy splitting [35, 36], so the eigenbasis of $\hat{H}_{SO}$ is a good basis to describe the Group IV-vacancy emission spectrum. In highly strained environments such as nanodiamonds and bulk diamond that has been densely implanted via bulk implantation or focused ion beam (FIB), the eigenbasis of $\hat{H}_{strain}$ is more suitable.

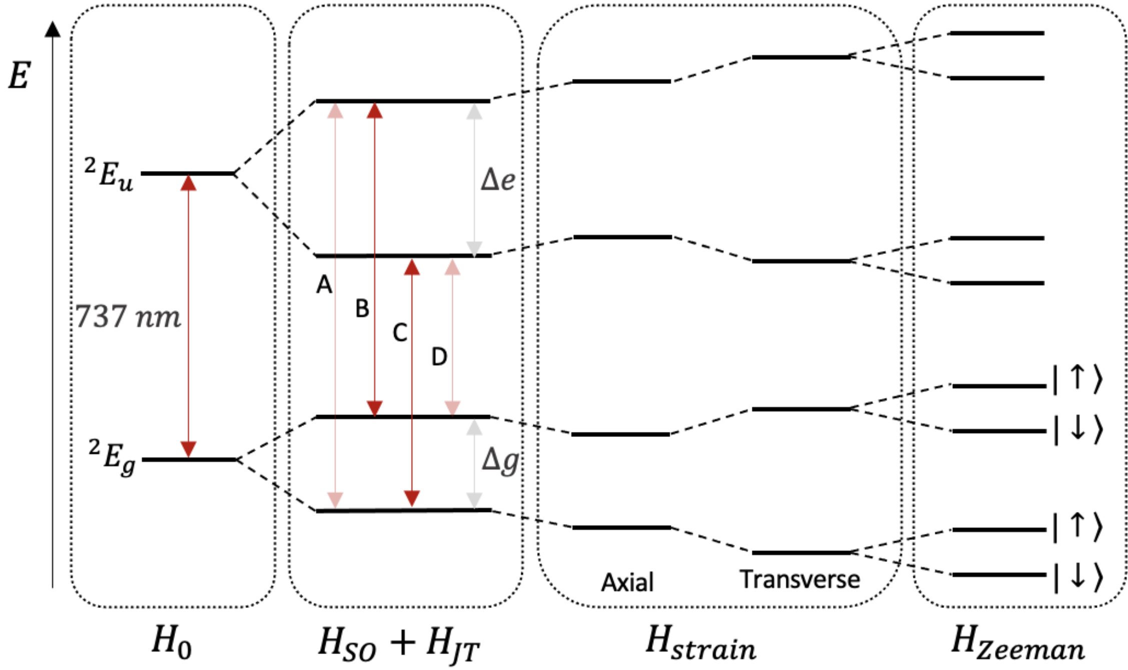

Figure 2.2: Energy spectrum of a single silicon vacancy center. The fourfold degenerate ^2E_g and ^2E_u energy manifolds are split into four doubly-degenerate optical transitions by the combined effect of spin-orbit and Jahn-Teller interactions. Axial strain in the lattice around the SiV shifts absolute energy difference between ^2E_g and ^2E_u levels, while strain transverse to the SiV axis impacts the ground and excited state splittings Δg and Δe. Finally, the application of a magnetic field yields a Zeeman interaction, splitting out individual spin states. The other Group IV-vacancy centers exhibit an energy spectrum of the same form.

2.3 Atomic interactions with electromagnetic fields

2.3.1 Dipole transitions

The interaction of an atom with dipole $\hat{d} = e\hat{r}$ and an electric field $\overrightarrow{E}$ can be described by the dipole Hamiltonian

$$\hat{H}_{dipole} = -\hat{d} \cdot \overrightarrow{E} = -\sum_i \sum_j |\psi_i\rangle \langle\psi_j| \langle\psi_i| \hat{d} |\psi_j\rangle \cdot \overrightarrow{E} \tag{2.18}$$

where $|\psi_i\rangle$ are atomic basis functions. Transitions between arbitrary atomic states are subject to constraints, and allowed transitions must obey

$$\langle\psi_j| \hat{r} |\psi_i\rangle \neq 0 \tag{2.19}$$

The dipole Hamiltonian can be written in the basis of Group IV-vacancy basis functions (Eqs. 2.1-2.2), which are general to defect centers with D_{3d} symmetry:

$$\begin{pmatrix} \langle e_{g,x}| \hat{d}_x |e_{u,x}\rangle & \langle e_{g,x}| \hat{d}_x |e_{u,y}\rangle \\ \langle e_{g,y}| \hat{d}_x |e_{u,x}\rangle & \langle e_{g,y}| \hat{d}_x |e_{u,y}\rangle \end{pmatrix} = \begin{pmatrix} e & 0 \\ 0 & -e \end{pmatrix} \tag{2.20}$$

$$\begin{pmatrix} \langle e_{g,x}| \hat{d}_y |e_{u,x}\rangle & \langle e_{g,x}| \hat{d}_y |e_{u,y}\rangle \\ \langle e_{g,y}| \hat{d}_y |e_{u,x}\rangle & \langle e_{g,y}| \hat{d}_y |e_{u,y}\rangle \end{pmatrix} = \begin{pmatrix} 0 & -e \\ -e & 0 \end{pmatrix} \tag{2.21}$$

$$\begin{pmatrix} \langle e_{g,x}| \hat{d}_z |e_{u,x}\rangle & \langle e_{g,x}| \hat{d}_z |e_{u,y}\rangle \\ \langle e_{g,y}| \hat{d}_z |e_{u,x}\rangle & \langle e_{g,y}| \hat{d}_z |e_{u,y}\rangle \end{pmatrix} = \begin{pmatrix} e & 0 \\ 0 & e \end{pmatrix} \tag{2.22}$$

There are four distinct dipolar orientations of the Group IV-vacancy center, oriented along the internal coordinates of the Group IV-vacancy center (Fig. 2.1). Of the four optical transitions exhibited by the Group IV-vacancy center with no applied magnetic field (Fig. 2.2), the B and C transitions involve the Z dipole alone and are therefore linearly polarized, while the A and D transitions involve an equal mixture of the X and Y dipole and are circularly polarized [29, 35].

The transition probabilities between atomic orbitals can be calculated explicitly with Fermi's golden rule:

$$P = 2\pi\rho |\langle \psi_f| \hat{d} |\psi_i\rangle|^2 \tag{2.23}$$

where ρ is the density of states, ψ_i is the initial atomic state, and ψ_f is the final atomic state.

2.3.2 Two-level atom

Consider the simplest interaction between an atom and an electromagnetic field: a two-level atom with states $|1\rangle$ and $|2\rangle$ under excitation by a weak, nearly-resonant classical light field. A monochromatic light field can be written as

$$E(r,t) = \varepsilon(r,t)e^{-i(\nu t - \mathbf{k}\cdot\mathbf{r})} + \varepsilon^*(r,t)e^{i(\nu t - \mathbf{k}\cdot\mathbf{r})} \tag{2.24}$$

The dipole operator can be expanded in the basis states of the two-level atom:

$$\hat{d} = -(|1\rangle\langle 2|\,\mu_{12} + |2\rangle\langle 1|\,\mu_{21}) \tag{2.25}$$

The total system Hamiltonian is therefore

$$\hat{H} = \hbar\omega\,|2\rangle\langle 2| - (|1\rangle\langle 2|\,\mu_{12} + |2\rangle\langle 1|\,\mu_{21}) \cdot \left(\varepsilon e^{-i\nu t} + \varepsilon^* e^{i\nu t}\right) \tag{2.26}$$

The time-dependent state can be expressed in terms of the atomic eigenstates:

$$|\psi(t)\rangle = c_1(t)\,|1\rangle + c_2(t)\,|2\rangle \tag{2.27}$$

The time evolution of the state is governed by the time-dependent Schrodinger equation

$$i\hbar\frac{d}{dt}\,|\psi(t)\rangle = \hat{H}\,|\psi(t)\rangle \tag{2.28}$$

The equations of motion are therefore

$$\dot{c}_1 = ic_2\frac{\mu}{\hbar} \cdot \left(\varepsilon e^{-i\nu t} + \varepsilon^* e^{i\nu t}\right) \tag{2.29}$$

$$\dot{c}_2 = -i\omega c_2 + ic_1\frac{\mu^*}{\hbar} \cdot \left(\varepsilon e^{-i\nu t} + \varepsilon^* e^{i\nu t}\right) \tag{2.30}$$

To simplify these expressions, first move into a frame rotating with the frequency of the optical excitation by defining

$$c_2 = \tilde{c}_2 e^{-i\nu t} \tag{2.31}$$

The equations of motion in the rotating frame (relabeling $\tilde{c}_2 \rightarrow c_2$) are

$$\dot{c}_1 = ic_2\frac{\mu}{\hbar}\left(\varepsilon e^{-2i\nu t} + \varepsilon^*\right) \tag{2.32}$$

$$\dot{c}_2 = i(\nu - \omega)c_2 + ic_1\frac{\mu}{\hbar}\left(\epsilon + \epsilon^* e^{2i\nu t}\right)$$

Finally, in the rotating wave approximation, valid for weak, nearly resonant fields that oscillate much faster than the relevant dynamics, fast-oscillating terms $\propto e^{\pm 2i\nu t}$ can be ignored. Further, let the detuning $\delta \equiv \nu - \omega$ and the Rabi frequency $\Omega \equiv \frac{\mu\varepsilon}{\hbar}$, so the equations of motion are

$$\dot{c}_1 = i\Omega^* c_2 \tag{2.33}$$

$$\dot{c}_2 = i\delta c_2 + i\Omega c_1 \tag{2.34}$$

These equations of motion can be solved analytically by direct substitution, and are particularly simple on resonance with $\delta = 0$:

$$\ddot{c}_1 = -|\Omega|^2 c_1 \tag{2.35}$$

$$\ddot{c}_2 = -|\Omega|^2 c_2$$

Choosing initial conditions such that the atom is in the ground state at $t = 0$, the time-dependent evolution of the two level atom is given by

$$c_1(t) = \cos|\Omega|t \tag{2.36}$$

$$c_2(t) = i\frac{\Omega}{|\Omega|}\sin|\Omega|t \tag{2.37}$$

The time-dependent probability to find the atom in $|1\rangle$ or $|2\rangle$ is simply the square of the probability amplitude:

$$P_{|1\rangle} = |c_1(t)|^2 = \cos^2|\Omega|t \tag{2.38}$$

$$P_{|2\rangle} = |c_2(t)|^2 = \sin^2|\Omega|t \tag{2.39}$$

2.3.3 Optical Bloch equations

The simple two-level picture is sufficient to describe the evolution of population between atomic states, but it does not capture some processes observed in real atoms, including spontaneous emission and decoherence. These phenomena are succinctly described in the density matrix formalism. The optical Bloch equations (OBE) describe the dynamics of a

two-level atom under illumination that has a spontaneous emission rate γ:

$$\dot{\rho}_{11} = \gamma\rho_{22} + i(-\Omega^*\rho_{21} + \Omega\rho_{12}) \tag{2.40}$$

$$\dot{\rho}_{22} = -\gamma\rho_{11} + i(\Omega^*\rho_{21} - \Omega\rho_{12}) \tag{2.41}$$

$$\dot{\rho}_{12} = -(\gamma_{12} - i\delta)\rho_{12} - i\Omega^*(\rho_{22} - \rho_{11}) \tag{2.42}$$

$$\dot{\rho}_{21} = -(\gamma_{21} + i\delta)\rho_{21} + i\Omega(\rho_{22} - \rho_{11}) \tag{2.43}$$

In this system, $\gamma_{12} = \gamma_{21} = \frac{\gamma}{2}$. A phenomenological term can be added to the decay rate of coherence to account for dephasing from other sources, such as the finite linewidth of the excitation laser:

$$\gamma_{12} \rightarrow \tilde{\gamma}_{12} = \frac{\gamma}{2} + \gamma_d \tag{2.44}$$

These equations cannot generally be solved analytically, but under certain circumstances, approximate solutions offer useful insight. For example, for continuous wave excitation in the long time limit ($t^{-1} \ll \Omega, \gamma$), the OBEs can be solved in steady state:

$$\rho_{21} = \frac{i\Omega(\rho_{22} - \rho_{11})}{\gamma_{21} + i\delta} \tag{2.45}$$

The steady-state population in the excited state is therefore

$$\rho_{22} = \frac{2|\Omega|^2}{\frac{\gamma}{\gamma_{21}}(\gamma_{21}^2 + \delta^2) + 4|\Omega|^2} \tag{2.46}$$

2.3.4 Optical linewidths

The amount of time that an emitter spends in the excited state before undergoing spontaneous emission is referred to as the excited state lifetime. Spontaneous emission is described by an exponential decay process in time:

$$P(t) = P(t = 0)e^{-|t|/T_1} \tag{2.47}$$

where the excited state lifetime is the inverse of the spontaneous emission rate, $T_1 = 1/\gamma$. The finite luminescence lifetime constrains the lineshape of the emitted photons. The narrowest possible frequency bandwidth of an emitted photon is given by the Fourier transform:

$$I(\omega) = \sqrt{\frac{2}{\pi}} \frac{\gamma}{\gamma^2 + (\omega - \omega_0)^2} \tag{2.48}$$

A summary of the lifetime and transform-limited linewidth of quantum emitters in diamond is given in Table 2.2

Emitter	Excited state lifetime	Transform-limited linewidth	Reference
NV	12.24 ns	13 MHz	[28]
SiV	1.96 ns	94 MHz	[37]
GeV	6 ± 0.1 ns	26 ± 1 MHz	[32]
SnV	4.5 ± 2 ns	35 ± 5 MHz	[36]
PbV	3 ns	53 MHz	[34]

Table 2.2: Excited state lifetime and corresponding transform-limited linewidth for NVs and Group IV-vacancy centers in diamond.

2.3.5 Broadening

Solid state emitters are susceptible to homogeneous and inhomogeneous processes that yield measured linewidths broader than the lifetime limit. Homogeneous thermal broadening is related to phonon dephasing and has a Lorentzian profile [18]. Inhomogeneous broadening processes result in Gaussian lineshapes, and are often attributed to electric or magnetic field noise in the local environment near the color center.

The NV center is particularly susceptible to charge (electric field) noise due to its large permanent dipole moment. Field fluctuations in the local environment around an NV can cause GHz-scale spectral diffusion, many times larger than the lifetime limited linewidth over slow timescales [38]. As a result, each initialization of the NV center has a non-zero probability to produce a photon in a completely different frequency band than the previous measurement, an effect detrimental to the indistinguishably necessary for quantum information applications. Further, NVs are so sensitive to charge noise from surfaces that it is

impractical to integrate them into typical nanostructures such as waveguides and cavities.

To first order, inversion-symmetric Group IV-vacancy centers are protected from DC noise. However, line broadening is observed in Group IV-vacancy centers, even in the bulk. The primary mechanism presumed to account for this observed phenomenon is strain [18, 35, 39], though it is observed even in samples which are presumed to be ultra-low strain based on the absolute emission energies and small inhomogeneous distribution. In spite of promising experimental demonstrations of lifetime-limited SiVs [16], GeVs [32], and SnVs [40] in nanostructures, spectral diffusion appears to play a role in Group IV-vacancy centers in bulk [39, 41] and in nanostructures [16, 32].

Because all measurements in this thesis were conducted below 4 K, the primary contribution to broadening processes is inhomogeneous, yielding Gaussian broadening on top of the Lorentzian emission profile. The inhomogeneous broadening process can be approximated via Monte Carlo simulation in which an emitter experiences n broadening events with magnitude m, where the values of n and m are each selected from a normal distribution. The product nm yields the amount of inhomogeneous broadening δw, which is a parameter that modifies the Gaussian linewidth in a modified pseudo-Voigt function:

$$f_v = a\Bigg(\frac{f}{1+4(\frac{x-b}{w})^2} + (1-f) * \exp\big(-4\log(2)\big(\frac{x-b}{w+\delta w}\big)^2\big)\Bigg) \tag{2.49}$$

The pseudo-Voigt function is parameterized by linewidth w, offset b, Lorentzian-Gaussian character f, and a scaling factor a chosen to unit-normalize the area under the profile.

Consider an example in which the distribution of the discrete number of broadening events n is distributed around 25 events with a standard deviation of 10, the magnitude of broadening events is continuously distributed around 10 MHz with a standard deviation of 5 MHz, and the Lorentzian-Gaussian character is 0.5. Let any negative broadening events that result from the model be mapped to 0 broadening. This model is applied to the SiV, which has a lifetime-limited linewidth of 94 MHz [16]. A histogram of the distribution of linewidths that

results after 1000 iterations, simulating 1000 photoluminescence excitation measurements, is shown in Fig. 2.3.

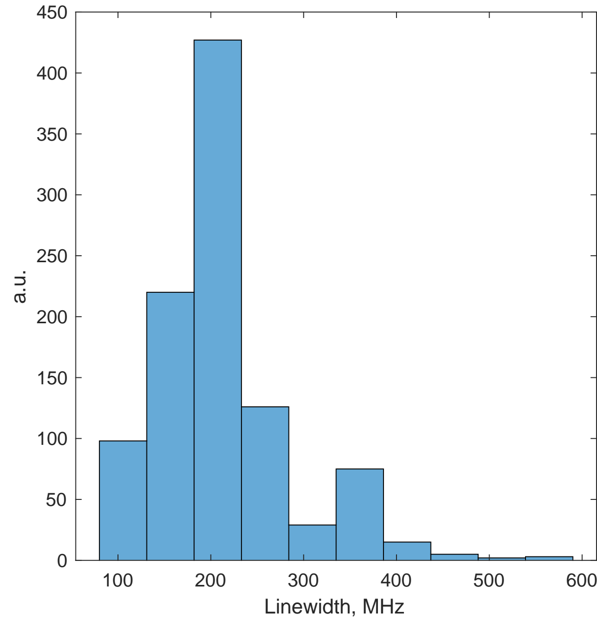

Figure 2.3: Monte Carlo simulation of inhomogeneous broadening. SiVs with a lifetime-limited linewidth of 94 MHz are considered. Each emitter encounters n discrete instances of broadening events of m magnitude. In this example, n is chosen from a discrete distribution around 25 events with a standard deviation of 10, and the magnitude of each event m is distributed around 10 MHz with a standard deviation of 5 MHz and the constraint that all negative broadening events map to 0.

Chapter 3

Optical setups

Now that we have explored the physics behind color centers in diamonds, we turn our attention to measuring the optical properties of single emitters. The home-built cryogenic microscope setups described in the following section serve to measure color center linewidths and the inhomogeneous distribution of emitters in a sample. As previously described, these metrics are critical to characterize and understand to build scalable quantum networks based on color centers.

3.1 Confocal microscopy

3.1.1 Principles

Confocal microscopes are commonly employed in fluorescence microscopy because they enable the illumination of and collection from a small image volume. The image plane at the sample is confocal with a pinhole on the collection path, which acts as a spatial filter to remove any light originating outside the focal plane. The lateral resolution of a confocal microscope is a function of the point spread function (PSF), and can be expressed in terms of the numerical aperture (NA) of the objective [42]:

$$r_{lat} = 0.37\frac{\lambda}{\mathrm{NA}} \tag{3.1}$$

In order to image larger areas on a sample than the diffraction-limited spot size, galvanometers (galvos) can be used to change the angle of the collimated light entering the 4f system. In this approach, angular shifts in the Fourier plane are mapped to lateral shifts in the image plane on the sample. Dual-axis scanning galvos enable the construction of a 2D sample image. Fig. 3.1 shows a schematic of the operating principle of our scanning confocal microscope.

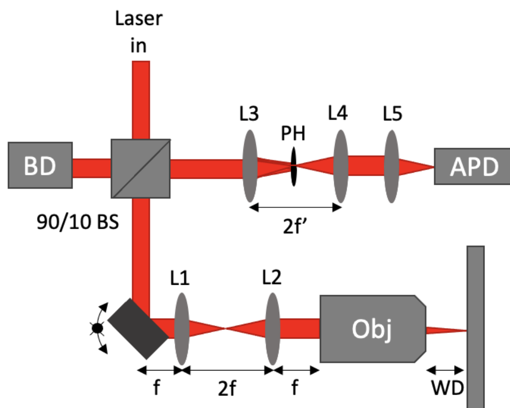

Figure 3.1: Working principle of our confocal microscope. A confocal microscope involves the illumination of a small volume on the sample with focused light. In our setup, collimated input laser light enters the microscope via the 10% port on a 90/10 beamsplitter (90/10 BS), while the reflected power is discarded into a beam dump (BD). The incoming light is then incident on dual-axis scanning galvos in the Fourier plane located at the back focal plane of L1. A 4f system comprising L1 and L2 maps the input laser to the back focal plane of the objective, which focuses the light on a sample located at the working distance (WD) of the objective. Light that has interacted with the sample reflects through the 90/10 BS and passes through an additional 2f system with a pinhole (PH) at the image plane. The pinhole acts as a spatial filter: only light that originates from the focus of the objective passes through. Finally, L5 focuses the confocal image spot onto an avalanche photodiode (APD). Filters can be added to collect only fluorescence.

3.1.2 Experimental cryogenic confocal microscope setup

A cryogenic scanning confocal microscope was used to collect fluorescence from individual Group-IV emitters. A detailed schematic of the setup is presented in Fig. 3.2. A Hubner Cobolt 06-MLD laser at 515 nm was used for off-resonant excitation for fluorescence imaging and charge state repump. The Cobolt had built-in power modulation with 70 dB extinction, which was controlled via TTL pulses from a SpinCore Pulseblaster ESR Pro, with 2 ns resolution.

Resonant excitation near 737 nm for SiVs was performed with an M^2 Lasers SolsTiS titanium:sapphire (Ti:Sapph) laser, which was pumped with a 16W M^2 Lasers Equinox pump laser at 532 nm. Resonant excitation near 620 nm for SnVs was performed with an M^2 Lasers External Mixing Module (EMM). The EMM contained a periodically-poled lithium niobate (PPLN) crystal in which near-infrared (NIR) Ti:Sapph light from another M^2 Lasers SolsTiS module light underwent sum frequency generation with a 1950 nm seed laser, yielding visible light. This SolsTiS module was pumped with a Lighthouse Photonics 15 W Sprout-G laser at 532 nm. Both resonant excitation lasers were stabilized via a HighFinesse WS7-60 wavemeter with an 8-channel switch. Each laser could be locked to the wavemeter with 10 MHz relative precision via a PID control loop that fed back to the laser diode, and the frequency was read out in real time via software.

The excitation lasers mixed via two configurations involving the input polarizing beam splitter (PBS). The fiber-coupled Cobolt entered via one port: any fiber fluorescence noise was removed with a 750 nm shortpass filter (for SolsTiS configuration) or a 640 nm shortpass filter (for EMM configuration). The SolsTiS combined with the Cobolt in a wavelength division multiplexer (Thorlabs RGB46HF, via the blue port). The EMM was free-space coupled and entered via the other PBS port. Fine power control of each laser was achieved with a half wave plate (HWP) immediately before the PBS. The SolsTiS power was controlled independently at its input fiber port.

After the excitation lasers are combined and linearly polarized on the PBS, they passed through a half waveplate that controlled the polarization axis. Then, a beamsplitter sent 10% of the excitation light into the confocal microscope: scanning galvonometer mirrors (Nutfield QS-7 Galvonometer Scanner) preceded a 4f imaging setup and a NA=0.95 achromatic objective (Montana Instruments Cryo-Optic). The sample was mounted inside the cryostat on a stage stack comprising three Attocube ANP101 piezoelectric nanopositioners (piezo stages) that enabled motion in x, y, and z and a cold finger maintained at ~ 4 K. A radiation shield separated the sample space from the room-temperature objective.

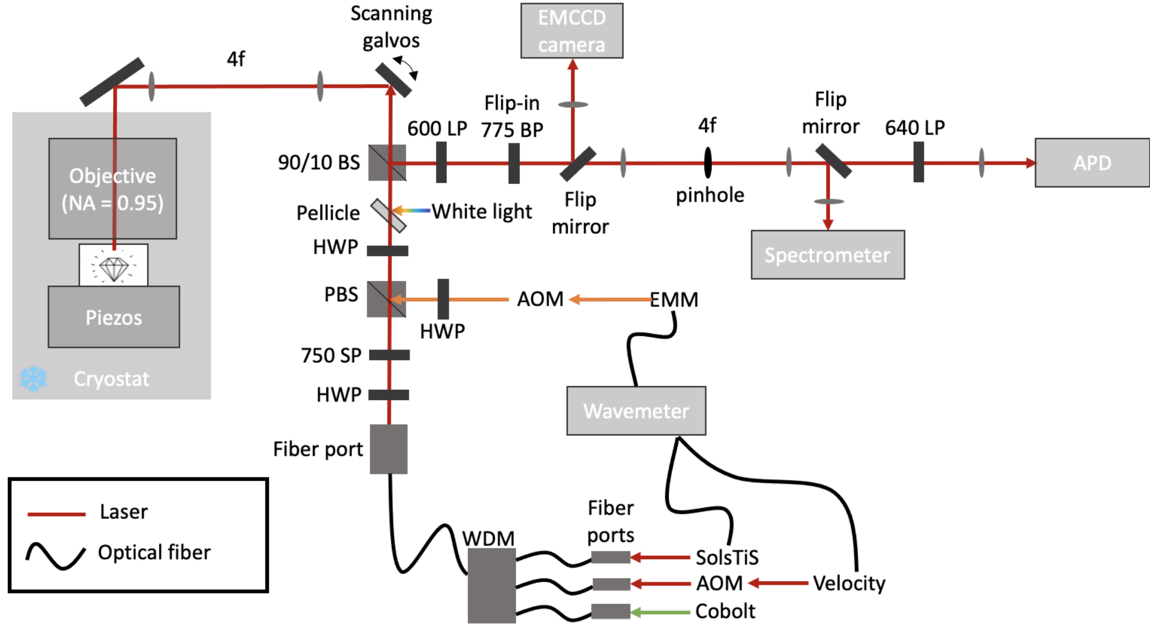

Figure 3.2: Cryogenic confocal microscope schematic. Details are provided in main text. WDM = wavelength division multiplexer, HWP = half waveplate, SP = shortpass filter, LP = longpass filter, PBS = polarizing beamsplitter, BS = beamsplitter, NA = numerical aperture, APD = avalanche photodiode, AOM = acousto-optic modulator

Fluorescence from the sample, along with reflected laser light, was collected by the objective and passed back through the 4f system. At the beamsplitter, 90% of the light was reflected into the collection path, where a 600 nm longpass filter blocked the strong green laser. For SiV measurements involving a resonant laser at 737 nm, a bandpass filter was used to collect only the phonon side band (775/46-25 Semrock Brightline RazerEdge). The light then passed through a spatial filter comprising a 2f system with a pinhole at the image plane. An automated flip mirror directed the light to be focused into a spectrometer (Princeton Instruments Isoplane SCT 320) or onto a free space avalanche photodiode (APD) (Excelitas SPCM-AQRH-14). A 640 nm longpass filter (Semrock BLP01-635R) was used to block 620 nm or 637 nm resonant laser, enabling collection of the SnV or NV phonon side band. The piezo stages were used to bring the sample into focus after cooldown and to image regions of the sample beyond the view of the scanning galvos. An incoherent white light source and a Photometrics Cascade 1K electron-multiplied charge coupled device (EMCCD) were used to aide in focusing and moving the sample and for widefield measurements.

3.2 Widefield microscopy

3.2.1 Principles

Unlike a confocal microscope, a conventional widefield microscope relies on the simultaneous illumination of a broad region on a sample, with the entirety of the image plane mapped onto a camera. There are two relevant operational modes: either the reflected light can be collected directly, or it can be filtered and fluorescence can be collected. The illumination volume of a widefield microscope is much larger than that of a confocal microscope, and there is no pinhole to act as a spatial filter. The lateral resolution of an optical microscope is given by Rayleigh's criterion

$$r_{lat} = 0.61\frac{\lambda}{N.A.} \tag{3.2}$$

A schematic of the operating principle of our widefield microscope is shown in Fig. 3.3.

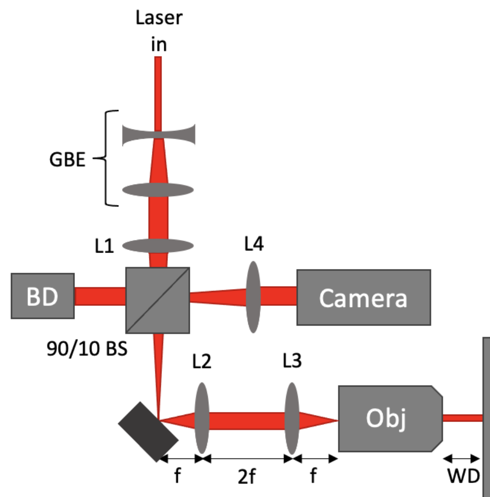

Figure 3.3: Working principle of our widefield microscope. In contrast to a confocal microscope, a widefield microscope involves illumination of a large sample area with collimated light. In our setup, collimated input laser light is first expanded with a Galilean beam expander (GBE), and then it enters the microscope via the 10% port on a 90/10 beamsplitter (90/10 BS), while the reflected power is discarded into a beam dump (BD). L1 focuses the collimated beam onto the 4F system, which maps it to the back aperture of the objective. Together, the GBE + L1 make up the telescope. For our configuration to be easily converted from confocal to widefield mode, we utilize the confocal 4f (L2, L3) to map the galvos (which act as two simple mirrors) to the back aperture of the objective. The sample is located at the working distance (WD) of the objective. Light that has interacted with the sample reflects through the 90/10 BS and is focused onto a camera sensor with L4. Filters can be added to collect only fluorescence.

3.2.2 Experimental widefield microscope setup

The cryogenic confocal microscope described previously was additionally outfitted with flip-in components to allow conversion between widefield and confocal imaging modes. The widefield configuration is shown in detail in Fig. 3.4. In this configuration, which requires much higher resonant laser power, the SolsTiS was fiber coupled directly into the setup to avoid damaging the WDM and avoid additional loss through the WDM. A 2x magnification telescope on a magnetic mount flipped into the excitation path to increase the illuminated area on the sample. The rest of the microscope functioned in broadly the same configuration as described previously, with the galvos fixed to a neutral position. The addition of the telescope enabled widefield imaging of the entire field of view that could previously be achieved by scanning the galvos in the confocal configuration. In widefield mode, scanning was accomplished by moving the sample using the piezos.

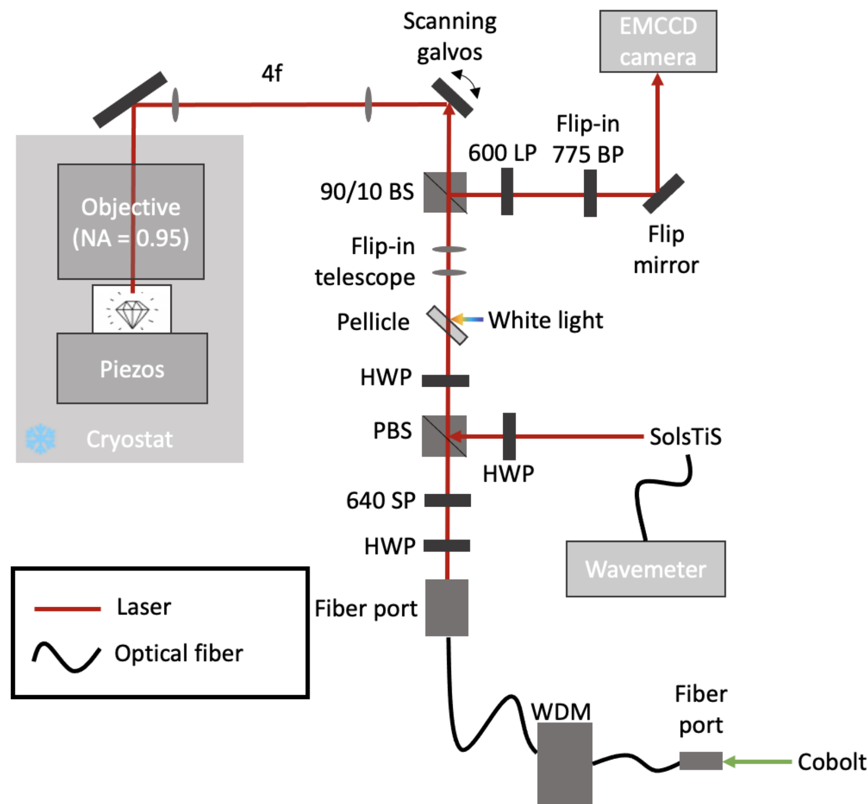

Figure 3.4: Cryogenic widefield microscope schematic. Details are provided in main text. For telescope and other imaging details, see Fig. 3.3. HWP = half waveplate, SP = shortpass filter, LP = longpass filter, PBS = polarizing beamsplitter, BS = beamsplitter, NA = numerical aperture, APD = avalanche photodiode, EMCCD = electron multiplied charge coupled device

On the collection path, the widefield image was focused onto the EMCCD camera, which had an active area of 1002 x 1004 pixels. The resolution was sufficient to image single emitters with high resolution, as each pixel corresponds to approximately 80 nm of sample distance.

3.3 Automated microscopy

Automated microscopy enabled efficient large-scale characterization of diamond color centers. The experiments described here were controlled by a central control computer which interfaced with auxiliary electronic control equipment, including a National Instruments Data Acquisition module (NIDAQ) and a Spincore PulseBlaster via a hardware server. The hardware server was used to send serial or TCP commands to the SolsTiS, EMM, and Velocity lasers. A schematic of the control scheme is presented in Fig. 3.5 and a detailed description of the experimental software front end (CommandCenter) and hardware server back end (hwserver) is presented in [43].

Sample characterization was performed at ~ 4 K in a Montana Instruments Cryostation using the home-built confocal microscope described previously. Emitter candidates were observed in confocal scans under 515 nm excitation as diffraction-limited bright spots, as shown in Fig. 3.6. Peak finding was employed to identify these candidates amongst the noisy background.

This list of candidate emitter sites served as the starting point for automated experiments. Each site was stored as a set of (x,y) galvo coordinates that could be readily revisited by setting a NIDAQ voltage output fed into the galvo controllers. Photoluminescence (PL) measurements were performed at each candidate site using 515 nm green excitation. The green light was filtered out with a 600 nm longpass filter and the fluorescence that remained was focused on the spectrometer (see Fig. 3.2). A small region of interest (ROI) was selected on the spectrometer camera to capture the entirety of the signal from the sample without extra noise from the unused CCD pixels (Fig. 3.7).

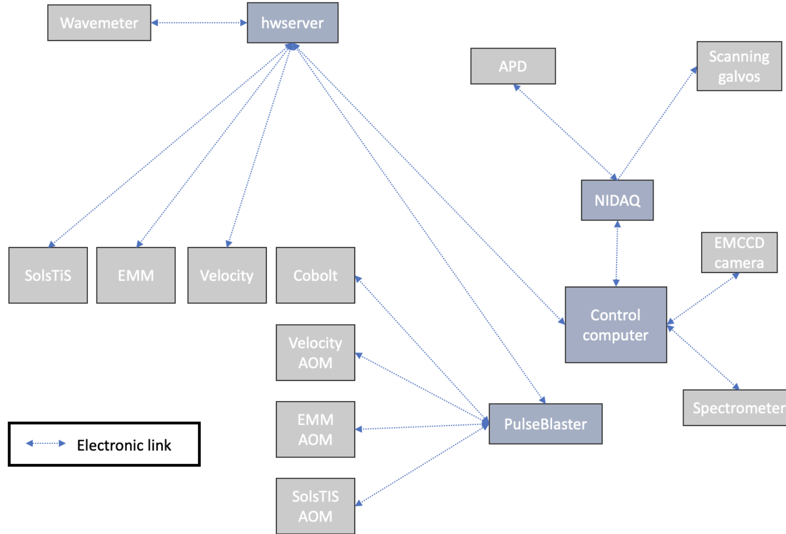

Figure 3.5: Automated microscope control scheme. A central control computer with CommandCenter software [43] was used to communicate with auxiliary devices. Data was fed from the spectrometer to the control computer via serial communication. The NIDAQ was controlled via serial communication using the NIDAQ DLL. NIDAQ analog output lines were used to control the galvos, while NIDAQ analog input lines read in counts from the APD using a digital gate. The control computer was also used to load pulse sequences onto the PulseBlaster, which sent TTL pulses to trigger the Cobolt, Velocity AOM driver, and EMM AOM driver. Finally, the control computer interfaced via serial communication with the hardware server (hwserver). The hwserver initiated serial communication with the wavemeter and TCP communication with the SolsTiS and EMM lasers, enabling active feedback on the frequency setpoint and software triggering of pulse sequences when the laser was locked to the wavemeter at the frequency of interest.

The spectrometer has a background offset that is present even when integrating for 0 s, and the intensity of the last pixel is always artificially high-valued as a charge artifact in the CCD, as shown in the left panel of Fig. 3.8. For this reason, the last pixel is removed from consideration, and the average background value with 0 s integration time of 669 is subtracted for all subsequent photoluminescence spectra in this thesis. A typical spectrum of an NV center (with corrections) is shown in the right panel of Fig. 3.8.

Next, peaks were fit to each of the PL spectra collected, and sites with a peak were selected for photoluminescence excitation (PLE). PLE involves probing the photoluminescence response of a color center as it is driven with a resonant laser that is scanned across the transition: these measurements elucidate several important aspects of the emitter and its environment.

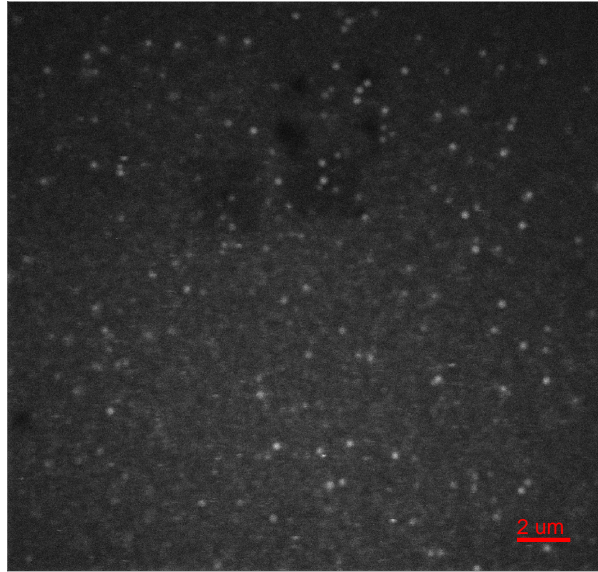

Figure 3.6: Typical confocal scan image. Single nitrogen vacancy centers are visible as diffraction-limited bright spots against the dark background of the diamond substrate. The 515 nm Cobolt was used for excitation, and fluorescence above 640 nm was collected on the APD.

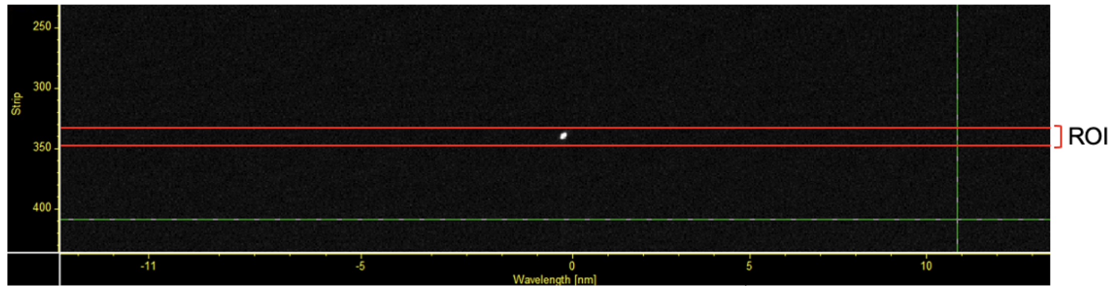

Figure 3.7: Region of interest on spectrometer charge coupled device. The bright spot in the center is the image of a laser reflected off the surface of the diamond substrate and focused into the spectrometer, through the grating, and onto a charge coupled device (CCD) camera. The ROI is selected to encompass the focused spot but neglect the remaining CCD camera area, which add unwanted readout noise.

PLE served as a measure of the frequency-domain behavior of the emitter, including the linewidth and center frequency of emission. The spectrometer-limited bandwidth of the PL measurements is determined by the spectrometer resolution ($\Delta\lambda = 0.05$ nm) and wavelength

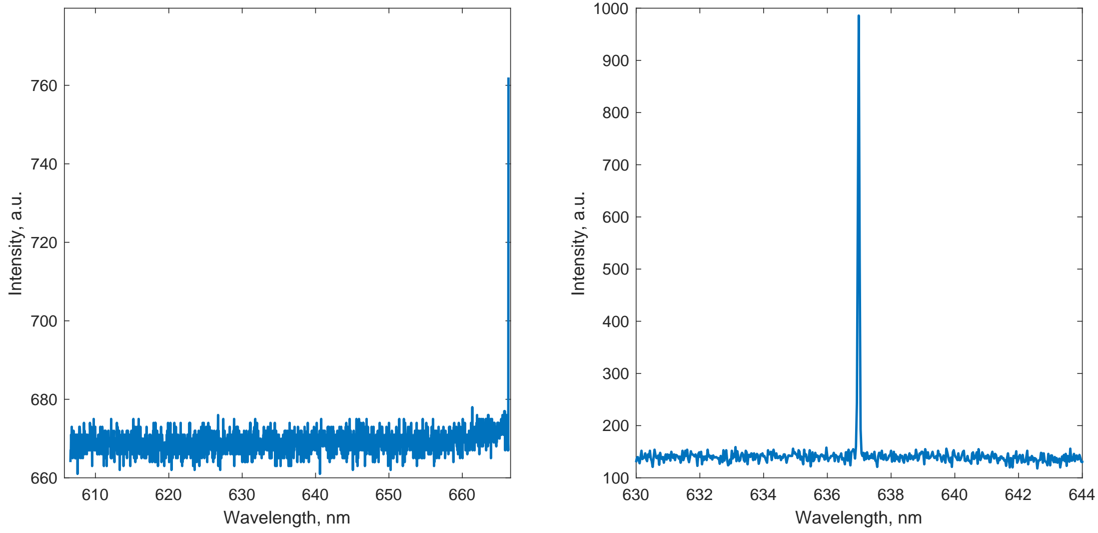

Figure 3.8: Typical photoluminescence spectrum. The left panel shows the 0 s integration time spectrometer background, and the intensity spike at 666 nm corresponds to the last pixel of the CCD camera, and is an artifact of charge build-up. These spectrometer artifacts are removed from subsequent photoluminescence spectra. The mean value of the background (after removing the last pixel) is 669. In the right panel, a single spectrometer-limited peak is observed for a nitrogen vacancy center under 515 nm excitation. The 0 s integration time spectrometer background was subtracted, and the last CCD pixel was removed.

of interest:

$$\Delta f = c\frac{\Delta\lambda}{\lambda^2} \tag{3.3}$$

Conveniently, the resonant laser could be tuned to the center frequency of a spectrometer-limited PL peak and then scanned around the center frequency to find the much narrower PLE peak with high probability (Table 3.1).

Emitter	Resonant excitation wavelength	Spectrometer limited bandwidth	Resonant laser	Tuning range
SnV	620 nm	39 GHz	M^2 EMM	25 GHz
NV	637 nm	37 GHz	Velocity	80 GHz
SiV	737 nm	28 GHz	M^2 SolsTiS	25 GHz

Table 3.1: Resonant excitation wavelength, spectrometer-limited bandwidth, resonant laser used, and mode-hop free tuning range available for the emitters of interest. For each color center, the tuning range covers enough of the spectrometer-limited bandwidth that scanning the full resonator range was likely to yield a PLE peak.

Frequency steps were selected to be smaller than the lifetime limited linewidth of the emit-

ter under investigation. At each frequency step, the laser frequency was tuned via software command. When tuning was complete, the frequency was read out on the wavemeter to ensure the laser frequency was successfully tuned.

To avoid ionization, the emitter was reset and initialized at each frequency step via an off resonant (515 nm) "repump" pulse. In all experiments described in this thesis, the initialization period $t_{\text{init}} = 2\ \mu\text{s}$ was followed by a wait period $t_{\text{wait}} = 100$ ns and a data period of resonant excitation $t_{\text{data}} = 10\ \mu\text{s}$ during which APD counts were collected and integrated. This sequence, shown in Fig. 3.9, was repeated 5000 times at each frequency step to obtain the average behavior over many excitations and resets.

Figure 3.9: Pulse sequence and collection window for photoluminescence excitation experiments. The emitter is initialized by appling green repump laser for $t_{\text{init}} = 2\mu\text{s}$. After a wait period $t_{\text{wait}} = 100$ ns, resonant laser is applied and counts are collected on the APD for $t_{\text{data}} = 10\mu\text{s}$. The sequence is repeated 5000 times at each frequency step during the PLE scan to obtain the average fluorescence response.

The pulse sequence was synchronized by the PulseBlaster, which sent TTL pulses to the Cobolt laser and to the AOM drivers for the Velocity or EMM. SiV measurements performed with the SolsTiS utilized continuous wave resonant laser as two-photon excitation leading to ionization was not observed to be a significant problem. For each laser, the response latency was characterized and precompensated. APD counts were collected as TTL pulses into a NIDAQ input line and integrated during the resonant excitation period. During PLE measurements, the resonant laser and ZPL emissions were blocked from reaching the APD, and only phonon side band counts were collected. A summary of the filters used for

each relevant emitter is provided in Table 3.2.

Emitter	Debye-Waller factor	Reference	PLE filter used
NV	0.03	[24]	640 nm LP
SnV	0.6	[41]	640 nm LP
SiV	0.7	[44]	775/46 nm BP

Table 3.2: Debye-Waller factors. The Debye-Waller factor represents the fraction of the total fluorescence emitted into the zero-phonon line (ZPL), with the remaining fluorescence emitted into the phonon side band (PSB). For photoluminescence excitation (PLE) characterization, the resonant laser and ZPL are filtered out and only PSB photons are collected. The specific filters used for each emitter are listed.

The result of a typical PLE measurement on a single NV center in the confocal volume is shown in Figure 3.10. The measurement employed the pulse sequence in Fig. 3.9 and the Newport Velocity laser served as the resonant excitation laser. The splitting between the two peaks, shown in red, was 6.656 GHz, and the average position of the two peaks was 470.474 THz. Together, these metrics can be used to assess the strain environment of the color center, similar to the discussion presented in Chapter 2 for Group IV color centers.

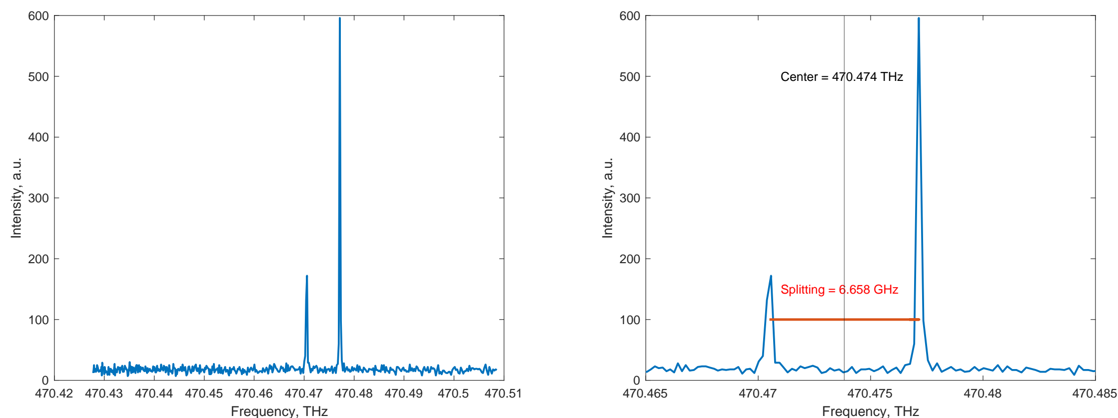

Figure 3.10: Typical photoluminescence excitation measurement. The left panel shows the results of a nitrogen vacancy PLE scan with 515 nm repump and 637 nm excitation using the pulse sequence described previously and shown in Fig. 3.9. The scan is centered on the center of the PL peak shown in Fig. 3.8 and spans the mode-hop free tuning range range of the Velocity laser. The right panel shows a zoomed-in version, with two clear narrow transitions split by 6.658 GHz and centered at 470.474 THz. Only the phonon sideband was collected on the APD.

Chapter 4

Characterization of SiVs in CVD diamond

4.1 Chemical vapor deposition of diamond

4.1.1 Principles

Chemical vapor deposition (CVD) of diamond involves generating favorable conditions for diamond growth using the chemical environment rather than the standard thermodynamically-required high temperature high pressure conditions. Typically, a single crystal diamond substrate is placed in contact with methane gas. When heated, the carbon plasma can deposit as a metastable diamond film on top of the single crystal seed. By engineering the growth times and temperatures, the properties of the resulting films can be modulated.

One advantage of CVD growth of diamond is that defects can be incorporated naturally during growth. These processes have been explored in depth for the incorporation of NV centers, particularly for sensing and magnetometry applications [45]. In-situ incorporation of SiVs in CVD diamonds has produced high quality color centers for quantum applications [46], including the demonstration of Hong-Ou-Mandel interference from distinct color centers [39]. The narrow inhomogeneous distribution of emitters represented a significant advance over typical implanted samples, which require postselection of emitters and/or strain en-

gineering [31] to tune distinct emitters into resonance. In this Chapter, we characterize the inhomogeneous distribution and optical transitions of SiVs produced in-situ in diamond grown via CVD.

4.1.2 Sample

The starting substrate was an ultralow strain single crystal diamond sourced from NDT. A diamond film was overgrown on the sample, and silicon was incorporated naturally during the growth process. Some of this silicon incorporated next to lattice vacancies to form SiVs. An optical micrograph of the film after growth is shown in Fig. 4.1.

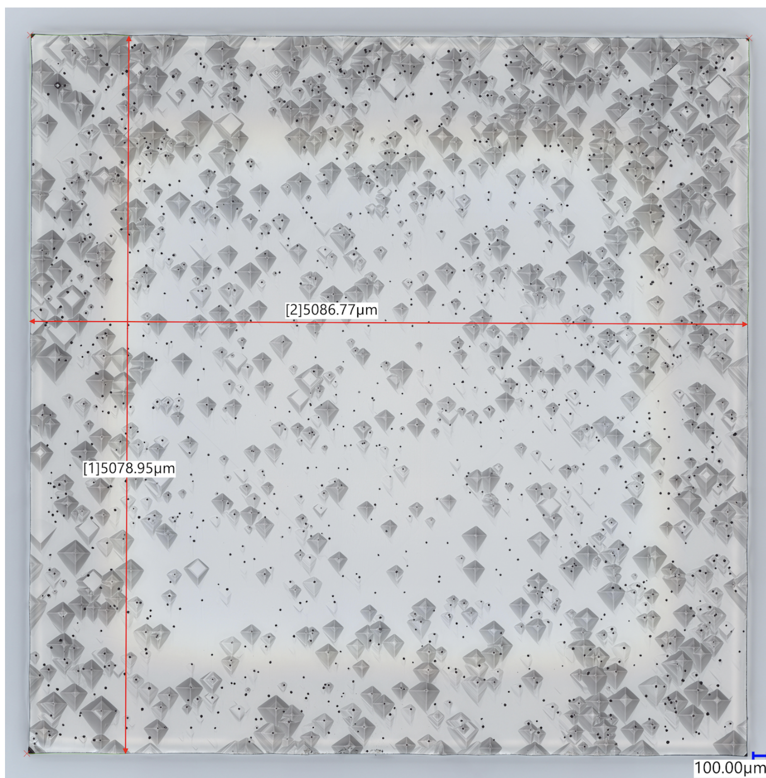

Figure 4.1: Optical micrograph of overgrown diamond. Growth pyramids are visible on top of the diamond film.

On top of the low-strain film, growth pyramids are visible. For the measurements reported in the subsequent sections of this thesis, we focus on the regions between growth pyramids to maintain a single focal plane.

4.2 Experimental results

4.2.1 Sample preparation

Following diamond growth, the sample was tri-acid cleaned in a 1:1:1 mixture of sulfuric, nitric, and perchloric acids at 345°C for 1 hour [38]. Immediately after tri-acid cleaning, the sample was cleaned in 3:1 sulfuric acid:hydrogen peroxide piranha solution for 5 minutes. The sample was then rinsed in an de-ionized (DI) water bath, then an isopropyl alchohol (IPA) bath, and finally dried with nitrogen gas. The sample was immediately transferred to a crucible for annealing to avoid organic contamination.

Following cleaning, the sample was annealed in a home-built high-vacuum furnace [47]. The furnace was pre-baked prior to the annealing run to remove residual adsorbed gas. After the sample was loaded, it was pumped to 2×10^{-8} mbar and annealed using the following temperature profile:

1. Ramp temperature to 400°C at 1°C/min
2. Hold at 400°C for 120 mins
3. Ramp temperature to 800°C at 1°C/min
4. Hold at 800°C for 120 mins
5. Ramp temperature to 1200°C at 1°C/min
6. Hold at 1200°C for 120 mins
7. Ramp temperature down to ambient temperature at -1°C/min

After annealing, the sample was tri-acid cleaned again to remove surface graphite, and cleaned in 3:1 sulfuric acid:hydrogen peroxide piranha solution using the processes described previously to remove any remaining organic contamination. The sample was then rinsed in DI water, transferred to methanol, and then critical point dried on a heated silicon substrate. The sample was transported between the clean room and the cryostat in a gel pak.

4.2.2 Photoluminescence measurements

The sample was mounted in the Montana Instruments cryostation using Ted Pella Inc PELCO colloidal silver paint, and the cryostation was pumped down to high vacuum (1×10^{-6} mbar) prior to cooling to its base temperature ~ 4 K. When the sample reached base temperature, the attocube stages were used to raise the sample into focus. A confocal image of flourescence from the overgrowth surface under 515 nm excitation is shown in Fig. 4.2. All subsequent data reported in this Chapter was collected using the cryogenic confocal microscope described in Chapter 3 and depicted in Figs. 3.2 and 3.5.

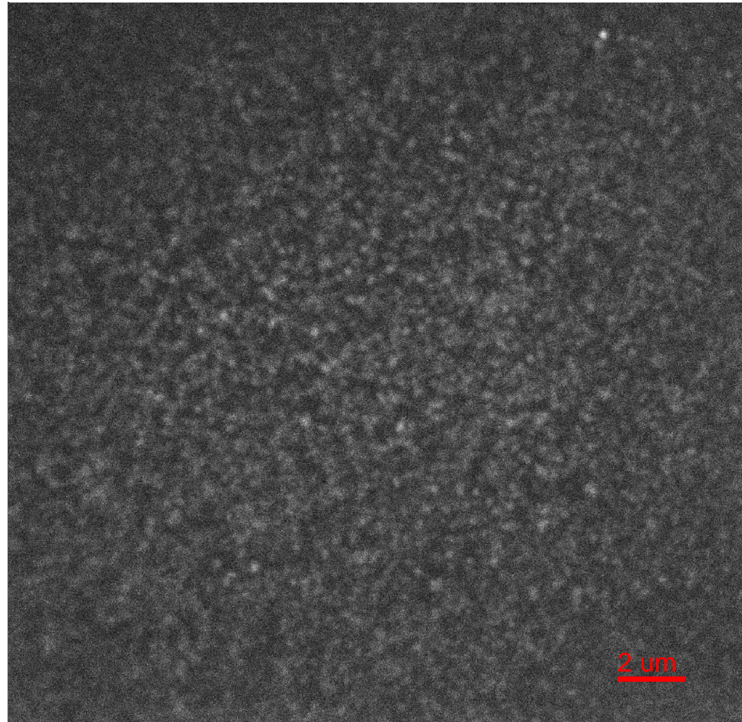

Figure 4.2: Confocal image of diamond overgrowth layer. THe diamond was illuminated with 515 nm excitation laser, and fluorescence above 640 nm was collected on the APD.

Candidate emitter sites were located with a peakfinding algorithm to find bright sites

amongst the background. First, the image was filtered with a spatial Gaussian bandpass filter with highpass and lowpass parameters. A 2D Gaussian kernel f_g was generated with standard deviation σ selected to match the diffraction limited spot size:

$$f_g(x,y) = e^{-\frac{(x^2+y^2)}{2\sigma^2}} \tag{4.1}$$

This kernel was discretized and convolved with the image $A(x,y)$ via discrete 2-dimensional convolution to yield a filtered image $C(x,y)$:

$$C(x,y) = \sum_i \sum_j A(i,j) f_g(x-i+1, y-j+1) \tag{4.2}$$

Here, the range of i and j in the sum spans the dimension of the image and the kernel. Finally, candidate emitter sites were located with a 2D Gaussian fit over the filtered image. This process is shown in Fig. 4.3.

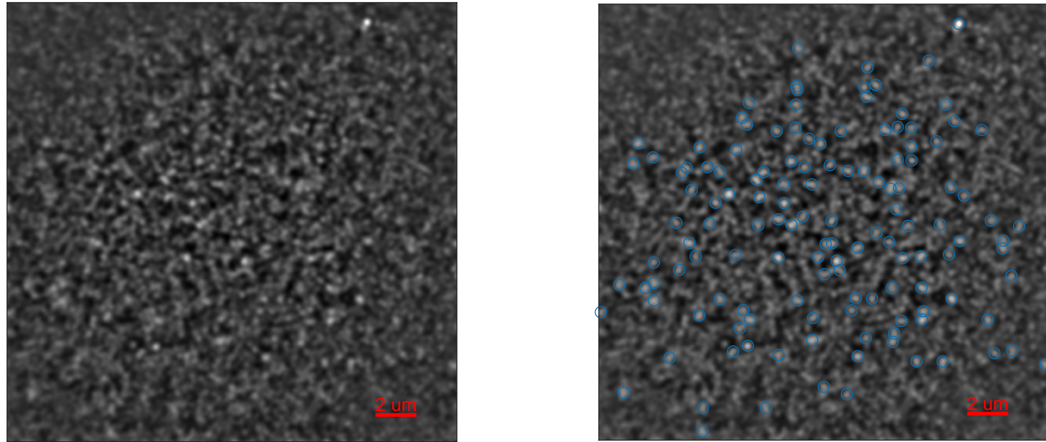

Figure 4.3: Image filtering and candidate emitter site selection. The left panel shows the bandpass-filtered confocal image of the diamond overgrowth layer which is expected to contain SiVs. The right panel shows the results of fitting 2D Gaussian peaks to the right confocal image. The peaks found served as candidate emitter sites for further investigation.

A PL spectrum was then obtained at each candidate site as described in Chapter 3.3. An example of one SiV PL peak and the Gaussian fit to it is shown in Fig. 4.4. For SiVs and

other Group IV emitters, the difference between ground and excited state splittings (Table 2.1) is sufficiently large such that two clear peaks appear for each emitter. For the SiV, the B and C transitions dominate at low temperatures [29].

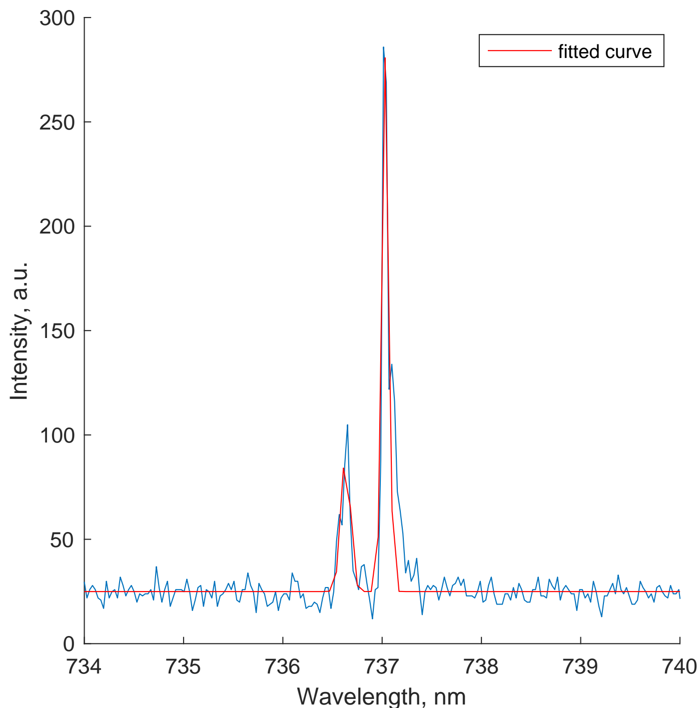

Figure 4.4: Example photoluminescence spectrum of silicon vacancy in overgrown sample. A PL spectrum (shown in blue) was collected under 515 nm excitation on the Princeton Instruments Isoplane spectrometer. The Gaussian fit peaks are overlaid in red. Two transitions are clearly visible, corresponding to the B and C transitions near 736.7 and 737.1 nm, respectively, shown in Fig. 2.2.

After peaks were fit to each candidate site, the candidate sites were further classified by whether they had a peak close to the expected SiV emission wavelength of 737 nm or not. An example of this classification process is shown in the left panel of Fig. 4.5, where candidate sites with a fit peak between 730 and 745 nm are shown with red circles, while sites with no peak in this range are shown with blue circles. The empirical inhomogeneous distribution of photoluminescence was then determined by computing the probability density of PL peak locations as a function of wavelength. The probability density function (PDF) was estimated using the kernel distribution given by

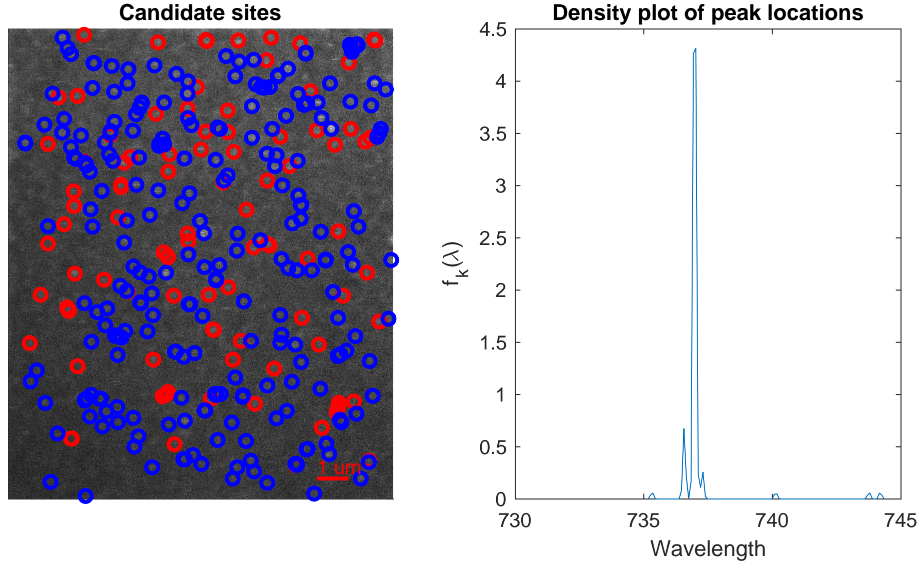

Figure 4.5: Candidate silicon vacancy sites and resulting photoluminescence inhomogeneous distribution Candidate sites were determined with 2D Gaussian peak fitting. A PL spectrum was then taken at each site. In the left panel, red circles represent sites that had a PL peak between 730 and 745 nm: these are SiV candidate sites. Blue circles did not have PL peaks in this range. The center frequencies of all SiV candidate sites were used to generate a kernel estimate of the empirical probability density function shown in the right panel.

$$f_k(\lambda) = \frac{1}{n}\sum_{i=1}^{n} K\big(\frac{\lambda - \lambda_i}{h}\big) \tag{4.3}$$

where n is the number of samples, λ_i are the sample values, K is the smoothing function, and h is the smoothing bandwidth. A Gaussian smoothing function with bandwidth σ was used:

$$K(\lambda) = e^{\frac{(\lambda - \lambda_c)^2}{2\sigma^2}} \tag{4.4}$$

This method generated an effective distribution around each data point and sums these distributions to generate a kernel estimate of the empirical probability density function. The bandwidth σ chosen to be the spectrometer limited bandwidth of 0.05 nm, and λ_c for each candidate site was set to be the center of the fit peaks at each candidate site. An example PDF for emitters found in one confocal region is shown in the right panel of Fig. 4.5.

To gain a better picture of the inhomogeneous distribution of PL across the sample, this process was repeated over multiple regions of the diamond surface. The PL PDFs for three

distinct regions are shown in Fig. 4.6.

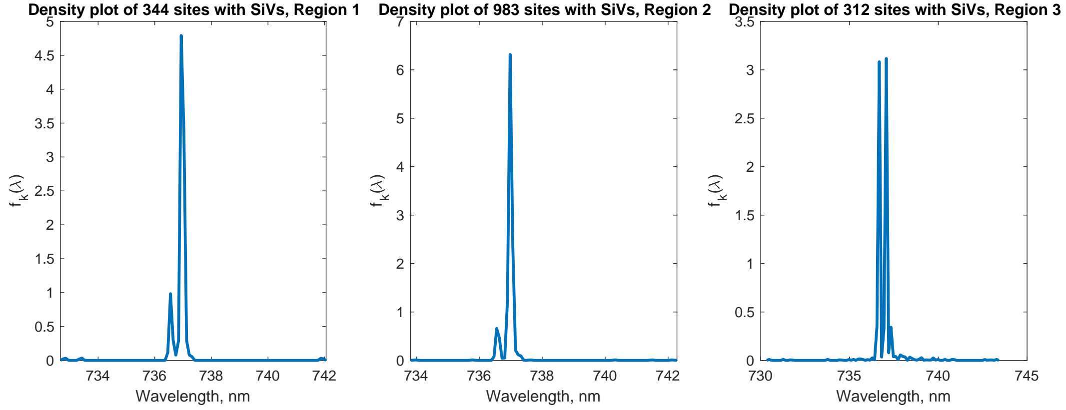

Figure 4.6: Inhomogeneous distribution of silicon vacancy photoluminescence in three regions of overgrown sample. Kernel estimates of the empirical probability density functions representing the inhomogeneous distribution of PL are shown for three distinct regions in the overgrown diamond layer. Region 1 represents 344 sites with fit peaks close to 737 nm, Region 2 represents 983 sites with peaks close to 737 nm, and Region 3 represents 312 sites with peaks close to 737 nm.

Data for Regions 1 and 2 were collected during a single cooling cycle, with the attocubes moved in between the two regions to reach a far-away spot on the surface of the diamond, while data for Region 3 was collected during a second cool-down. Region 1 comprises 344 sites with peaks fit close to 737 nm, while Region 2 and 3 comprise 983 and 312 such sites. Candidate sites in Region 1 were selected from a total sample area of 296 μm^2, while candidate sites in Region 2 span 407 μm^2 and in Region 3, 466 μm^2.

A kernel estimate of the empirical probability density function of all of the emitters in Fig. 4.6, representing the inhomogeneous distribution of PL in 1639 distinct candidate sites with peaks close to 737 nm, is shown in Fig. 4.7. The majority of the PL probability density was concentrated in two distinct peaks located close to 736.6 nm and 737 nm.

4.2.3 Photoluminescence excitation measurements

While photoluminescence is an efficient tool to understand the scope of the inhomogeneous distribution, further investigation is required to investigate key optical properties of the SiV

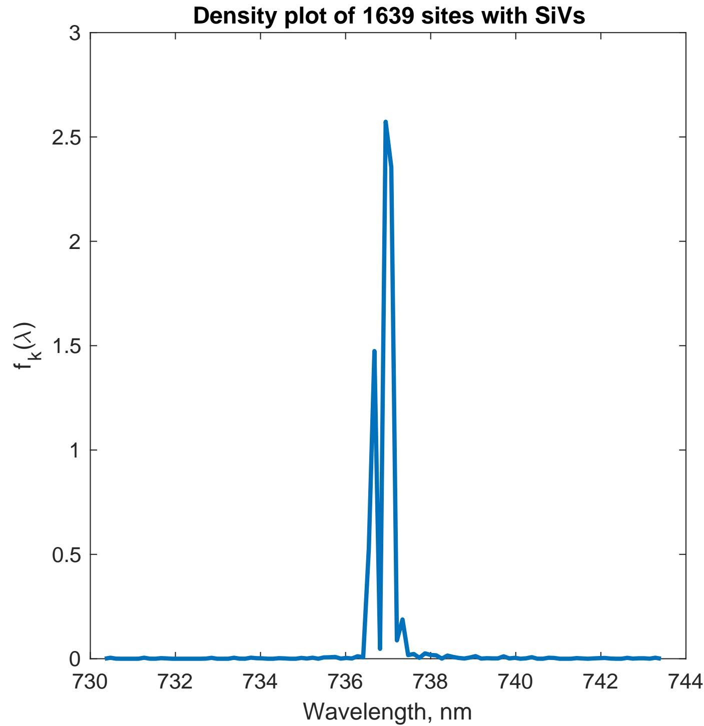

Figure 4.7: Summary of silicon vacancy photoluminescence inhomogeneous distribution in overgrown sample. A kernel estimate of the empirical probability density function plotted versus wavelength for 1639 individual sites with PL peaks near 737 nm is shown. Altogether, the PL peaks were measured across three distinct regions in the overgrown surface over two cooldowns.

population in the sample. The technique described in Chapter 3.3 was utilized for SiV PLE measurements, with resonant laser close to 737 nm provided by continuous wave excitation from a M^2 SolsTiS laser and pulsed 515 nm repump provided by the Cobolt laser. The pulse sequence scheme is shown in Fig. 3.9, though the intensity of resonant laser is not modulated as ionization was not observed to be a significant problem. An example of the experimental stack comprising a representative confocal image, PL spectrum, and PLE spectrum at one site is shown in Fig. 4.8.

This measurement was repeated over 113 candidate sites spanning two distinct regions in the diamond overgrowth layer, and peaks are fit to determine the center frequency and linewidth. Although the expected lineshape of the emitters in frequency space is Lorentzian, broadening processes can result in a deviation from Lorentzian behavior as described in Chapter 2.3.5. For this reason, pseudo-Voigt profiles are fit to each peak. Voigt profiles are a convolution

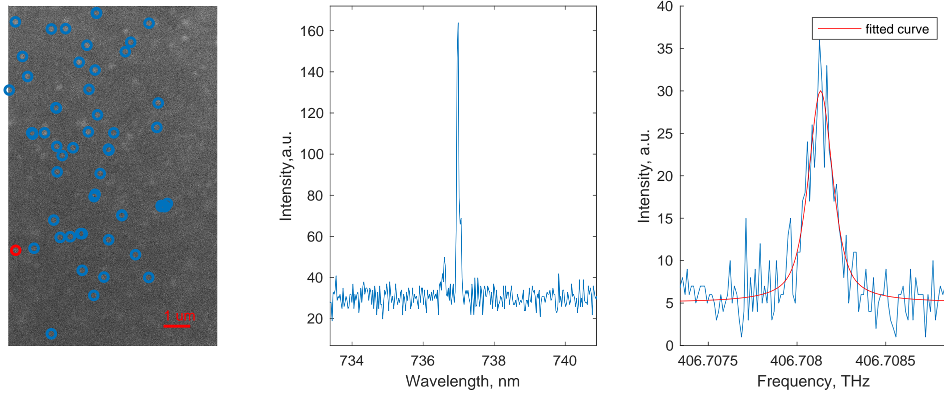

Figure 4.8: Experimental stack and peak fitting for a silicon vacancy in the overgrown sample. A confocal scan with candidate sites is shown in the left panel. The PL specrum associated with the site highlighted in red is shown in the center. The center of the Gaussian peak fit to the PL peak was used to center the resonant laser to obtain the PLE peak shown in the right panel. Finally, a Gaussian peak was fit to the PLE peak in the right panel.

of a Lorentzian with a Gaussian peak, and they capture how 'Lorentz-like' an experimental peak is via fit parameters. The pseudo-Voigt function uses a linear combination of a Gaussian and a Lorentzian instead of a convolution. The pseudo-Voigt profile used is given by:

$$f_v = a\left(\frac{e}{1+4(\frac{x-b}{c})^2} + (1-e)*\exp\big(-4\log(2)\big(\frac{x-b}{c}\big)^2\big)\right) + d \tag{4.5}$$

where the 5 fit parameters a, b, c, d, e represent the amplitude, center, composite width, offset, and Lorentzian-Gaussian ratio, respectively. For each peak fit, the value of b is used to determine the peak center, and the value of c is used to determine the peak width for generating the kernel estimate of the empirical probability density function for inhomogeneous distribution or linewidth.

The two regions were measured over the span of two cryostat cooling cycles that occurred approximately 4 months apart. A comparison of the two regions is provided in Fig. 4.9. In the left panels, an example of a representative PLE measurement at a single site in Region 1 (top) and Region 2 (bottom) is shown. Each peak was fit with a pseudo-Voigt function (Eq. 4.5). Then, in the center panels, a kernel estimate of the empirical probability density function of the center frequency of 56 PLE peaks in Region 1 (top) and 57 PLE peaks in Region 2 (bottom) highlights the narrow inhomogeneous distribution of C transitions over many

sites across the diamond. Finally, the right panels show histograms and kernel estimates of the empirical probability density functions of the linewidths of 56 SiV sites in Region 1 (top) and 57 SiV sites in Region 2. The PDFs are calculated using Eqs. 4.3-4.4.

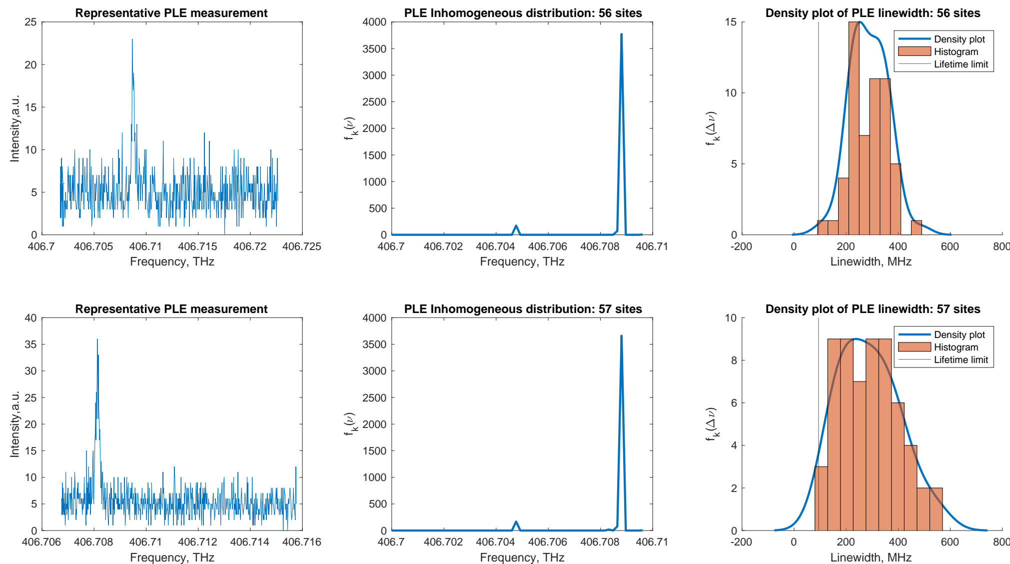

Figure 4.9: Comparison of photoluminescence excitation taken in two regions of the overgrown sample over two cooldowns. The top (bottom) row represents 56 (57) SiV sites from Region 1 (2). Representative PLE measurements are shown on the left. Aa kernel estimate of the empirical probability density function is computed for the frequency locations of the 56 (57) SiV sites in the center. A kernel estimate of the empirical probability density function of the emitter linewidths is shown with a histogram of linewidths measured in Region 1 (top) and Region 2 (bottom). No significant differences are observed between the two regions/cooldowns.

No significant differences were observed in the two populations of SiVs over the two regions. The top and bottom rows of Fig. 4.9 rows were combined into a summary of all 113 SiV sites over the two regions in Fig. 4.6. The kernel estimate of the empirical probability density function of the PLE peaks measured at all 113 sites was computed using Eqs. 4.3-4.4 and is shown in the left panel. A Gaussian fit to the PDF has standard deviation $\sigma = 73.5$ MHz ($2\sigma = 147$ MHz), which is about 1.56 times larger than the lifetime limit of the SiV. A histogram and the a kernel estimate of the empirical probability density function was computed using of the linewidth distribution over the 113 PLE sites is provided in the right panel of Fig. 4.10.

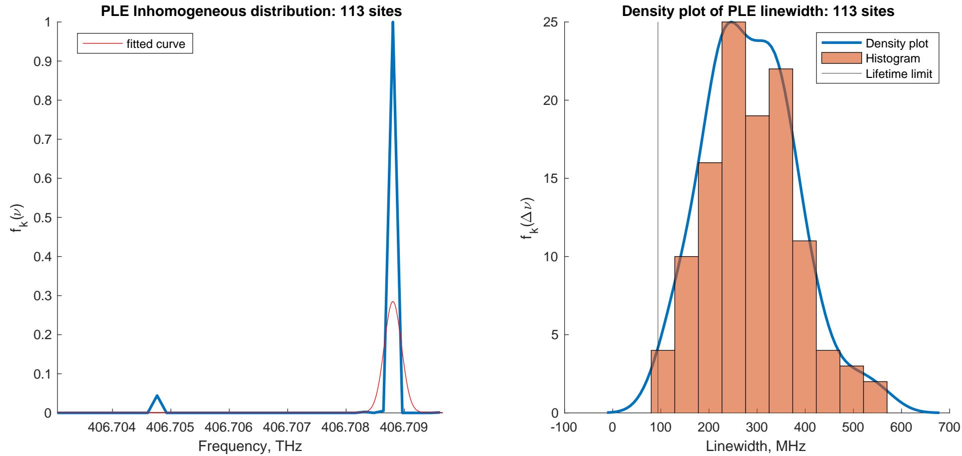

Figure 4.10: Summary of silicon vacancy photoluminescence excitation in the overgrown sample. The kernel estimate of the empirical probability distribution function associated with the center frequency of 113 PLE measurements is plotted in the left panel. On the right, a kernel estimate of the empirical probability density function associated with the linewidth of 113 PLE measurements is plotted, along with a histogram of linewidths measured. The lifetime limited linewidth for a single SiV center is indicated by a thin line at 94 MHz.

Finally, to explore the characteristics of the ground and excited state splittings, both the B and C transitions of SiV sites were measured in a third cooldown. A kernel estimation of the empirical probability density function representing the inhomogeneous distribution of PL peaks at 52 sites explored is shown in the left panel of Fig. 4.11.

Like the previous measurements of the C transition, the center PLE frequencies of these 52 sites were found to have a narrow inhomogeneous distribution around 406.709 THz, while the center frequencies of the B transitions in the same 52 sites were distributed around 406.920 THz, as shown in the left-center panel. Finally, the distribution of C transition linewidths is nearly 500 MHz narrower than the distribution of B transition linewidths, as shown in the right panels of Fig. 4.11.

The C transition linewidths summarized in the center left panel of Fig. 4.11 are overlaid on the confocal image to visualize the spatial distribution of SiV properties. No significant correlation between location on the sample and linewidth was observed.

Further, to investigate the spatial distribution of the energy spectra of SiVs in the overgrown

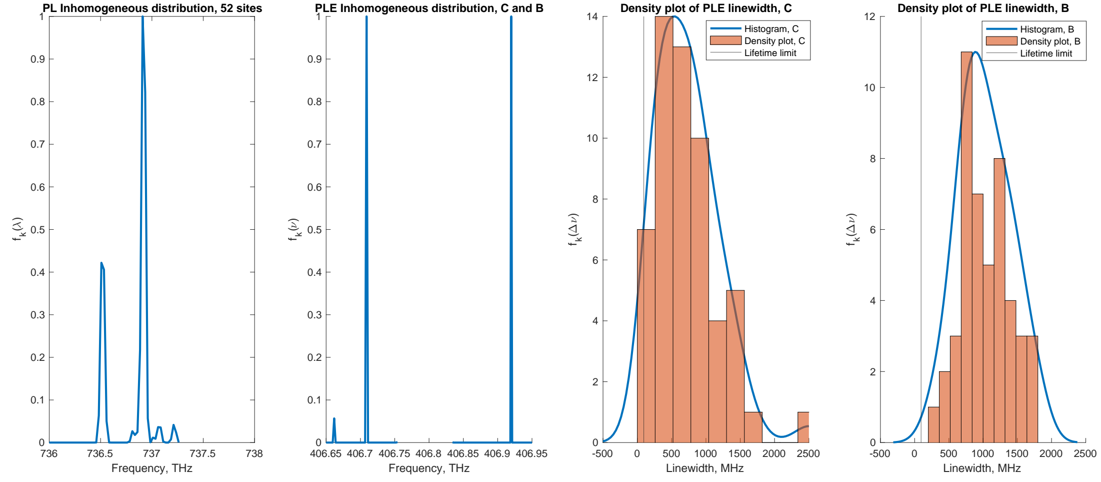

Figure 4.11: Inhomogeneous distribution of silicon vacancy B and C transitions in the overgrown sample. A kernel estimate of the empirical probability density function of PL peaks at 52 sites is shown in the left panel. The left-center panel contains a kernel estimate of the empirical probability density function for the center frequency of PLE measurements of the C and B transitions at the 52 sites. The C transition is located at 406.709 THz, and the B transition is located at 406.920 THz. Distributions of linewidths for the C and B transitions are shown in the right plots, with histograms and kernel estimates of the empirical linewidth probability density functions of each transition.

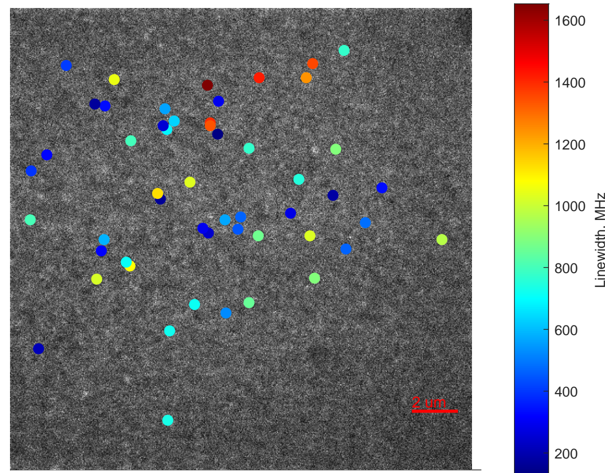

Figure 4.12: Spatial map of silicon vacancy linewidths in the overgrown sample. The fit linewidths, shown in the right-center panel of Fig. 4.11, of the 52 emitters measured are plotted spatially.

sample, the mean of the B and C transitions and the splitting between the B and C transitions are shown against spatial maps in the top panel of Fig. 4.13. Most of the emitters have

a splitting close to 211.3 GHz and a mean transition frequency of 484.8143 THz, indicating there was low residual strain remaining substrate following overgrowth. The relationship between the splitting between the B and C transitions and the mean frequency of the B and C transitions is plotted in the bottom panels of Fig. 4.13. The bottom left panel shows the relationship for all 52 emitters summarized in Figs. 4.11, and the right panel shows the primary group in detail.

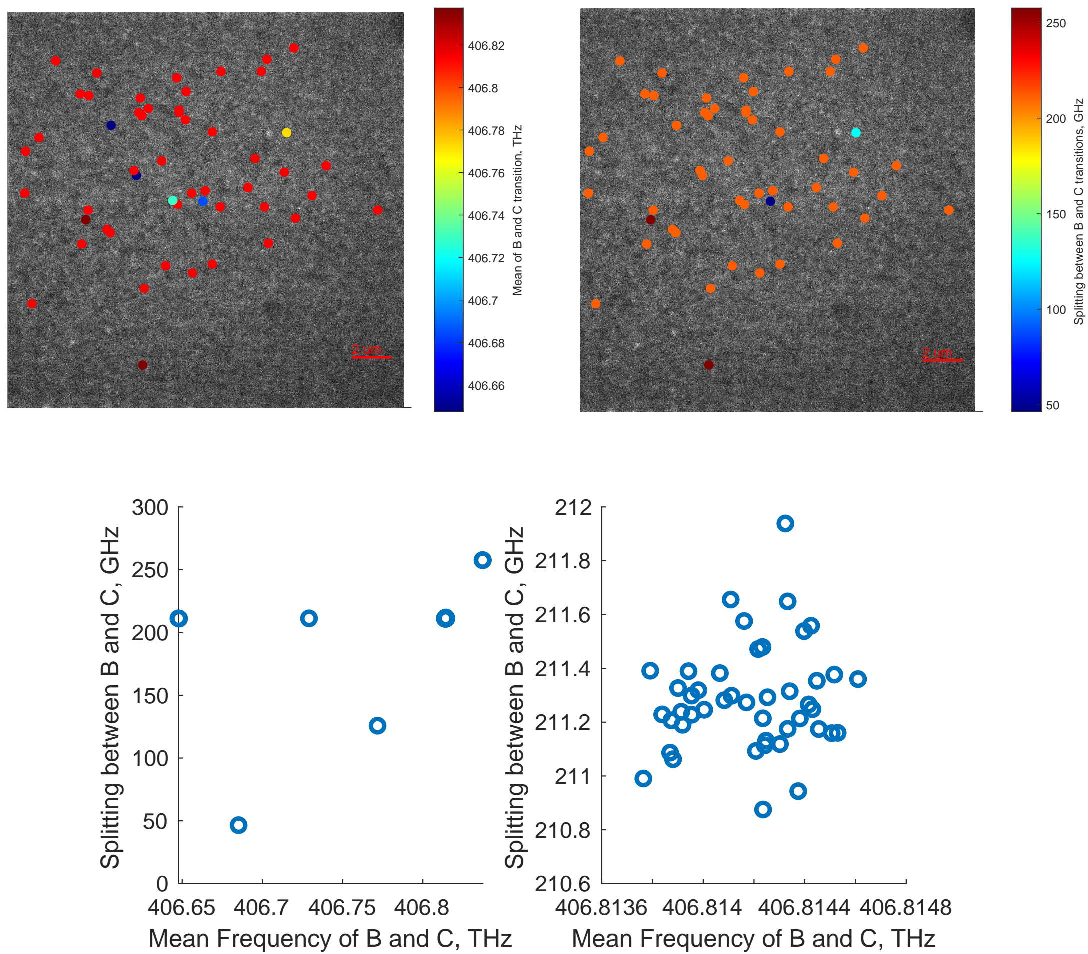

Figure 4.13: Spatial map of silicon vacancy optical properties in the overgrown sample. In the top left panel, the mean values of the B and C transitions at each site are plotted spatially. In the top right panel, the difference between the B and C transitions at all sites are plotted spatially. The center panels show this splitting between the B and C transitions as a function of the mean frequency of the B and C transitions for all 52 sites with SiVs. The bottom right panel shows the cluster close to a 211.3 GHz splitting and 406.8143 THz mean frequency in detail.

Chapter 5

Characterization of SnVs in HPHT-treated diamond

5.1 High pressure high temperature treatment

5.1.1 Principles

Tin vacancies in diamond have emerged as a promising Group IV color center, particularly due to their large ground state splitting, which could yield long spin lifetimes at higher temperatures than SiVs and GeVs [48]. Unfortunately, the optical properties of SnVs suffer from spectral diffusion [41]. The Sn atoms that make up the SnV centers are more massive and spatially large compared to the Si atoms in SiVs: the implantation process generates more vacancies and lattice damage for larger atoms [49]. It has also been shown that the linewidth of SnV centers decreases with higher annealing temperatures, but significant surface graphitization is observed in high temperature anneals [33].

High pressure high temperature (HPHT) treatment offers the ability to achieve the high temperatures thought to improve SnV optical properties while avoiding significant graphitization that occurs at atmospheric pressures. Seminal work in SnV spectroscopy has shown that applying pressure of 7.7 GPz enables an annealing temperature of 2100° C, which yielded a narrow inhomogeneous distribution of SnV emitters by effectively healing lattice damage

generated during the implantation process [33]. These results were confirmed and extended via the measurement of transform-limited linewidths in HPHT-treated diamond [41]. In this Chapter, we present characterization of the inhomogeneous distribution and linewidths of SnVs in two samples that are first implanted with tin, then overgrown, and finally HPHT treated using two different processes.

5.1.2 Samples

Two 2mm x 2mm electronics grade (EG) CVD diamonds from Element 6 served as the starting substrates. The samples will subsequently be referred to as Sample A and Sample B.

Sample A was sonicated in acetone for 5 minutes followed by IPA for 10 minutes upon receipt. Prior to ion implantation, a strain-relief etch was performed. Following cleaning in 3:1 sulfuric acid:hydrogen peroxide piranha solution for 5 minutes to remove organic contaminates, reactive ion etching (RIE) was performed with $ArCl_2$ gas for 4 hours (9.4 sccm Ar and 15 sccm Cl_2). Immediately following, a second RIE step was performed with 30 sccm O_2 gas for 15 minutes. Sample A was then sent out for bulk ion implantation at Innovion Corporation, and implanted with $1{\times}10^{11}/\text{cm}^2$ Sn-117 at 96 keV with a 7° tilt, aiming for shallow implantation at $\sim$ 30 nm. Sample A was then tri-acid cleaned, cleaned in 3:1 sulfuric acid:hydrogen peroxide piranha solution, and annealed using the process described in Chap. 4.2.1. The diamond was then overgrown at MIT Lincoln Laboratory targeting a 1 μm overgrowth layer. Finally, Sample A was sent to the National Institute for Materials Science of Japan for HPHT treatment, where it was annealed at 2100 ^{o}C under 7.7 GPa of pressure for 15 minutes.

Sample B was implanted with Sn on half of its surface with $1{\times}10^9/\text{cm}^2$, and on the other half, $1{\times}10^{11}/\text{cm}^2$ at 300 keV. Various nanostructures were fabricated on the surface for unrelated work. Following implantation and fabrication, Sample B was tri-acid cleaned, cleaned in 3:1 sulfuric acid:hydrogen peroxide piranha solution, and annealed using the process described in Chap. 4.2.1. The diamond was then overgrown at MIT Lincoln Laboratory targeting a 1

μm overgrowth layer. Finally, Sample B was sent to Element 6 for HPHT treatment, where it was annealed at 1850°C under 7-8 GPa of pressure for 10 minutes.

5.2 Experimental results

5.2.1 Sample preparation

Following HPHT treatment, the samples were sonicated for 5 minutes in acetone followed by 3 minutes in IPA and then cleaned in 3:1 sulfuric acid:hydrogen peroxide piranha solution for 5 minutes. Both samples were rinsed in DI water and then methanol and dried with nitrogen gas. Immediately prior to characterization, the samples were tri-acid cleaned by boiling in a 1:1:1 mixture of sulfuric, nitric, and perchloric acids at 345°C for 1 hour, cleaned in a 3:1 sulfuric acid:hydrogen peroxide solution for 5 minutes, rinsed in DI water, and rinsed in methanol.

5.2.2 Photoluminescence measurements

The samples were first investigated with photoluminescence (PL) measurements using 515 nm excitation from the Cobolt laser to gain a broad understanding of the optical properties of any tin vacancies remaining post-HPHT treatment. Photoluminescence was collected on the Princeton Instruments IsoPlane Spectrometer in the configuration described in Chap. 3 and shown in Figs. 3.2 and 3.5. A typical spectrum for each sample is shown in Fig. 5.1. For SnVs, the dominant peaks observed at $\sim$ 4 K correspond to the C and D optical transitions (Fig. 2.2), as the thermal occupation of the upper excited state branch is very low [33].

An example confocal region for Sample A is shown in Fig. 5.2. In the left panel, the confocal image is overlaid with the identified candidate sites. Candidate sites were classified by whether they had PL peaks near the expected SnV emission wavelength of 619 nm. Candidate sites with a fit peak between 610 and 630 nm are shown with red circles, while sites with no peak in this range are shown with blue circles. The inhomogeneous distribution of PL was then determined by finding the probability density of finding a peak as a function of

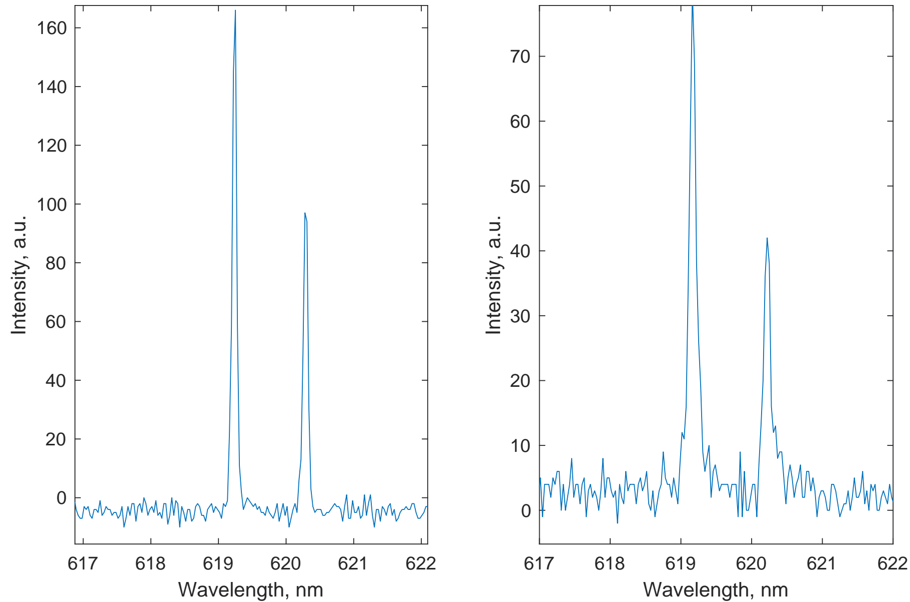

Figure 5.1: Example photoluminescence spectra of tin vacancy centers in high pressure high temperature-treated diamond samples. A typical photoluminescence spectrum under 515 nm excitation for one confocal site in Sample A is shown in the right panel, and one for Sample B is shown in the left panel.

wavelength. A kernel estimate of the empirical probability density function of the PL peaks was estimated using Eqs. 4.3-4.4, and is shown in the right panel of Fig. 5.2.

An example confocal region for Sample B is shown in Fig. 5.3. Peaks were classified, fit, and summarized using the same process as for Sample A. The left panel shows the candidate sites, where red circles indicate candidate sites that head PL peaks between 610 and 630 nm, and the right panel shows a a kernel estimate of the empirical probability density function of SnV PL calculated using Eqs. 4.3-4.4.

Confocal PL measurements were taken over several regions on each sample to investigate regional differences that may be caused by, for example, strain in the diamond. Confocal images were filtered as described in Chapter 4.2 using Eqs. 4.1-4.2, and candidate emitter sites were located with a 2D Gaussian fit over the filtered images.

The aggregate PL inhomogeneous distribution for each sample is shown in Fig. 5.4. The left

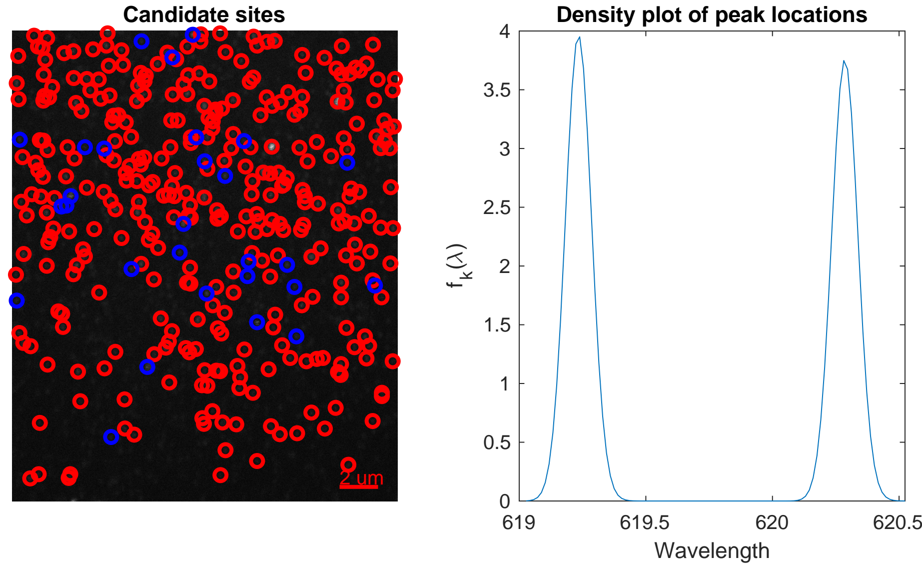

Figure 5.2: Candidate tin vacancy sites and resulting photoluminescence inhomogeneous distribution for Sample A. Candidate sites were determined with 2D Gaussian peak fitting. A PL spectrum was then taken at each site. In the left panel, red circles represent sites that had a PL peak between 610 and 630 nm: these are SnV candidate sites. The center frequencies of all 324 SnV candidate sites were used to generate a kernel estimate of empirical probability density function of SnV PL shown in the right panel.

panel shows a kernel estimate of the empirical probability density function of the location of PL peaks for 1733 SnV sites over four regions of Sample A, and the right panel shows a a kernel estimate of the empirical probability density function of the location of PL peaks for 1677 SnV sites over two regions of Sample B. The kernel estimates were computed using Eqs. 4.3-4.4. No significant regional differences are observed, and the C and D transitions remain clearly distinguishable even over thousands of confocal sites.

At the edge of Sample A, relatively few SnVs are observed. However, fluorescence from SiVs at 737 nm is prevalent close to the edge of Sample A, along with a bright, narrow peak at 720 nm. Two example PL spectra from the edge of Sample A are shown in Fig. 5.5. In the left panel, a PL spectrum taken at one confocal site at the edge of the chip has a strong SiV peak at 737 nm, a strong peak at 720 nm, and no evidence of SnV fluorescence. In the right panel, a PL spectrum taken at a confocal site about 20 um in from the edge of the Sample A has SiV fluorescence at 737 nm, the strong 720 nm peak, and two clear peaks close to 620 nm that are from SnVs. The intensity of the SiV signal from the edge of Sample A

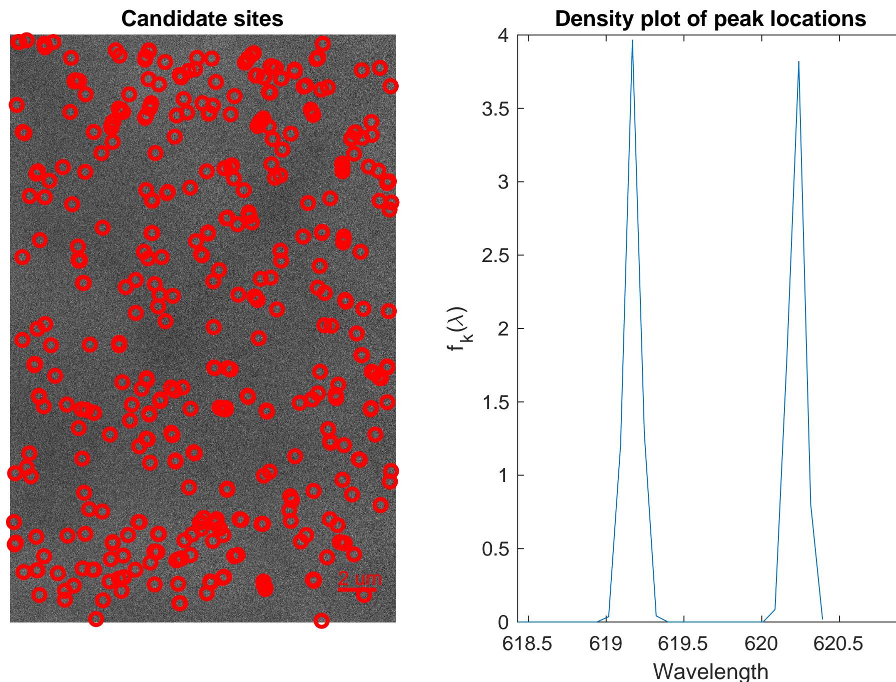

Figure 5.3: Candidate tin vacancy sites and resulting photoluminescence inhomogeneous distribution for Sample B. Candidate sites were determined with 2D Gaussian peak fitting. A PL spectrum was then taken at each site. In the left panel, red circles represent sites that had a PL peak between 610 and 630 nm: these are SnV candidate sites. The center frequencies of all 427 SnV candidate sites were used to generate a a kernel estimate of the empirical probability density function shown in the right panel.

(left panel) is much brighter than that further towards the center of Sample A (right panel), though the two spectra were taken within 5 minutes using the same excitation power and integration time: this indicates that there may be many more SiVs in the confocal spot near the edge of the chip.

The SiVs observed likely originate from the overgrown layer, and the fact that they are observed only at the edge of the sample can be attributed to inhomogeneity in the application of pressure during HPHT treatment. A summary of PL measurements covering 600-800 nm taken near the edge of the chip is presented in Fig. 5.6. The left panel shows all candidate sites with circles: the edge of the chip is observed to be bright in the bottom-left corner of the left panel. Candidate sites that had PL peaks at 720 nm and 737 nm are shown as red circles, and candidate sites that had PL peaks at 720 nm, 737 nm, and 620 nm are shown as black circles. The right panel shows a kernel estimate of the empirical probability

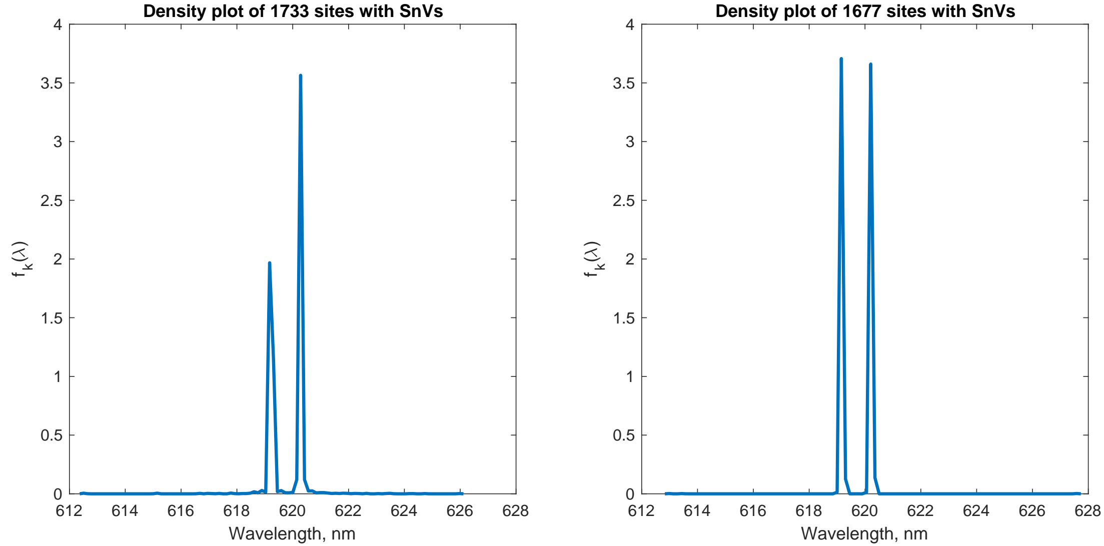

Figure 5.4: Inhomogeneous distribution of tin vacancy photoluminescence for two high pressure high temperature-treated samples. A kernel estimate of the empirical probability density function for the location of photoluminescence peaks for 1733 SnV PL sites in Sample A (left panel) and 1633 SnV PL sites in Sample B (right panel). In both samples, the B and C transitions are clearly visible and distinct.

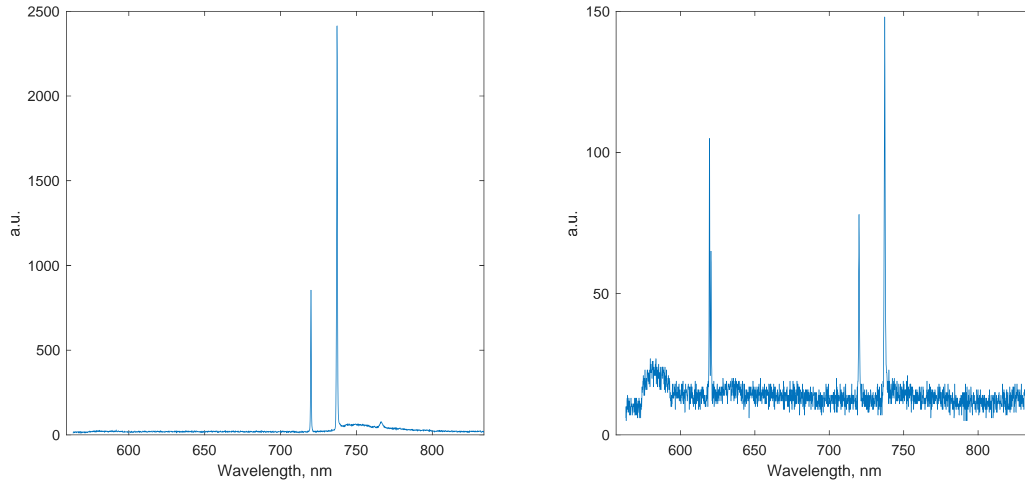

Figure 5.5: Silicon vacancy and 720 nm photoluminescence peaks observed in high pressure high temperature-treated Sample A. In the left panel, a PL spectrum taken at the edge of the chip has optical signature of SiVs at 737 nm as well as a strong, narrow peak at 720 nm. In the right panel, a PL spectrum taken further in towards the center of the sample has the same optical signatures as well as 620 nm peaks attributed to SnVs.

density function of the SiV PL peaks calculated using Eqs. 4.3-4.4 for peaks between 700 and 800 nm. Photoluminescence close to 720 nm has been previously reported in diamond, and was attributed to Ni-related defects [50].

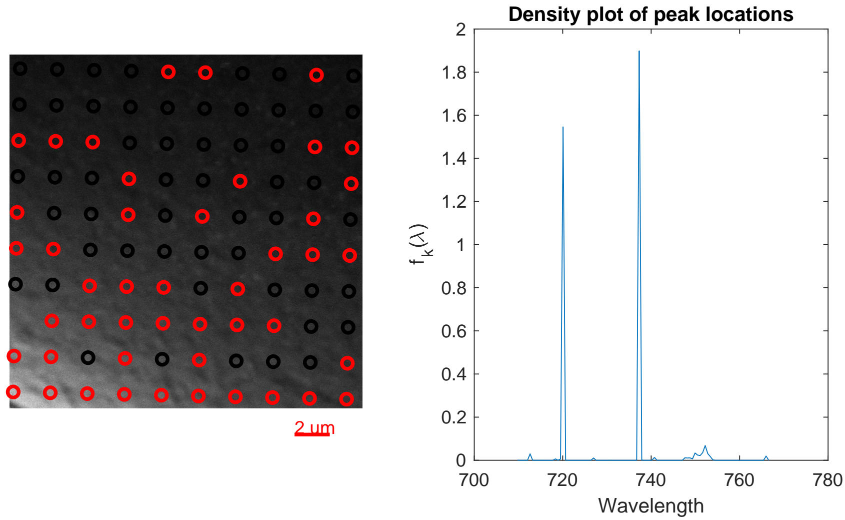

Figure 5.6: Candidate sites and resulting photoluminescence for silicon vacancy centers in Sample A. A grid of candidate sites was selected at the edge of the chip, and a PL spectrum was taken at each site. In the left panel, red circles represent sites that had peaks at both 720 nm and 737 nm, while the black circles represent sites that had peaks at 720 nm, 737 nm, and 620 nm. The center frequencies of all peaks between 700 nm and 800 nm were used to generate a kernel estimate of the empirical probability density function for the non-SnV peaks observed.

In Sample A, SiV signal was only observed at the edge of the chip. However, in Sample B, fluorescence at 737 nm was observed over the entirity of the sample, co-located in the same confocal region as the SnVs. A typical spectrum from Sample A including SiV signal is shown in Fig. 5.7. In contrast to the typical spectra at the edge of Sample A presented in Fig. 5.5, the SnV peak in Sample B is stronger than the SiV peak, and no 720 nm peak was observed.

A summary of PL measurements taken spanning 600-800 nm taken in the center of Sample B is shown in Fig. 5.8. Candidate sites that had PL peaks at both 620 nm and 737 nm are shown in yellow. Unlike in Sample A, no peaks were observed at 720 nm, though SiV signal persisited throughout the sample. The right panel shows a kernel estimate of the empirical probability density function of the SiV PL calculated using Eqs. 4.3-4.4 for peaks between 700 and 800 nm. The SiVs likely originated in the overgrowth layer, and appear to have remained in the sample and optically active following HPHT treatment.

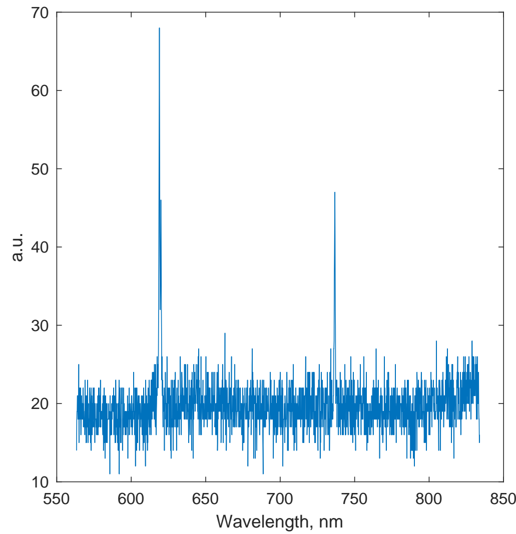

Figure 5.7: Silicon vacancy photoluminescence peaks observed in high pressure high temperature-treated Sample B. A PL spectrum taken in the middle of Sample B has optical signatures of SiVs at 737 nm as well as SnV peaks at 620 nm.

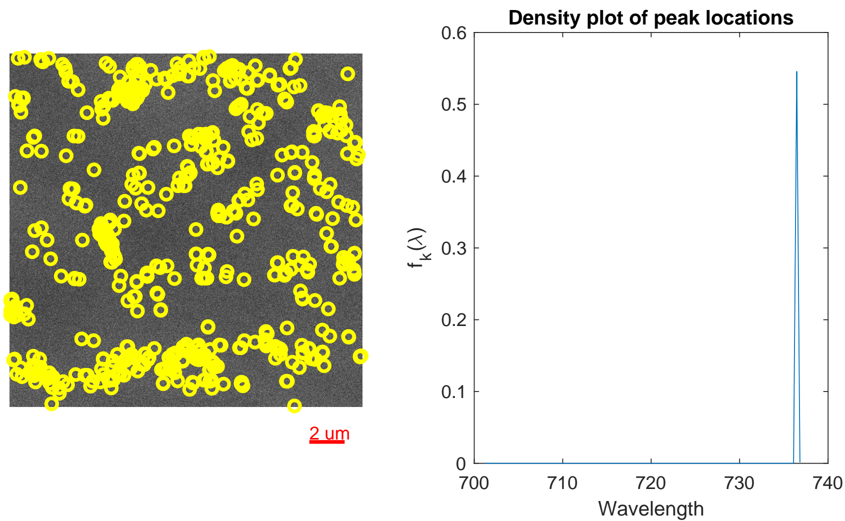

Figure 5.8: Candidate sites and resulting photoluminescence for silicon vacancy centers in Sample B. Candidate sites were determined with 2D Gaussian peak fitting. A PL spectrum was then taken at each site. In the left panel, yellow circles represent sites that head a PL peak near 620 nm and a PL peak near 737 nm. The center frequencies of all peaks between 700 nm and 800 nm were used to generate a kernel estimate of the empirical probability density function for the non-SnV peaks observed.

5.2.3 Photoluminescence excitation measurements

Following photoluminesence measurements, photoluminescence excitation measurements were taken to assess the inhomogeneous distribution within the spectrometer-limited distributions shown in Figs. 5.2-5.3 and the emitter linewidths. The technique described in Chapter 3.3 was utilized for SnV PLE measurements, with pulsed resonant laser close to 620 nm provided by an M^2 EMM and pulsed 515 nm repump provided by the Cobolt laser. The pulse sequence scheme is shown in Fig. 3.9. Peaks were fit with pseudo-Voigt functions (Eq. 4.5). A summary of PLE measurements for Sample A is given in Fig. 5.9. The left panel shows the results of a typical PLE measurement. A kernel estimate of the empirical probability density function of PLE center frequencies is shown in the center panel, representing the inhomogeneous distribution of the C transition of 70 SnV peaks that were fit. The inhomogeneous distribution is centered at 484.144 THz and has a standard deviation of σ = 4.51 GHz (2σ =9.13 GHz). Finally, a histogram of linewidths of the 70 peaks as well as a kernel estimate of the empirical probability density function of SnV linewidths calculated with Eqs. 4.3-4.4 are shown in the left panel.

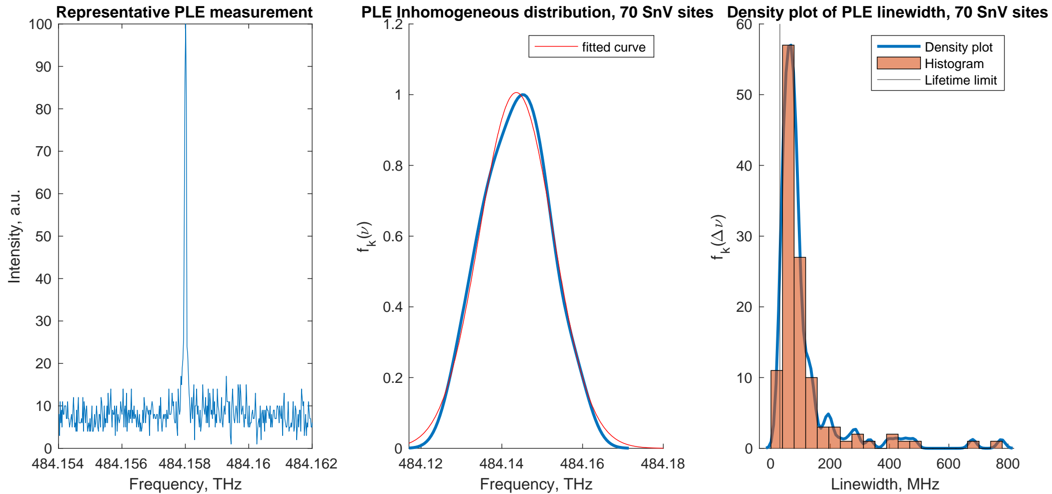

Figure 5.9: Summary of tin vacancy photoluminescence excitation in high puressure high temperature-treated Sample A. In the right panel, a typical PLE spectrum at one site in Sample A is shown. A kernel estimate of the empirical probability distribution function associated with the center frequency of 70 PLE peaks is plotted in the center panel. On the right, the kernel estimate of the empirical probability density function associated with the linewidth of 70 PLE peaks is plotted, along with a histogram of linewidths measured. The lifetime limited linewidth for a single SnV center is indicated by a thin line at 35 MHz.

This process was repeated for 25 SnV peaks in Sample B, as shown in Fig. 5.10. A typical PLE spectrum is shown in the left panel, and each peak was fit with a pseudo-Voigt peak (Eq. 4.5). A kernel estimate of the empirical probability density function of center frequencies is calculated using Eqs. 4.3-4.4 and is shown in the center panel. The inhomogenous distribution was fit with a Gaussian peak that is centered at 484.198 THz with a standard deviation of $\sigma = 2.40$ GHz ($2\sigma = 4.80$ GHz). The rightmost panel shows a histogram of linewidths of the 25 peaks as well as aa kernel estimate of the empirical probability density function of the SnV linewidths calculated using Eqs. 4.3-4.4.

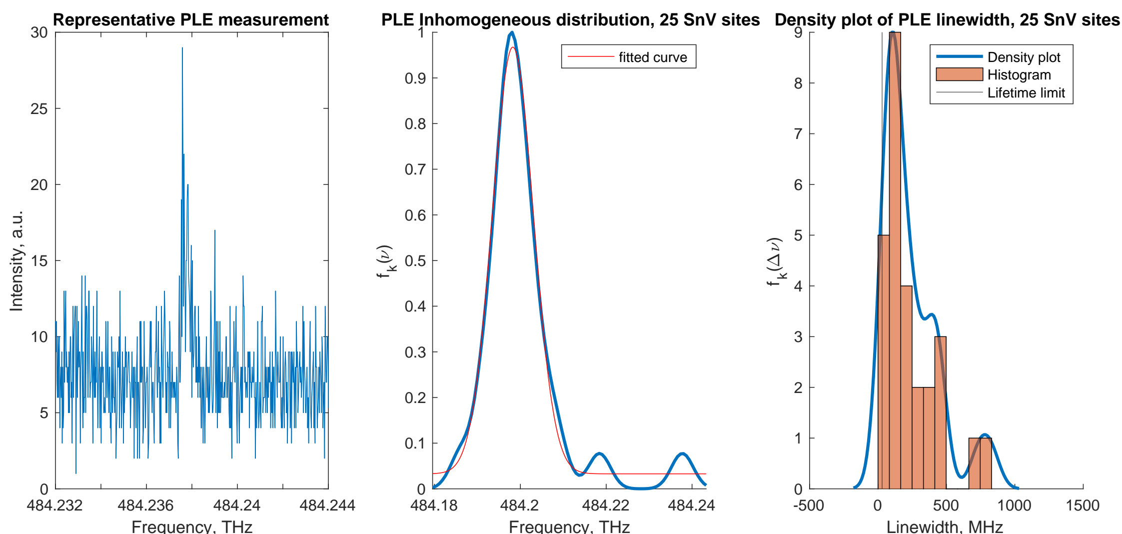

Figure 5.10: Summary of tin vacancy photoluminescence excitation in high pressure high temperature-treated Sample B. In the right panel, a typical PLE spectrum at one site in Sample B is shown. A kernel estimate of the empirical probability density function associated with the center frequency of 70 PLE peaks is plotted in the center panel. On the right, a kernel estimate of the empirical probability density function associated with the linewidth of 70 PLE peaks is plotted, along with a histogram of linewidths measured. The lifetime limited linewidth for a single SnV center is indicated by a thin line at 35 MHz.

Chapter 6

Widefield microscopy for efficient optical characterization

6.1 Focused-ion beam implantation

6.1.1 Principles

Focused ion beam implantation (FIB) has been widely used in the semiconductor industry, and was more recently applied to diamond to control the placement of color centers. Targeted implantation of Si ions with FIB enabled direct placement of SiVs into nanostructures such as 2D photonic crystal nanocavities and waveguides. Though the FIB process is non-deterministic in that the yield of SiV creation ranges from 0-3% of the implanted dose of Si ions depending on implantation parameters, the lateral straggle can be in the tens of nm [15, 51].

6.1.2 Sample

A 2×2 mm electronics grade CVD sample from Element 6 served as the starting substrate. First, a strain relieving etch was performed by reactive ion etching (RIE) with $ArCl_2$ gas for 4 hours (9.4 sccm Ar and 15 sccm Cl_2). A second RIE etch in O_2 gas for 15 minutes (30 sccm) immediately followed. The sample was then cleaned in 3:1 sulfuric acid:hydrogen peroxide piranha solution. The sample was then patterned with FIB markers and Quick

Reference (QR) coordinates as described in [43]. Focused ion beam implantation of Si and Sn was performed at Sandia National Laboratory using a range of implantation densities and energies. Widefield images taken of the sample after FIB-implantation and cleaning at room temperature are provided in Fig. 6.1.

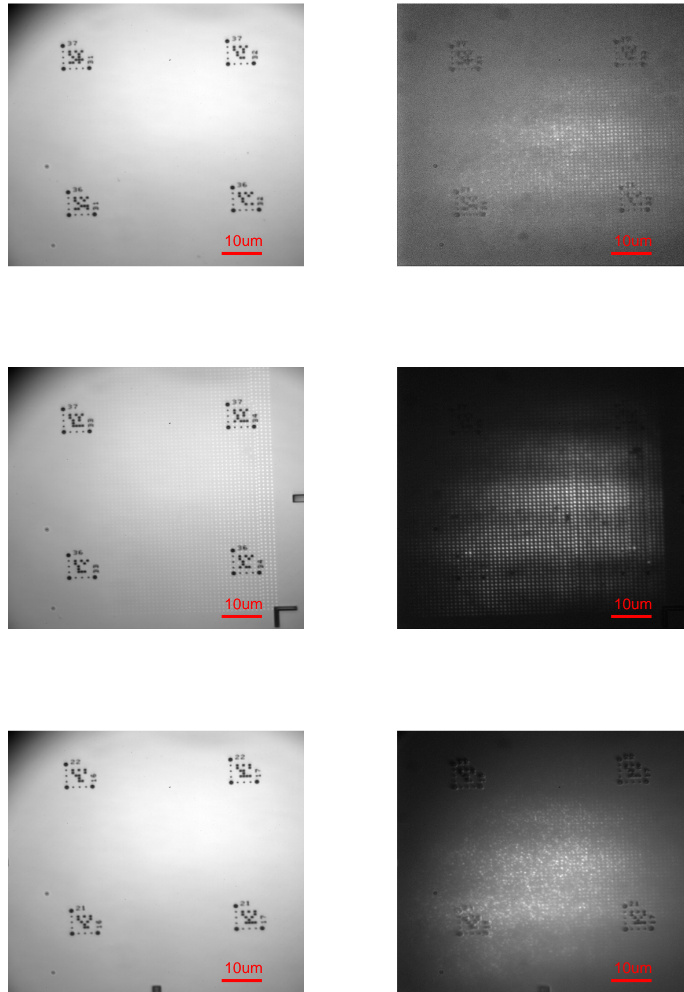

Figure 6.1: Room temperature widefield microscopy of focused ion beam-implanted sample. Typical images of QR-coded regions on the sample are shown in each row, with the left column illuminated with incoherent white light, and the right column illuminated with 532 nm laser and using bandpass filters around 737 nm (for SiVs) or 620 nm (for SnVs). The top row is representative of a region implanted with a low dosage of Si ions: fluorescence from the FIB sites is visible as a grid. The middle row is representative of a high Si ion dose: lattice damage at the FIB sites is clearly visible even in the white light image. The bottom row is representative of a region implanted with Sn ions.

6.2 Experimental results

6.2.1 Sample preparation

Following FIB implantation, the sample was cleaned in a 3:1 sulfuric acid:hydrogen peroxide piranha solution for 5 minutes. It was rinsed in DI water and then methanol and dried with nitrogen gas. The sample was then tri-acid cleaned by boiling in a 1:1:1 mixture of sulfuric, nitric, and perchloric acids for 345°C for 1 hr. Finally, the sample was cleaned again in a 3:1 sulfuric acid:hydrogen peroxide piranha solution for 5 minutes, rinsed in DI water, rinsed in methanol, and dried with nitrogen gas.

6.2.2 Photoluminescence measurements

The sample was first investigated with photoluminescence (PL) measurements. The sample was illuminated with 515 nm excitation from the Cobolt laser, and PL was collected on the Princeton Instruments IsoPlane Spectrometer in the configuration described in Chapter 3. As in the previous Chapters, confocal PL measurements were taken over several regions on the sample. An example region implanted with Si ions is shown in Fig. 6.2. In the left panel, candidate sites were identified using a 2D Gaussian fitting; sites that had a peak between 730 nm and 745 nm are shown as red circles. The FIB grid with implantation sites spaced at 1 μm is clearly visible. The right panel shows a kernel estimate of the empirical probability density function of SiV PL calculated using Eqs. 4.3-4.4.

Similarly, an example region that was FIB implanted with Sn ions is shown in Fig. 6.3. In the left panel, candidate sites were identified using a 2D Gaussian fitting; sites that had a peak between 610 nm and 630 nm are shown as red circles. As with the SiV implantation sites, the FIB grid with implantation sites spaced at 1 μm is clearly visible. The right panel shows a kernel estimate of the empirical probability density function of SnV PL calculated using Eqs. 4.3-4.4.

These measurements were repeated over seven SiV and seven SnV regions on the sample, and the aggregate distributions of PL peaks are shown in Fig. 6.4. In the left panel, a

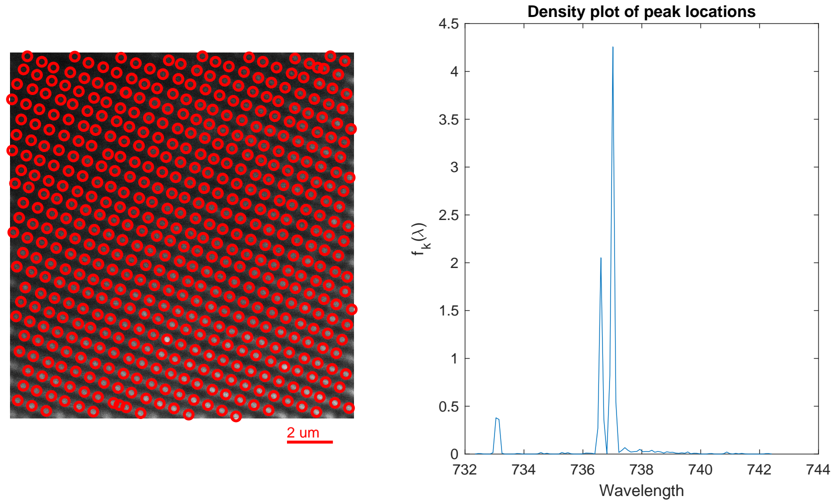

Figure 6.2: Candidate silicon vacancy sites and resulting photoluminescence inhomogeneous distribution in focused ion beam-implanted sample. Candidate sites were determined with 2D Gaussian peak fitting. A PL spectrum was then taken at each site. In the left panel, red circles represent sites that had a PL peak between 730 and 745 nm: these are SiV candidate sites. The center frequencies of all 530 SiV candidate sites were used to generate a kernel estimate of the empirical probability density function shown in the right panel.

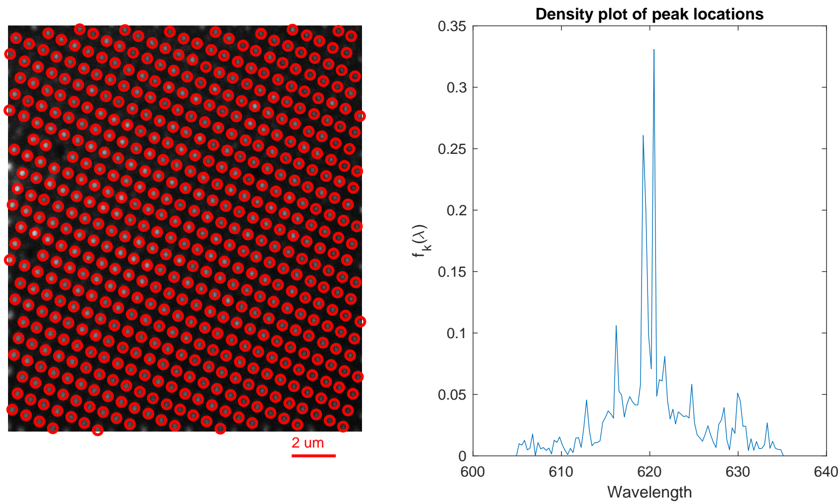

Figure 6.3: Candidate tin vacancy sites and resulting photoluminescence inhomogeneous distribution in focused ion beam-implanted sample. Candidate sites were determined with 2D Gaussian peak fitting. A PL spectrum was then taken at each site. In the left panel, red circles represent sites that had a PL peak between 610 and 630 nm: these are SnV candidate sites. The center frequencies of all 553 SnV candidate sites were used to generate a kernel estimate of the empirical probability density function shown in the right panel.

kernel estimate of the empirical probability density function for the center of PL peaks fit at 11,010 sites with SiVs is shown. Most of the probability density is concentrated in two clear transitions close to 737 nm, though broad peaks at 733 nm contribute to a smaller

rise in probability density at that wavelength. Additionally, there is a non-zero fall-off of probability density at wavelengths higher than 737 nm. The right panel has a kernel estimate of the empirical probability density function for the center of PL peaks fit at 2,668 sites with SnVs. The inhomogeneous distribution of SnV PL is quite broad, with non-zero probability to find a peak extending over close to 20 nm.

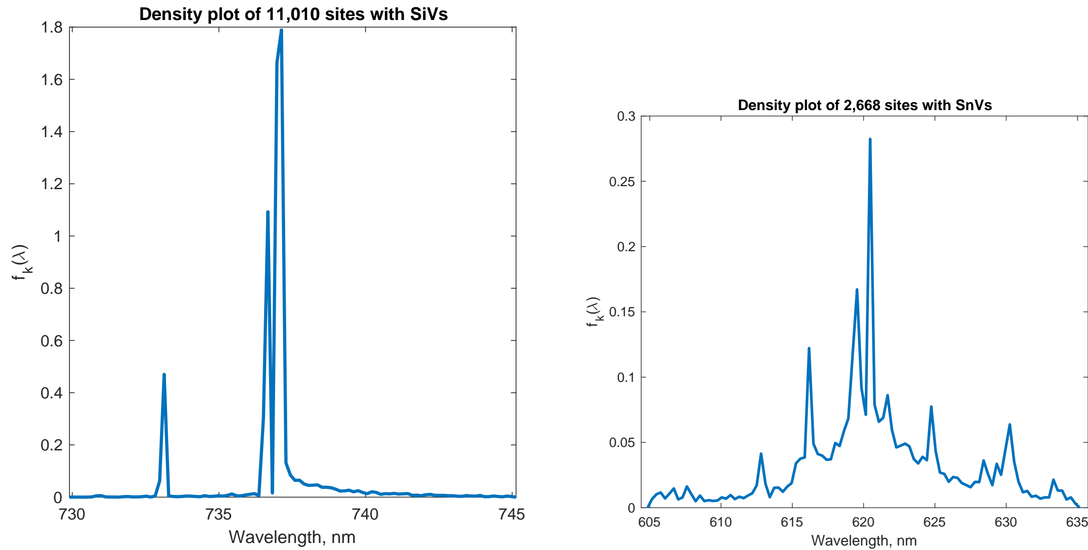

Figure 6.4: Summary of silicon vacancy and tin vacancy photoluminescence inhomogeneous distribution in focused ion beam-implanted sample. In the left panel, a kernel estimate of the empirical probability density function for the location of photoluminescence peaks was calculated for 11,010 sites with SiVs. In addition to peaks in probability density close to 737 nm representing the B and C transitions of the SiV, there is a peak in probability density close to 733 nm and a broad fall-off at wavelengths higher than 737 nm. In the right panel, a kernel estimate of the empirical probability density function was calculated for the location of photoluminescence peaks for 2,668 sites with SnVs is plotted as a function of wavelength. The probability density to find a peak extends from 613 nm to 632 nm, with regions of high probability centered at 620 nm.

6.2.3 Widefield photoluminescence excitation measurements

To multiplex characterization of color centers, PLE was then collected in widefield mode as shown in Fig. 3.4. The field of view of the widefield microscope is shown in Fig. 6.5, which shows an entire QR code region under white light illumination. This region was implanted with ^{29}Si spaced at 1 μm at 180 keV. To measure PLE, the resonant laser was swept over

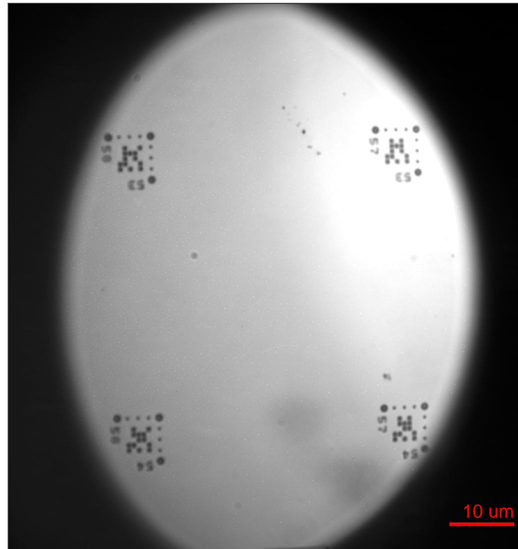

Figure 6.5: Widefield field of view. A single QR region on the FIB-implanted sample is shown under white light illumination. The widefield field of view is oblong as the image is laterally clipped by a mirror just before the EMCCD camera, but the entire QR region remains in view.

its mode-hop free tuning range in frequency steps much smaller than the emitter lifetime, and weak 515 nm Cobolt laser was applied continuously to repump the emitters. For SiVs, the M^2 SolsTiS laser served as the resonant laser. Tuning was accomplished by applying an external voltage to the SolsTiS resonator: this voltage was controlled by the NIDAQ. The resonator was tuned in voltage steps that corresponded to 10 MHz steps in frequency, and the frequency was read out on the wavemeter at each step to ensure tuning was successful. Once tuning was complete, the EMCCD was exposed for 1 s. An example image generated during this 1 s exposure period is shown in Fig. 6.6. In this case, the laser was locked to 405.8971 THz.

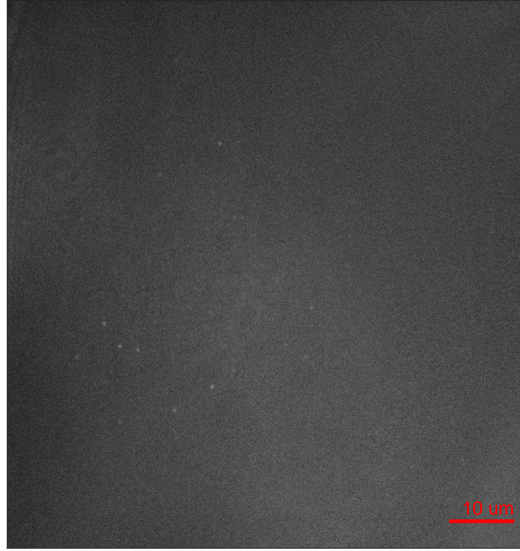

Figure 6.6: Raw widefield image under resonant excitation. In this example, the entire widefield field of view is shown while the resonant laser is locked to 405.8971 THz. Resonant laser was applied continuously along with weak 515 nm repump, and the image was exposed on the camera for 1 s. A few emitters are excited and visible as diffraction-limited spots.

The raw image was first cropped to remove area outside the QR region, as shown in the left panel of Fig. 6.7. Then, the image was filtered with a 2D Gaussian filter. The 2D Gaussian kernel f_g was generated with standard deviation $\sigma = 2$ pixels selected to match the diffraction limited spot size:

$$f_g(x, y) = e^{-\frac{(x^2+y^2)}{2\sigma^2}} \tag{6.1}$$

At each frequency step ν, this kernel was discretized and convolved with the image $M_\nu(x, y)$ via discrete 2-dimensional convolution to yield a filtered image $C_\nu(x, y)$:

$$C_\nu(x, y) = \sum_i \sum_j M_\nu(i, j) f_g(x - i + 1, y - j + 1) \tag{6.2}$$

Here, the range of i and j in the sum spans the dimension of the image and the kernel. The result of this Gaussian filtering is shown in the right panel of Fig. 6.7.

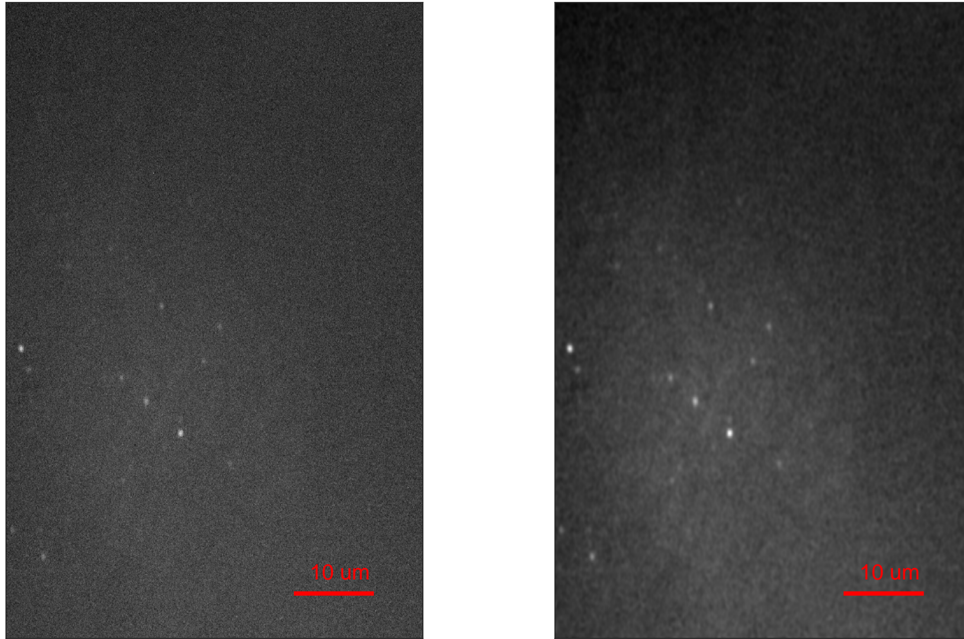

Figure 6.7: Cropped and filtered widefield image under resonant excitation. In the left panel, the raw image has been cropped to remove area outside of the image from the sample. In the right panel, the cropped image has been convolved with a 2D Gaussian kernel with a standard deviation of 2 pixels to match the diffraction limited spot size.

After each image was filtered, the data was sectioned into frequency bands to facilitate image processing. At each frequency band, an aggregate image summarizing the fluorescence over ≈20 GHz of laser tuning was generated by taking the maximum value of each pixel over the images taken at all frequency steps. An example of an aggregate image generated for images taken while scanning the resonant laser from 405.8816-404.9005 THz is shown in the left panel of Fig. 6.8. This aggregate image allowed for identification of candidate emitter sites using a single image.

Sites were identified by first applying a Gaussian bandpass filter to the aggregate image $A(x, y)$, and then fitting 2D Gaussians to the resulting image. The bandpass filter was applied by first convolving the aggregate image with a 2D Gaussian with the lowpass standard deviation σ_{LP}:

$$f_{LP}(x, y) = e^{-\frac{(x^2+y^2)}{2\sigma_{LP}^2}} \tag{6.3}$$

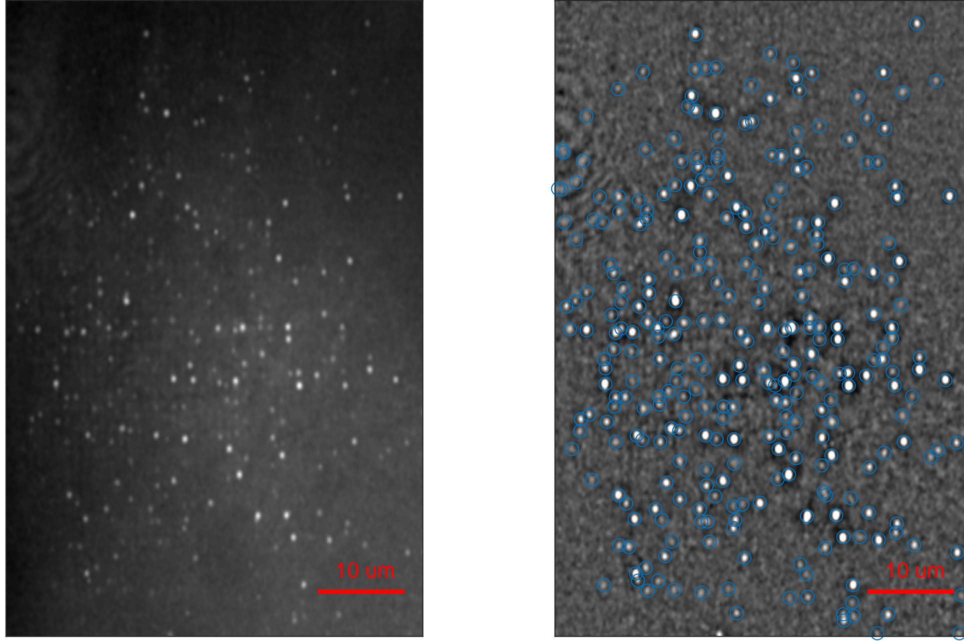

Figure 6.8: Example aggregate widefield image and candidate sites. After raw images are cropped and filtered as shown in Fig. 6.7, an aggregate image is generated to find the locations of candidate emitter sites, as shown in the left panel. A list of candidate sites is generated from the aggregate image by first bandpass filtering the image, and then fitting 2D Gaussian peaks to the resulting filtered image. These candidate sites are shown in blue over the bandpass filtered image in the right panel.

This kernel was discretized and convolved with the aggregate image $I(x, y)$ via discrete 2-dimensional convolution to yield an intermediate filtered image $R(x, y)$:

$$R(x, y) = \sum_i \sum_j I(i, j) f_{LP}(x - i + 1, y - j + 1) \tag{6.4}$$

The resulting image $R(x, y)$ was then high-pass filtered by convolution with a 2D Gaussian with the high pass standard deviation σ_{HP}:

$$f_{HP}(x, y) = e^{-\frac{(x^2+y^2)}{2\sigma_{HP}^2}} \tag{6.5}$$

This kernel was discretized and convolved with the intermediate image $R(x,y)$ via discrete 2-dimensional convolution to yield an bandpass-filtered image $F(x,y)$ (Fig. 6.8):

$$F(x,y) = R(x,y) - \sum_i \sum_j R(i,j) f_{HP}(x-i+1, y-j+1) \tag{6.6}$$

The Gaussian bandpass filtering process highlighted bright spots with radii between the lowpass and highpass filter standard deviations. Candidate emitter sites were generated from the resulting bright spots by fitting 2D Gaussians to the filtered image: these candidate sites are shown as blue circles in the right panel of Fig. 6.8.

At each candidate emitter site, the fluorescence intensity as a function of excitation frequency was constructed. For a given candidate emitter site, pixels were first binned around the spatial center of the 2D Gaussian fit. An example site is highlighted in red in the top left panel of Fig. 6.9, and the group of binned pixels around this site is shown in a red box in the bottom left panel. Then, this group of pixels was summed at each frequency step to find the fluorescence intensity as a function of excitation frequency, $I_{p,q}(\nu)$ for an emitter located at location $x = p$, $y = q$ in the convolved image $C_\nu(x,y)$:

$$I_{p,q}(\nu) = \sum_{i=p-3}^{p+3} \sum_{j=q-3}^{q+3} C_\nu(i,j) \tag{6.7}$$

The number of pixels to include in the binned region was selected to maximize the signal-to-noise ratio. Note that although the bandpass-filtered image $F(x,y)$ was used to generate the candidate sites, the convolved images at each frequency $C_\nu(x,y)$ are used to generate the raw intensity function $I_{p,q}(\nu)$. An example intensity function $I_{p,q}(\nu)$ for one SiV candidate site is shown in the top right panel of Fig. 6.9. In principle, both the emitter fluorescence signal $S_{p,q}$ at a site and background fluorescence from the sample B both depend on the intensity of the excitation laser. A simple model is considered to account for fluctuating

laser intensity $L(\nu)$, where ν is the frequency bin:

$$I_{p,q}(\nu) = S_{p,q}(\nu)L(\nu) + BL(\nu) \tag{6.8}$$

This was modeled as a linear process since the emitters are driven below saturation. The intensity function $L(\nu)$ is calculated by calculating the average value of all pixels in the convolved image $C_\nu(x, y)$ at each frequency:

$$L(\nu) = \frac{1}{xy}\sum_{x}\sum_{y} C_\nu(x, y) \tag{6.9}$$

While $L(\nu)$ accounts for global fluctuations of intensity, it does not account for regional fluctuations, including the point spread function of the widefield microscope. Finally, the frequency-dependent SiV fluorescence signal at a given site $S_{p,q}(\nu)$ is determined by dividing the measured intensity by the noise function:

$$S_{p,q}(\nu) + B = \frac{I_{p,q}(\nu)}{L(\nu)} \tag{6.10}$$

An example of the frequency-dependent intensity function $L(\nu)$ at one site is shown in the center-right panel of Fig. 6.9. This model assumes that there are many color centers such that the emission frequencies of the population of color centers are uncorrelated, and that the dominant intensity fluctuation of the entire image is correlated with the excitation frequency.

The final PLE intensity and constant background signal $S_{p,q}(\nu) + B$ at one site are shown in the bottom right panel of Fig. 6.9, along with the results of fitting a pseudo-Voigt function (Eq. 4.5). The PLE peak occurs at 405.8945 THz, and has a linewidth of 233.7 MHz.

This process was repeated for all candidate sites. A summary of the inhomogeneous distribution over the scan range is provided in Fig. 6.10. A kernel estimate of the empirical probability density function representing the inhomogeneous distribution for 330 peaks detected was calculated using Eqs. 4.3-4.4 is shown in the left panel. A histogram of the

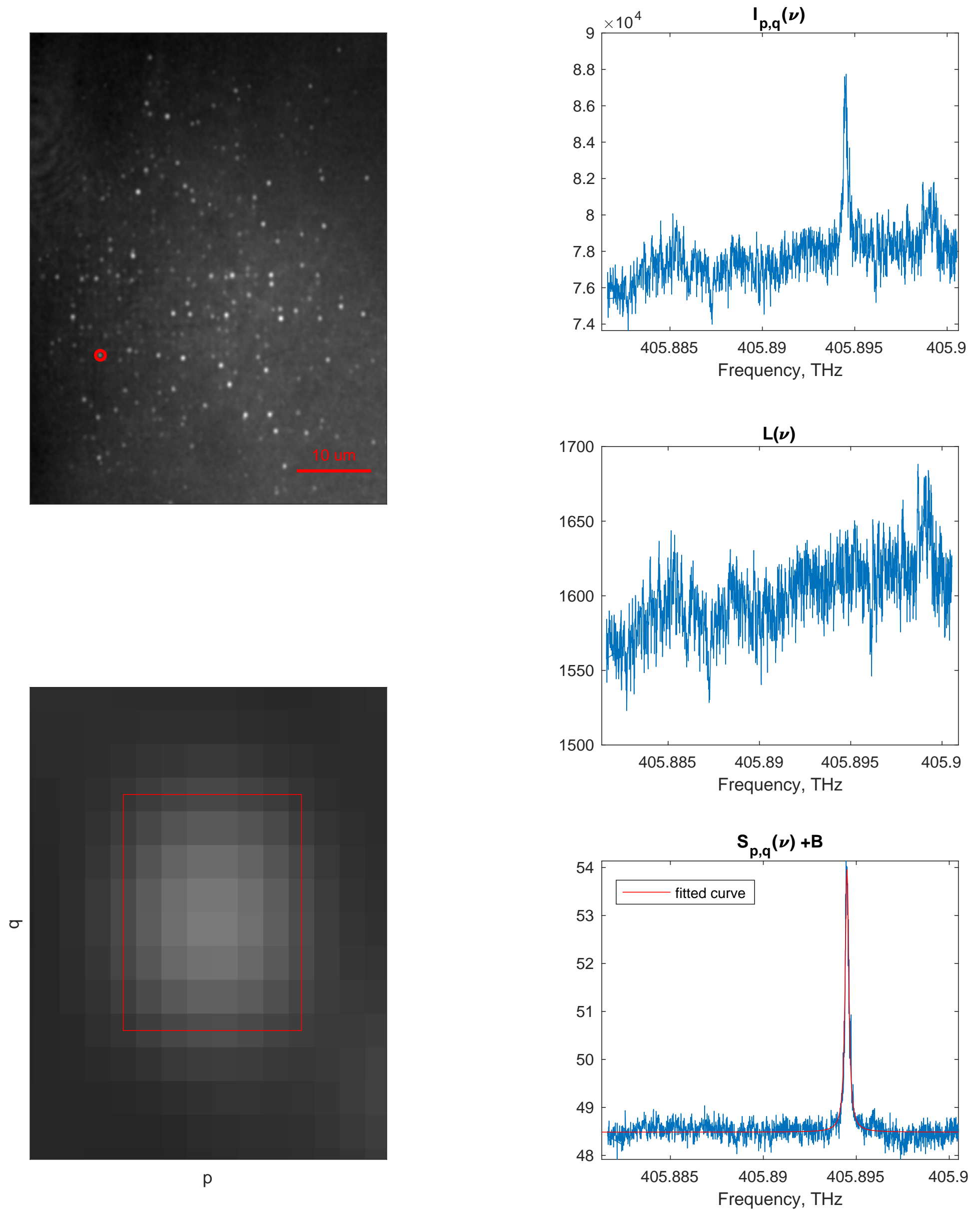

Figure 6.9: Image processing for one widefield photoluminescence excitation site. The top left panel shows the location (p, q) of the candidate site under consideration on the aggregate image. In the bottom left panel, the site is shown in detail: the red rectangle indicates the extent of pixel binning used to generate the intensity function. The extent of the pixel binning was selected to maximize the signal-to-noise ratio. The top right panel shows the raw intensity $I_{p,q}(\nu)$ as a function of frequency (Eq. 6.7). The right center panel shows the laser intensity function $L(\nu)$ constructed with Eq. 6.9. Finally, the bottom panel shows the emitter fluorescence intensity and constant background $S_{p,q}(\nu) + B$ as a function of frequency as calculated using Eq. 6.10.

linewidths of these 178 peaks, as well as a density plot of the linewidth PDF, are shown in the right panel.

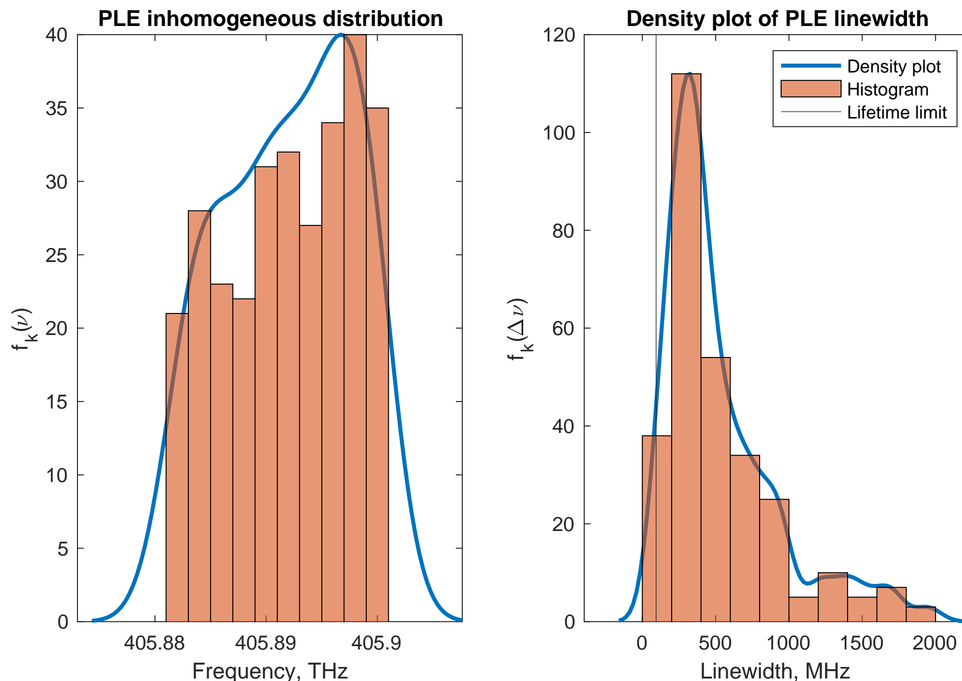

Figure 6.10: Summary of widefield photoluminescence excitation results over one laser scan range. The left panel shows a histogram and a a kernel estimate of the empirical probability density function of locations of 330 widefield PLE peaks. The right panel shows a histogram and a a kernel estimate of the empirical probability density function of the linewidths of the same 178 widefield PLE peaks. The lifetime limit is shown with a thin black line.

This process was repeated over the inhomogeneous distribution shown in the left panel of Fig. 6.4, corresponding to a span of over 1.1 THz from 405.8816 to 407.0007 THz, in 10 MHz steps. A summary of all identified SiV peaks measured with widefield microscopy is provided in Fig. 6.11. The left panel shows the inhomogeneous distribution. A kernel estimate of the empirical probability density function of the locations 47,314 SiV peaks with linewidths less than 2 GHz is provided, along with a histogram of emission frequencies. Two clear peaks in the probability distribution are observed to be centered at 406.6147 THz and 406.8625 THz, as well as the gradual fall-off of probability density at lower frequencies, as observed in the SiV PL spectrum in Fig. 6.4. A Gaussian fit to the distribution, shown in the center panel, reveals that the standard deviation of the peak in probability density at 406.6147 THz is

28.0 GHz (2σ =56.1 GHz) and the standard deviation of the peak in probability density at 406.8625 THz is 20.1 GHz (2σ =40.3 GHz). Finally, the right panel shows a kernel estimate of the empirical probability density function of 47,314 SiV peak linewidths less than 2 GHz.

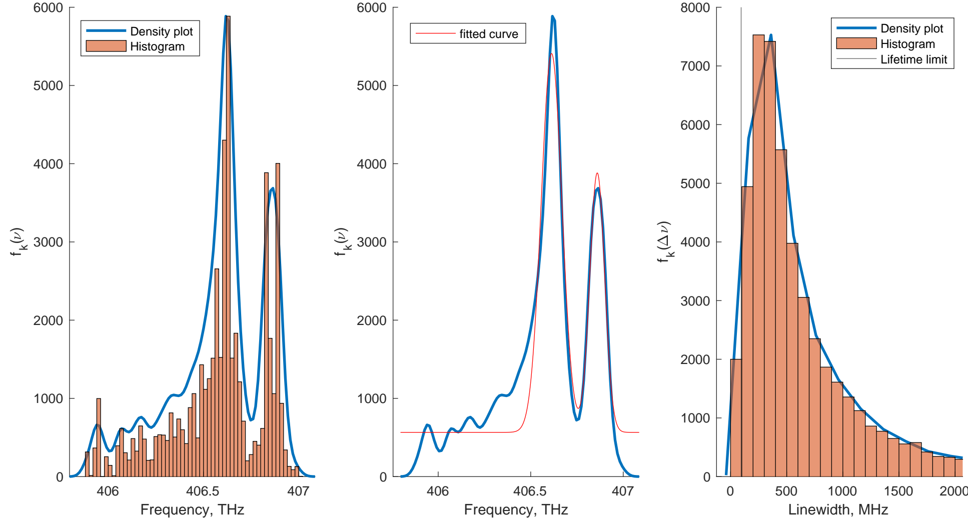

Figure 6.11: Summary of widefield photoluminescence excitation results for 47,314 silicon vacancy peaks. In the left panel, the inhomogeneous distribution of 47,314 SiV peaks with linewidths less than 2 GHz measured using the widefield microscopy technique described in the main text is shown. A kernel estimate of the empirical probability density function of peak locations was calculated using Eqs. 4.3-4.4. In the center panel, a fit to this distribution is shown, revealing two peaks in probability density at 406.6147 THz (σ =28.0 GHz) and 406.8625 THz (σ =20.1 GHz, as well as a fall-off in probability density to find peaks at lower energies. In the right panel, a kernel estimate of the empirical probability distribution of the linewidths of the 47,314 SiV sites with linewidths less than 2 GHz is shown. The linewidth distribution peaks around 300 MHz, approximately three times the SiV lifetime limit.

The SiV peaks are expected to be distributed on a grid spaced by 1 um pitch. The coordinates of the 47,314 SiV sites were clustered to reconstruct the FIB grid. The clustering algorithm iteratively calculated the nearest neighbors from each SiV peak coordinate out to a threshold by computing the distance between all sets of coordinates. For example, for two sites with camera pixel coordinates given as site $l = (x_l, y_l)$ and site $m = (x_m, y_m)$:

$$d_{lm} = \sqrt{(x_l - x_m)^2 + (y_l - y_m)^2} \tag{6.11}$$

The threshold was chosen to be 10 pixels (≈ 800 nm). The centroid of all sites n included in each cluster r was computed using

$$c_r = \frac{1}{n}\Big(\sum_n x_n, \sum_n y_n\Big) \tag{6.12}$$

All clusters are shown in Fig. 6.12, with a heat map indicating the number of peaks included in each cluster. The reconstructed FIB grid is clearly visible, with quality degrading towards the edges as the laser intensity falls off and aberration distorts the image.

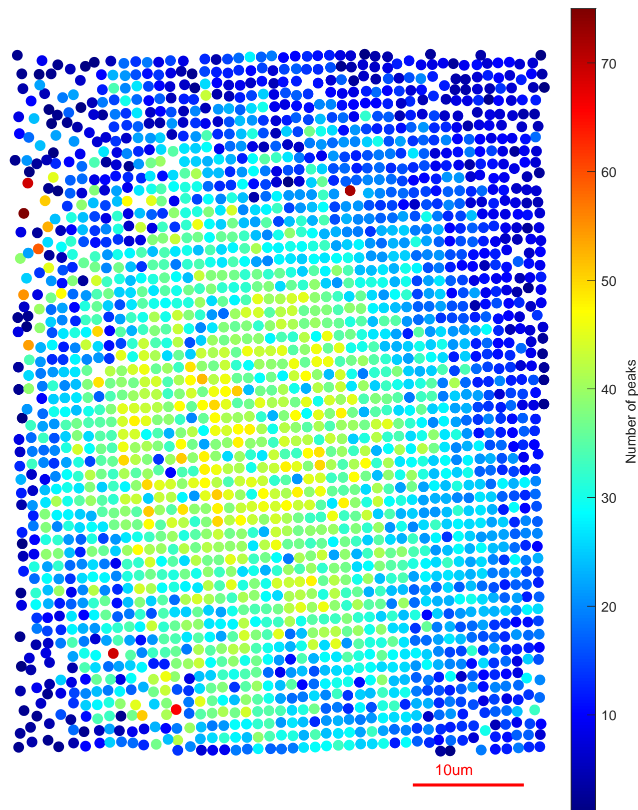

Figure 6.12: Clustered reconstruction of focused ion beam sites measured with widefield microscopy. The 47,314 SiV sites measured and fit were clustered based on their location using the algorithm described in the main text. The centroid of each cluster is plotted here, and the color of the centroid is given by the number of SiV peaks that make up the cluster. The FIB implantation grid is clearly visible.

Chapter 7

Conclusion

In this thesis, we introduced techniques for large scale characterization of quantum emitters using confocal and widefield microscopy. Using these techniques, we investigated silicon vacancy centers incorporated in a diamond overgrowth layer deposited by chemical vapor deposition, and found a narrow inhomogeneous distribution of hundreds of emitters. We investigated two samples implanted with tin, overgrown with chemical vapor deposition diamond, and high pressure high temperature treated, and observed a spectrometer-limited distribution of photoluminescence over thousands of tin vacancy sites. Finally, we demonstrated the ability to spatially multiplex photoluminescence excitation measurements using widefield microscopy, enabling efficient optical characterization of quantum emitters.

7.1 Outlook

The processing techniques presented here, including diamond overgrowth by chemical vapor deposition and high pressure high temperature treatment, yielded samples with high quality quantum emitters and inhomogeneous distributions that are level with the best reports in literature. In this thesis, we reported an inhomogeneous distribution of photoluminescence excitation of the C transition of SiVs in CVD diamond with a standard deviation of 73.5 MHz. Previous reports have found similarly narrow distributions in low-strain CVD diamond [37, 39], though over smaller sample areas and representing fewer color centers. A comparison of the inhomogeneous distribution of SiVs measured via photoluminescence

excitation in the CVD diamond sample (Chapter 4) and those implanted in the FIB sample (Chapter 6) is shown in Fig. 7.1. Not only is the distribution of emitter locations in the FIB sample nearly three orders of magnitude larger, with a standard deviation of 28.0 GHz for the distribution of the lower energy transition, but it also exhibits a broad fall-off of probability to find SiV peaks at lower excitation energies.

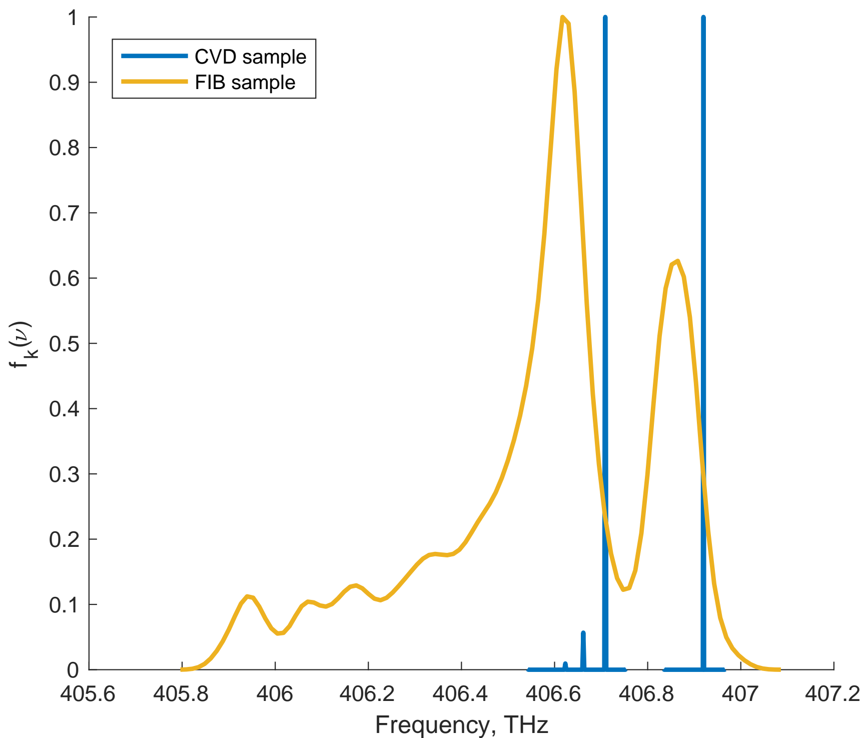

Figure 7.1: Summary: silicon vacancy photoluminescence excitation measurements. Kernel estimates of the empirical probability distribution functions for silicon vacancy photoluminescence excitation measurements in the chemical vapor deposition (CVD) sample and the focused ion beam (FIB) implanted sample. The inhomogeneous distribution of the lower energy transition in the CVD sample had a standard deviation 0f 73.5 MHz, while that of the FIB implanted sample was 28.0 GHz.

Similarly, we reported spectrometer-limited tin vacancy photoluminescence from thousands of sites in two samples treated with high pressure high temperature processes following tin implantation. Photoluminescence excitation measurements confirmed the narrow inhomogeneous distribution: the standard deviation of a kernel estimate of the empirical probability function to find a SnV peak in Sample A was 4.51 GHz, and in Sample B was 2.40 GHz. These results comport with previous work on SnVs in high pressure high temperature treated

diamond, though again far exceed the scale of previous photoluminescence [33] and photoluminescence excitation reports [41]. We also showed that diamond overgrowth prior to HPHT treatment is a viable technique to maintain the implanted Sn atoms throughout HPHT treatment. A comparison of the inhomogeneous distribution of photoluminescence for SnVs measured in the two HPHT-treated samples (Chapter 5) and for SnVs measured in the FIB implanted sample (Chapter 6) are shown in Fig. 7.2.

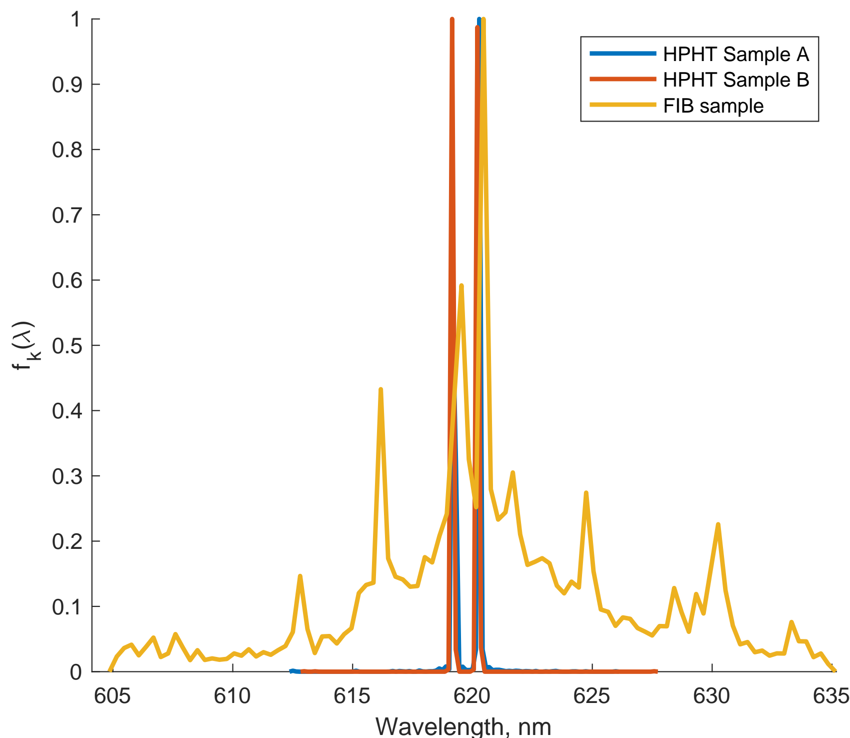

Figure 7.2: Summary: tin vacancy photoluminescence measurements. Normalized kernel estimates of the empirical probability density functions for tin vacancy photoluminescence in three samples are shown. The inhomogeneous distributions of tin vacancies in the two HPHT-treated samples, Sample A and Sample B, are spectrometer-limited, while the inhomogeneous distribution of tin vacancies in the focus ion beam implanted sample is much broader.

7.2 Future directions

Now that the ability to develop samples with large numbers of high quality, low inhomogeneous distribution SiVs and SnVs has been demonstrated, the obvious next step would be

to demonstrate Hong-Ou-Mandel (HOM) interference with distinct emitters in the samples. Following the demonstration of HOM interference, detailed characterization of the spin properties would be necessary prior to demonstrating spin-photon entanglement, but spin-spin entanglement between distinct, separated pairs of SiVs or SnVs would follow naturally.

The homogeneity of the samples presented lends them well to use in the development of large-scale quantum device applications such as quantum repeater nodes. To achieve this goal, devices must be patterned into the diamond using nanofabrication techniques. If the optical properties are maintained throughout fabrication, these quantum emitters would be ideal for heterogeneously integrated diamonds with photonic integrated circuits [15], and may even mitigate the need for voltage-driven strain tuning, saving cooling power at dilution-refrigerator temperatures.

Bibliography

[1] M. K. Bhaskar, R. Riedinger, B. Machielse, D. S. Levonian, C. T. Nguyen, E. N. Knall, H. Park, D. Englund, M. Lončar, D. D. Sukachev, and M. D. Lukin, "Experimental demonstration of memory-enhanced quantum communication," *Nature*, vol. 480, pp. 60–64, 2020.

[2] C. H. Bennett and G. Brassard, "Quantum cryptography: Public key distribution and coin tossing," in *Proceedings of IEEE International Conference on Computers, Systems, and Signal Processing*, (Bangalore, India), pp. 175–189, 1984.

[3] E. T. Khabiboulline, J. Borregaard, K. De Greve, and M. D. Lukin, "Optical Interferometry with Quantum Networks," *Physical Review Letters*, vol. 123, no. 7, 2019.

[4] M. Pompili, S. L. Hermans, S. Baier, H. K. Beukers, P. C. Humphreys, R. N. Schouten, R. F. Vermeulen, M. J. Tiggelman, L. dos Santos Martins, B. Dirkse, S. Wehner, and R. Hanson, "Realization of a multinode quantum network of remote solid-state qubits," *Science*, vol. 372, no. 6539, 2021.

[5] H. J. Kimble, "The quantum internet," *Nature*, vol. 453, 6 2008.

[6] S. Pirandola, R. Laurenza, C. Ottaviani, and L. Banchi, "Fundamental limits of repeaterless quantum communications," *Nature Communications*, vol. 8, 2017.

[7] W. K. Wootters and W. H. Zurek, "A single quantum cannot be cloned," *Nature*, vol. 299, no. 5886, 1982.

[8] S. D. Barrett and P. Kok, "Efficient high-fidelity quantum computation using matter qubits and linear optics," *Physical Review A - Atomic, Molecular, and Optical Physics*, vol. 71, no. 6, 2005.

[9] G. Wolfowicz, F. J. Heremans, C. P. Anderson, S. Kanai, H. Seo, A. Gali, G. Galli, and D. D. Awschalom, "Quantum guidelines for solid-state spin defects," *Nature Reviews Materials*, vol. 6, no. 10, 2021.

[10] H. Choi, M. Pant, S. Guha, and D. Englund, "Percolation-based architecture for cluster state creation using photon-mediated entanglement between atomic memories," *npj Quantum Information*, vol. 5, no. 1, pp. 1–8, 2019.

[11] L. M. Duan, M. D. Lukin, J. I. Cirac, and P. Zoller, "Long-distance quantum communication with atomic ensembles and linear optics," *Nature*, vol. 414, no. 6862, 2001.

[12] L. M. Duan, A. Kuzmich, and H. J. Kimble, "Cavity QED and quantum-information processing with "hot" trapped atoms," *Physical Review A - Atomic, Molecular, and Optical Physics*, vol. 67, no. 3, 2003.

[13] K. Huang and A. Rhys, "Theory of light absorption and non-radiative transitions in F -centres," *Proceedings of the Royal Society of London. Series A. Mathematical and Physical SciencesR*, vol. 204, no. 1078, 1950.

[14] B. Machielse, S. Bogdanovic, S. Meesala, S. Gauthier, M. J. Burek, G. Joe, M. Chalupnik, Y. I. Sohn, J. Holzgrafe, R. E. Evans, C. Chia, H. Atikian, M. K. Bhaskar, D. D. Sukachev, L. Shao, S. Maity, M. D. Lukin, and M. Lončar, "Quantum Interference of Electromechanically Stabilized Emitters in Nanophotonic Devices," *Physical Review X*, vol. 9, no. 3, 2019.

[15] N. H. Wan, T. J. Lu, K. C. Chen, M. P. Walsh, M. E. Trusheim, L. De Santis, E. A. Bersin, I. B. Harris, S. L. Mouradian, I. R. Christen, E. S. Bielejec, and D. Englund, "Large-scale integration of artificial atoms in hybrid photonic circuits," *Nature*, vol. 583, no. 7815, 2020.

[16] C. T. Nguyen, D. D. Sukachev, M. K. Bhaskar, B. MacHielse, D. S. Levonian, E. N. Knall, P. Stroganov, C. Chia, M. J. Burek, R. Riedinger, H. Park, M. Lončar, and M. D. Lukin, "An integrated nanophotonic quantum register based on silicon-vacancy spins in diamond," *Physical Review B*, vol. 100, no. 16, 2019.

[17] H. Bernien, L. Childress, L. Robledo, M. Markham, D. Twitchen, and R. Hanson, "Two-photon quantum interference from separate nitrogen vacancy centers in diamond," *Physical Review Letters*, vol. 108, no. 4, pp. 1–5, 2012.

[18] E. Neu, C. Hepp, M. Hauschild, S. Gsell, M. Fischer, H. Sternschulte, D. Steinmüller-Nethl, M. Schreck, and C. Becher, "Low-temperature investigations of single silicon vacancy colour centres in diamond," *New Journal of Physics*, vol. 15, 2013.

[19] W. Saslow, T. K. Bergstresser, and M. L. Cohen, "Band structure and optical properties of diamond," *Physical Review Letters*, vol. 16, no. 9, 1966.

[20] R. S. Balmer, J. R. Brandon, S. L. Clewes, H. K. Dhillon, J. M. Dodson, I. Friel, P. N. Inglis, T. D. Madgwick, M. L. Markham, T. P. Mollart, N. Perkins, G. A. Scarsbrook, D. J. Twitchen, A. J. Whitehead, J. J. Wilman, and S. M. Woollard, "Chemical vapour deposition synthetic diamond: Materials, technology and applications," *Journal of Physics Condensed Matter*, vol. 21, no. 36, 2009.

[21] M. W. Doherty, N. B. Manson, P. Delaney, F. Jelezko, J. Wrachtrup, and L. C. Hollenberg, "The nitrogen-vacancy colour centre in diamond," *Physics Reports*, vol. 528, no. 1, 2013.

[22] A. Faraon, C. Santori, Z. Huang, V. M. Acosta, and R. G. Beausoleil, "Coupling of nitrogen-vacancy centers to photonic crystal cavities in monocrystalline diamond," *Physical Review Letters*, vol. 109, no. 3, 2012.

[23] M. Ruf, M. Ijspeert, S. Van Dam, N. De Jong, H. Van Den Berg, G. Evers, and R. Hanson, "Optically Coherent Nitrogen-Vacancy Centers in Micrometer-Thin Etched Diamond Membranes," *Nano Letters*, vol. 19, no. 6, 2019.

[24] A. Gali, "Ab initio theory of the nitrogen-vacancy center in diamond," *Nanophotonics*, 2019.

[25] L. Robledo, L. Childress, H. Bernien, B. Hensen, P. F. Alkemade, and R. Hanson, "High-fidelity projective read-out of a solid-state spin quantum register," *Nature*, vol. 477, no. 7366, 2011.

[26] J. P. Goss, R. Jones, S. J. Breuer, P. R. Briddon, and S. Öberg, "The twelve-line 1.682 eV luminescence center in diamond and the vacancy-silicon complex," *Physical Review Letters*, vol. 77, no. 14, 1996.

[27] U. F. D'Haenens-Johansson, A. M. Edmonds, B. L. Green, M. E. Newton, G. Davies, P. M. Martineau, R. U. Khan, and D. J. Twitchen, "Optical properties of the neutral silicon split-vacancy center in diamond," *Physical Review B - Condensed Matter and Materials Physics*, vol. 84, no. 24, 2011.

[28] A. Gali and J. R. Maze, "Ab initio study of the split silicon-vacancy defect in diamond: Electronic structure and related properties," *Physical Review B - Condensed Matter and Materials Physics*, vol. 88, no. 23, 2013.

[29] C. Hepp, T. Müller, V. Waselowski, J. N. Becker, B. Pingault, H. Sternschulte, D. Steinmüller-Nethl, A. Gali, J. R. Maze, M. Atatüre, and C. Becher, "Electronic structure of the silicon vacancy color center in diamond," *Physical Review Letters*, vol. 112, no. 3, 2014.

[30] T. Müller, C. Hepp, B. Pingault, E. Neu, S. Gsell, M. Schreck, H. Sternschulte, D. Steinmüller-Nethl, C. Becher, and M. Atatüre, "Optical signatures of silicon-vacancy spins in diamond," *Nature Communications*, vol. 5, 2014.

[31] S. Meesala, Y. I. Sohn, B. Pingault, L. Shao, H. A. Atikian, J. Holzgrafe, M. Gündoğan, C. Stavrakas, A. Sipahigil, C. Chia, R. Evans, M. J. Burek, M. Zhang, L. Wu, J. L. Pacheco, J. Abraham, E. Bielejec, M. D. Lukin, M. Atatüre, and M. Lončar, "Strain engineering of the silicon-vacancy center in diamond," *Physical Review B*, vol. 97, no. 20, 2018.

[32] M. K. Bhaskar, D. D. Sukachev, A. Sipahigil, R. E. Evans, M. J. Burek, C. T. Nguyen, L. J. Rogers, P. Siyushev, M. H. Metsch, H. Park, F. Jelezko, M. Lončar, and M. D. Lukin, "Quantum Nonlinear Optics with a Germanium-Vacancy Color Center in a Nanoscale Diamond Waveguide," *Physical Review Letters*, vol. 118, no. 22, 2017.

[33] T. Iwasaki, Y. Miyamoto, T. Taniguchi, P. Siyushev, M. H. Metsch, F. Jelezko, and M. Hatano, "Tin-Vacancy Quantum Emitters in Diamond," *Physical Review Letters*, vol. 119, no. 25, 2017.

[34] M. E. Trusheim, N. H. Wan, K. C. Chen, C. J. Ciccarino, J. Flick, R. Sundararaman, G. Malladi, E. Bersin, M. Walsh, B. Lienhard, H. Bakhru, P. Narang, and D. Englund, "Lead-related quantum emitters in diamond," *Physical Review B*, vol. 99, no. 7, 2019.

[35] C. Hepp, *Electronic Structure of the Silicon Vacancy Color Center in Diamond*. PhD thesis, Saarbrücken, 2014.

[36] M. E. Trusheim, B. Pingault, N. H. Wan, M. Gündoğan, L. De Santis, R. Debroux, D. Gangloff, C. Purser, K. C. Chen, M. Walsh, J. J. Rose, J. N. Becker, B. Lienhard, E. Bersin, I. Paradeisanos, G. Wang, D. Lyzwa, A. R. Montblanch, G. Malladi, H. Bakhru, A. C. Ferrari, I. A. Walmsley, M. Atatüre, and D. Englund, "Transform-Limited Photons from a Coherent Tin-Vacancy Spin in Diamond," *Physical Review Letters*, vol. 124, no. 2, 2020.

[37] L. J. Rogers, K. D. Jahnke, T. Teraji, L. Marseglia, C. Müller, B. Naydenov, H. Schauffert, C. Kranz, J. Isoya, L. P. McGuinness, and F. Jelezko, "Multiple intrinsically identical single-photon emitters in the solid state," *Nature Communications*, vol. 5, 2014.

[38] Y. Chu, N. P. De Leon, B. J. Shields, B. Hausmann, R. Evans, E. Togan, M. J. Burek, M. Markham, A. Stacey, A. S. Zibrov, A. Yacoby, D. J. Twitchen, M. Loncar, H. Park, P. Maletinsky, and M. D. Lukin, "Coherent optical transitions in implanted nitrogen vacancy centers," *Nano Letters*, vol. 14, no. 4, 2014.

[39] A. Sipahigil, K. D. Jahnke, L. J. Rogers, T. Teraji, J. Isoya, A. S. Zibrov, F. Jelezko, and M. D. Lukin, "Indistinguishable photons from separated silicon-vacancy centers in diamond," *Physical Review Letters*, vol. 113, no. 11, pp. 1–5, 2014.

[40] A. E. Rugar, C. Dory, S. Aghaeimeibodi, H. Lu, S. Sun, S. D. Mishra, Z. X. Shen, N. A. Melosh, and J. Vučković, "Narrow-Linewidth Tin-Vacancy Centers in a Diamond Waveguide," *ACS Photonics*, vol. 7, no. 9, 2020.

[41] J. Görlitz, D. Herrmann, G. Thiering, P. Fuchs, M. Gandil, T. Iwasaki, T. Taniguchi, M. Kieschnick, J. Meijer, M. Hatano, A. Gali, and C. Becher, "Spectroscopic investigations of negatively charged tin-vacancy centres in diamond," *New Journal of Physics*, vol. 22, no. 1, 2020.

[42] S. Wilhelm, G. B., M. Gulch, and Heinz. H., "The Confocal Laser Scanning Microscope," tech. rep., Zeiss Jena, 2003.

[43] M. P. Walsh, *Statistical metrology and process control of quantum devices.* PhD thesis, Massachusetts Institute of Technology, Cambridge, 6 2020.

[44] C. Bradac, W. Gao, J. Forneris, M. E. Trusheim, and I. Aharonovich, "Quantum nanophotonics with group IV defects in diamond," *Nature Communications*, vol. 10, no. 1, 2019.

[45] K. Ohno, F. Joseph Heremans, L. C. Bassett, B. A. Myers, D. M. Toyli, A. C. Bleszynski Jayich, C. J. Palmstrøm, and D. D. Awschalom, "Engineering shallow spins in diamond with nitrogen delta-doping," *Applied Physics Letters*, vol. 101, no. 8, 2012.

[46] H. Sternschulte, K. Thonke, R. Sauer, P. C. Münzinger, and P. Michler, "1.681-eV luminescence center in chemical-vapor-deposited homoepitaxial diamond films," *Physical Review B*, vol. 50, no. 19, 1994.

[47] M. P. Walsh, "Microwave and Optical Control of Sub-Diffraction Spin Qubits in Diamond at Cryogenic Temperatures," 9 2015.

[48] M. E. Trusheim, B. Pingault, N. H. Wan, M. Gundogan, L. De Santis, K. Chen, M. Atature, and D. Englund, "Quantum Optics with Tin-Vacancy Emitters in Diamond," in *2019 Conference on Lasers and Electro-Optics, CLEO 2019 - Proceedings*, 2019.

[49] A. E. Rugar, H. Lu, C. Dory, S. Sun, P. J. McQuade, Z. X. Shen, N. A. Melosh, and J. Vučković, "Generation of Tin-Vacancy Centers in Diamond via Shallow Ion Implantation and Subsequent Diamond Overgrowth," *Nano Letters*, vol. 20, no. 3, 2020.

[50] A. Yelisseyev and H. Kanda, "Optical centers related to 3d transition metals in diamond," *New Diamond and Frontier Carbon Technology*, vol. 17, no. 3, 2007.

[51] T. Schröder, M. E. Trusheim, M. Walsh, L. Li, J. Zheng, M. Schukraft, A. Sipahigil, R. E. Evans, D. D. Sukachev, C. T. Nguyen, J. L. Pacheco, R. M. Camacho, E. S. Bielejec, M. D. Lukin, and D. Englund, "Scalable focused ion beam creation of nearly lifetime-limited single quantum emitters in diamond nanostructures," *Nature Communications*, vol. 8, 2017.